Carbon nanotubes:

in situ studies of growth and electromechanical properties

Johan Ek Weis

Degree of Doctor of Philosophy
University of Edinburgh
2011

Abstract

Carbon nanotubes have been found to have extraordinary properties, such as ballistic electrical conductivity, extremely high thermal conductivity and they can be metallic or semiconducting with a wide range of band gaps.

There are however several issues that have to be solved before these properties can be fully utilised. One of these issues is that the nanotube growth temperature must be lowered in order to make the synthesis compatible with the fabrication processes used in electronics. The whole environment is heated to temperatures typically higher than 500 °C in the standard growth techniques whereas only a very localised area is heated in the technique developed here. This technique thus provides a way around the temperature issue.

In the method developed here, the catalyst is deposited on top of a small metal (molybdenum) wire on the substrate. The high temperature required for nanotube growth is then reached by Joule heating by sending a current through the metal wire. This process eliminates the furnace which is used in conventional chemical vapour deposition and localises the high temperature to a very small and controlled area of the sample. Consequently, this technique is compatible with the semiconductor technology used today.

Another advantage of this technique is that, since no furnace is required, a small growth chamber, which fits under a microscope, can be used. This allows *in situ* studies of the growth by optical microscopy and by Raman spectroscopy.

By changing the carbon precursor, single- or multiwalled nanotubes can be grown. This can be important when producing devices since single-walled nanotubes predominantly are semiconducting whereas multi-walled mainly are metallic.

The multi-walled nanotubes grow in a rapid and concerted process. This growth was monitored through an optical microscope. It was found that the thickness of the support layer and especially the catalyst are even more crucial parameters for nanotube growth using this local heating technique than in conventional processes. The activation energy could be extracted and was found to be 1.1-1.3 eV.

The carbon nanotube growth was investigated by *in situ* Raman spectroscopy. The growth evolution could be well described by a model using the initial growth rate and the catalyst lifetime as parameters. The process was found to be limited by the mass transport of the carbon precursor. It was found that the molybdenum wire creates an additional pathway for the carbon cycle from gas to nanotube formation.

The Raman spectra were studied at elevated temperatures. A decrease in intensity and a shift towards lower wavenumbers with increasing temperature was observed for the Stokes signal. It was found that the laser used for the Raman measurements could heat the nanotubes to high temperatures without any other heat source.

Vertically aligned arrays of nanotubes were grown by conventional CVD. These arrays were actuated by applying a DC voltage between them. An effective Young's modulus of the arrays was found to be similar to that of rubber, which is orders of magnitude lower than for individual nanotubes. The capacitance between the arrays was measured to be tens of fF with a tunability of over 20%.

“You can do anything you want to do, if you put your mind to it.“

MacGyver, from the TV series MacGyver

Declaration

I declare that the work presented in this thesis is my own unless otherwise stated by reference.

Johan Ek Weis

Publications

J. Ek-Weis, O. A. Nerushev, E. E. B. Campbell, *Optical in-situ characterisation of carbon nanotube growth*, accepted for publication in the International Journal of Nanotechnology

S. Dittmer, J. Ek-Weis, O. A. Nerushev, E. E. B. Campbell, *Growth of Aligned MWNT Arrays Using a Micrometer Scale Local-Heater at Low Ambient Temperature*, J. Nanosci. Nanotechnol. **10**, 6, 4015-4022 (2010)

N. Olofsson, J. Ek-Weis, A. Eriksson, T. Idda, E.E.B Campbell, *Determination of the effective Young's modulus of vertically aligned carbon nanotube arrays: a simple nanotube-based varactor*, Nanotechnology **20** (2009) 385710

J. Ek-Weis, A. Eriksson, T. Idda, N. Olofsson, E.E.B. Campbell, *Radio-frequency characterization of varactors based on carbon nanotube arrays,* Proc. IMechE, Part N: J. Nanoengineering and Nanosystems **222** 34 (2009) 111-115

S. Bengtsson, P. Enoksson, F. Alavian Ghavanini, K. Engström, P. Lundgren, E. E. B. Campbell, J. Ek-Weis, N. Olofsson, A. Eriksson, *Carbon-based nanoelectromechanical devices*, International Journal of High Speed Electronics & Systems, **20** 1 (2011) 195-204.

T. Idda, N. Olofsson, J. Ek-Weis, J. Ruan, S. Pacchini, E. Campbell, R. Plana., *Modélisation d'une capacité variable à base de nanotubes de carbone verticaux,* 16èmes Journées Nationales Microondes (JNM 2009), 27-29 Mai 2009, 5p, Grenoble

S. Dittmer, N. Olofsson, J. Ek-Weis, O.A. Nerushev, A.V. Gromov, E.E.B. Campbell, *In situ Raman studies of single-walled carbon nanotubes grown by local catalyst heating*, Chem. Phys. Lett. **457** (2008) 206-210

Acknowledgements

There are many people that I'm grateful that I have met and gotten to know. I would especially like to thank:

Eleanor for taking me along on this adventure and for giving me a lot of freedom to follow my own ideas but also keeping me focused. Thank you for everything!

Oleg for sharing some of your vast physics knowledge and for all interesting discussions (about science and everything else) both in the lab and in kb.

Andrei for your chemistry (and history) passion and knowledge.

Olof for keeping two of my languages alive.

Gordon for countless hours talking about football and life in general.

Chaweewan for always being positive.

Kirsten for being like a younger sister.

Andrew for always being happy to help and to answer questions about Scotland.

Ada for your unspoiled optimism that everything will work immediately.

Our undergraduate James, and high school students John, Andrew and Duncan for seeing everything with fresh eyes.

Jonathan and Craig (and all above!) for the great atmosphere in our office.

Elizabeth for promoting my rollercoaster image.

Niklas for all your help in the cleanroom.

Staffan for teaching me everything in the beginning of my project.

My office mates in Sweden; SangWook and Johannes, the whole former atomic and molecular physics group and the MC2 nanofabrication laboratory in Gothenburg for everything during my time in Gothenburg when the labs in Edinburgh were being refurbished.

Santiago for showing me life as a PhD student before I started it myself.

Per for telling me about the PhD position that eventually brought me to Edinburgh.

The Portobello Mushrooms (and our previous teams) for making the ChemSoc league an amazing time.

Ben and all his merry fatneckers and all other footballers for the great times we've had both on and off the pitch.

I would also like to thank all other friendly people in Edinburgh for making my time here a wonderful experience.

Mum and dad for your support on my adventures, även om jag vet att ni tycker om Lindome…

Danne for being a great brother, och för att du håller med om att det finns mer att se än Mölndal...

Minha querida Sara for always being so happy and gorgeous.

Abbreviations

CNT	Carbon nanotube
CVD	Chemical vapour deposition
DWCNT	double-walled carbon nanotube
eV	Electron volt
MWCNT	Multi-walled carbon nanotube
RBM	Radial breathing mode
rf	Radio frequency
sccm	Standard cubic centimetres per minute
SEM	Scanning electron microscopy
SWCNT	Single-walled carbon nanotube
TEM	Transmission electron microscopy

Table of contents

Chapter 1 Introduction

There has been a lot of research about carbon nanotubes since the boost in 1991 after the work by Ijima [1]. It has been found that carbon nanotubes have a lot of fascinating properties, such as ballistic electrical conductivity [2], they are extremely mechanically strong and resilient [3] and they can be semiconducting with a wide range of band gaps. They can also withstand very high current densities and are very good thermal conductors [4]. Several thousand papers about carbon nanotubes are published every year, but there is still a lot that is unknown, in particular the exact growth mechanism. Different models have been suggested but there is still no complete understanding of the process. The properties of the nanotubes depend, for example, on whether they are single-walled or multi-walled, their chirality and the amount of defects. To be able to take full advantage of these different properties it is therefore essential to understand the growth mechanism in order to tailor the growth to yield only nanotubes of the desired kind.

The growth temperature needs to be kept below about 450 °C for integration of nanotubes into electronics. For example, dielectrics with a low dielectric constant can otherwise be damaged and doping atoms can migrate. There have been a few studies where the growth temperature has been kept below this value but the nanotube quality is then generally low [5, 6].

Here, a growth technique that is both compatible with current microelectronics processing and that allows *in situ* studies of the growth is investigated. In this local heating technique, a small metal wire coated with nanotube catalyst material is fabricated on a substrate. This small metal wire or heater is heated to nanotube growth temperatures by resistive or Joule heating. Since this heater is small it only heats the substrate in the immediate vicinity, which makes the technique compatible with microelectronic fabrication. Since no furnace is required, in contrast to standard nanotube synthesis, a small growth chamber that fits under an optical microscope and inside a Raman spectrometer can be used. This allows *in situ* studies of the nanotube growth evolution.

In this thesis we start by looking at the structure and some properties of carbon nanotubes, followed by how they are synthesised in Chapter 2. The sample fabrication using different cleanroom processes is discussed in Chapter 3. The local heating technique to grow carbon nanotubes that was developed and used in this thesis is thereafter explained. Two of the main characterisation techniques, scanning electron microscopy (SEM) and Raman spectroscopy, are discussed with emphasis on their application for the study of carbon nanotubes in Chapter 4.

Chapter 5 is devoted to growth of carbon nanotubes using acetylene as carbon feedstock. The growth is studied *in situ* using optical microscopy and *ex situ* by SEM and Raman spectroscopy. Local heaters with a temperature gradient along the heater are used to study the influence of different temperatures. It is also shown that the lasers used for Raman spectroscopy can be used to heat parts of the heater to selectively grow nanotubes at these locations.

Chapter 6 is focused on studies of growth of single-walled nanotubes, with ethylene as carbon feedstock, using *in situ* Raman spectroscopy. Two different modes are investigated; "intermittent" and real time. In the intermittent technique the nanotube growth is stopped after selected growth times such that Raman spectra with a high signal-to-noise ratio can be obtained. Several different laser excitation wavelengths can thus be used to study the growth after the same growth time. Real time refers to continuous acquisition of Raman spectra as the nanotubes are growing.

In Chapter 7 the temperature influence on the Raman spectra is investigated. The temperature of the nanotubes is increased by varying the power of the laser used for the Raman measurements. A strong blackbody background is found in the Raman spectra which is used to determine the temperature of the nanotubes.

The electromechanical properties of vertically aligned carbon nanotubes are investigated in Chapter 8. This is the only chapter in this thesis where the nanotubes have not been grown by the local heating technique but by standard chemical vapour deposition. The vertically aligned nanotubes are used to create an electronic device, a varactor, which is characterised.

Chapter 2 Carbon nanotubes

It is often said that carbon nanotube research started with Ijima's paper in 1991 [1], where multi-walled carbon nanotubes were presented. Radushkevich and Lukyanovich had already reported tubular carbon filaments as early as 1952 [7], but these were not recognised as carbon nanotubes. Other reports about similar structures exist in the literature before Ijima's paper and it is not obvious who should be credited for the discovery of carbon nanotubes [8]. Some earlier papers had been published in Russian journals which had less impact in the West. After the development of high resolution transmission electron microscopes and due to the interest in fullerenes, the research community was more ready for nanotubes in the beginning of the 1990s. Carbon nanotube research was tremendously increased after Ijima's report, and in most papers, this is referred to as the discovery of nanotubes. Ijima's paper from 1993 is arguably the first unambiguous experimental report on single-walled carbon nanotubes [9].

2.1 Carbon nanotube structure

The most common analogy used when introducing carbon nanotubes is to think of them as a single two-dimensional layer of graphite, a graphene sheet, which is rolled to form a cylinder. Even though this has nothing to do with how they actually are produced, as is described in chapter 2.3, it gives a good explanation of the structure of nanotubes. It can also explain some of the properties of the nanotubes, which are discussed below.

Carbon nanotubes can either consist of one shell, single-walled carbon nanotubes (SWCNTs), or consist of several concentric shells, multi-walled carbon nanotubes (MWCNTs). These are then structured similar to a Russian doll or an onion. The different shells in a MWCNT are separated by the interlayer distance in graphite, which is 3.41 Å. Other similar structures also exist, for example carbon nanofibres where the angle between the graphene sheets and the tube axis is nonzero, see Figure 2.1.

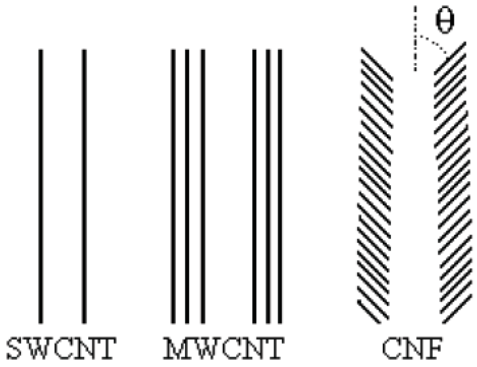

Figure 2.1. Schematic of a single-walled carbon nanotube, SWCNT, a multi-walled carbon nanotube, MWCNT, and carbon nanofibre, CNF.

Carbon nanotubes can have an extremely high aspect ratio, with lengths up to centimetres and diameters of less than one nanometre [10].

A graphene sheet is constructed of carbon atoms positioned at the vertices of hexagons. The symmetry can be described by the unit vectors $\mathbf{a_1} = a_0(\sqrt{3}, 0)$ and $\mathbf{a_2} = a_0(\sqrt{3}/2, 3/2)$, where $a_0 = 0.142$ nm is the carbon-carbon bond length, see Figure 2.2. Each unit cell contains two carbon atoms located at $1/3(\mathbf{a_1} + \mathbf{a_2})$ and $2/3(\mathbf{a_1} + \mathbf{a_2})$. The length of the lattice vectors are $|\mathbf{a_1}| = |\mathbf{a_2}| = 2.461$ Å with an angle of 60° between them. Using these vectors, each nanotube can be characterised by its chiral vector, which is defined as:

$$\mathbf{c} = (n_1, n_2) = n_1\mathbf{a_1} + n_2\mathbf{a_2}, \qquad 2.1$$

where n_1 and n_2 are positive integers. This is the vector between two points in the graphene sheet which are rolled to coincide, see Figure 2.2. It therefore describes the helicity of the nanotube. It also becomes the circumference of the nanotube and is thus perpendicular to the tube axis. The diameter of a nanotube can thus be calculated from its chiral vector:

$$d = \frac{|\mathbf{c}|}{\pi} = \frac{a_0}{\pi}\sqrt{n_1^2 + n_1 n_2 + n_2^2} \qquad 2.2$$

The chiral angle, θ, is the direction of the chiral vector. It is defined as the angle between $\mathbf{a_1}$ and $\mathbf{c}$, and can be calculated from:

$$\cos\theta = \frac{\mathbf{a_1} \cdot \mathbf{c}}{|\mathbf{a_1}| \cdot |\mathbf{c}|} = \frac{n_1 + n_2/2}{\sqrt{n_1^2 + n_1 n_2 + n_2^2}} \qquad 2.3$$

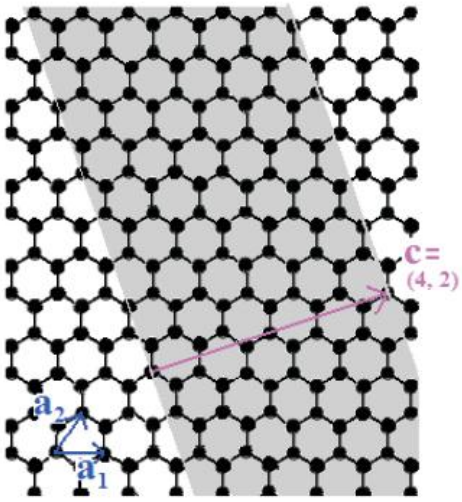

Figure 2.2. Graphene sheet with the unit vectors a_1 and a_2. When rolled to a cylinder, the grey area will be the surface of a nanotube with chiral vector **c** = (4, 2).

Since the hexagons in the graphene sheet have six-fold symmetry, there exists an equivalent nanotube in the interval 0°-60° for all nanotubes. For each nanotube with a chiral angle between 30° and 60°, there also exists one mirrored nanotube with a chiral angle between 0° and 30°. It is therefore sufficient to consider nanotubes in this interval. Nanotubes with a chiral vector (n,0), that is where $\theta = 0°$, are termed zig-zag nanotubes since the circumference forms a zig-zag pattern, see Figure 2.3. Nanotubes of the form (n,n), $\theta = 30°$, are called armchair nanotubes since the circumference resembles an armchair. The remaining nanotubes are labelled chiral nanotubes.

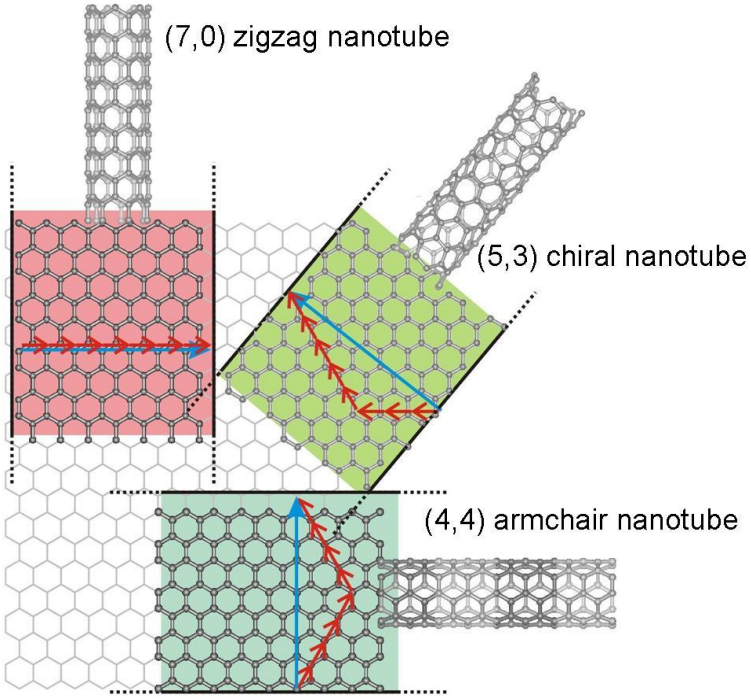

Figure 2.3. Sketch of how a graphene sheet can be thought to be rolled up to form an armchair, zig-zag and a chiral nanotube. The red arrows show how the unit vectors are added together to form the chiral vector, shown by a blue arrow. The chiral vector becomes the circumference of the nanotube. Adapted from [11]

2.2 Band structure of carbon nanotubes

As already mentioned, carbon nanotubes are very similar to graphene. As a first approximation, it is also possible to calculate the electronic properties of nanotubes from graphene [12]. The electronic properties of graphene can be calculated in reciprocal space. The reciprocal lattice vectors perpendicular, $\mathbf{k}_\perp$, and parallel, $\mathbf{k}_z$, to the length of the nanotube are defined by:

$$\begin{aligned} \mathbf{k}_\perp \cdot \mathbf{c} &= 2\pi & \mathbf{k}_z \cdot \mathbf{c} &= 0 \\ \mathbf{k}_\perp \cdot \mathbf{a} &= 0 & \mathbf{k}_z \cdot \mathbf{a} &= 2\pi \end{aligned} \qquad 2.4$$

where **a** is a vector which is perpendicular to the chiral vector **c** and is along the length of the nanotube. The hexagonal lattice in real space also forms a hexagonal pattern in reciprocal space, see Figure 2.4a. This hexagonal lattice can be described by the lattice vectors $\mathbf{k}_1$ and $\mathbf{k}_2$. The band structure of graphene is shown in Figure 2.4b. It can be seen that the occupied bonding π and the empty anti-bonding π* states only meet in one point, that is in the K point in the corner of the Brillouin zone. Consequently, the Fermi level is located at this energy.

Since the electronic transport is dominated by the states close to the Fermi energy, these K points are the most important ones.

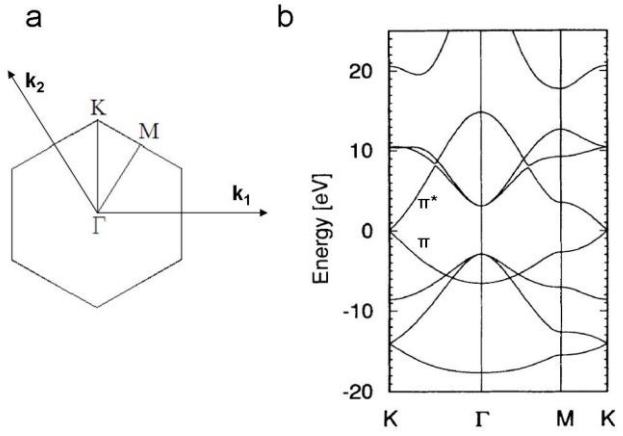

Figure 2.4. a, The first Brillouin zone of graphene showing the K, M and Γ points together with the reciprocal lattice vectors $\mathbf{k_1}$ and $\mathbf{k_2}$. b, 2D representation of the dispersion relation of graphene. It can be seen that the bonding π and anti bonding π* bands only meet in the K point. Adapted from [13].

This changes when the graphene sheet is rolled to form a nanotube. The wavevector along the tube axis, $\mathbf{k_z}$, is not affected since the nanotubes are relatively long. The diameter, on the other hand, is normally very small which means that the circumference can be very short. The wavelength and the wavevector along the circumference must therefore satisfy the boundary conditions:

$$m\lambda = |\mathbf{c}| = \pi d$$
$$\boldsymbol{k}_{\perp,\mathbf{m}} = \frac{2\pi}{\lambda} = \frac{2\pi}{|\mathbf{c}|} m = \frac{2}{d} m, \qquad 2.5$$

where m is an integer, λ the wavelength and $\mathbf{k}_{\perp,\mathbf{m}}$ the wavevectors along the circumference of the nanotube. Consequently, the wavevector is quantised along the circumference. The allowed electronic states of the nanotube therefore form parallel lines along the tube axis in the reciprocal space.

As a first approximation, the electronic properties of carbon nanotubes can now be found by comparing these quantised wavevectors with the continuous situation in graphene. This can be represented as in Figure 2.5, where the allowed wavevectors for a metallic and for a semiconducting nanotube are plotted together with the first Brillouin zone of graphene.

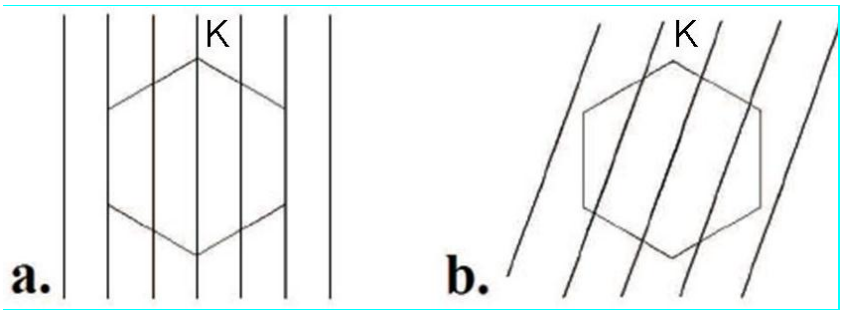

Figure 2.5. Reciprocal lattice of graphene together with the quantised wave vectors of (a) a metallic nanotube and (b) a semiconducting nanotube.

The density of states can be obtained from this and is shown in Figure 2.6 [14]. It can be seen that the quantisation of the wavevectors leads to a density of states with many sharp peaks, known as van Hove singularities.

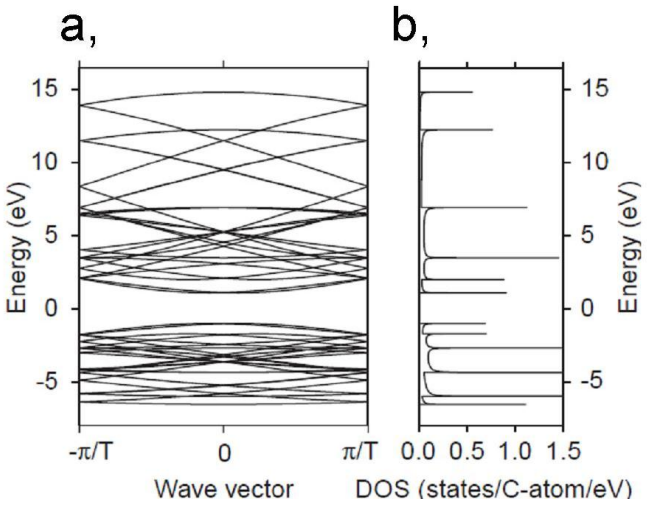

Figure 2.6. (a) shows the band structure and (b) the density of states for a semiconducting nanotube. This represents a semiconducting nanotube since there are no states around the Fermi level. Adapted from [14].

In metals, the density of states is non-zero around the Fermi level. Since the bonding and anti-bonding π-bands in graphene only meet at one point, the K point, one of the quantised wavevectors in nanotubes must coincide with this point for the nanotube to be metallic. This can be used to find a condition for the nanotube to be metallic by using equation 2.5 and the fact that the K point of graphene is located at 1/3 ($\mathbf{k}_1$-$\mathbf{k}_2$) (see Figure 2.4a):

$$2\pi m = \mathbf{K}\mathbf{c} = \frac{1}{3}(\mathbf{k}_1 - \mathbf{k}_2)(n_1\mathbf{a}_1 + n_2\mathbf{a}_2) = \frac{2\pi}{3}(n_1 - n_2) \qquad 2.6$$

This can be rearranged to give:

$$n_1 - n_2 = 3m \qquad 2.7$$

Consequently one third of all nanotubes are metallic, see Figure 2.7.

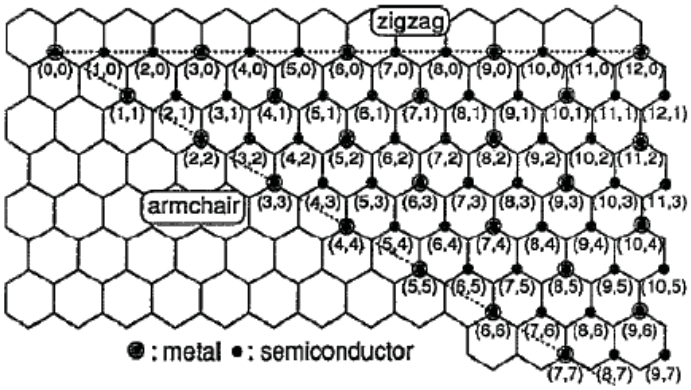

Figure 2.7. Possible chiral vectors for nanotubes. The larger dots represent metallic nanotubes whereas the smaller ones represent semiconducting nanotubes. [15]

The two thirds of nanotubes that do not satisfy this expression have no energy states at the Fermi energy. These nanotubes therefore have an energy gap between the occupied bonding π- and the unoccupied π*-bands and are consequently semiconducting, see Figure 2.8. The bandgap of these semiconducting nanotubes is proportional to the inverse of the diameter and is about 0.5 eV for a SWCNT with a diameter of 1.4 nm [16].

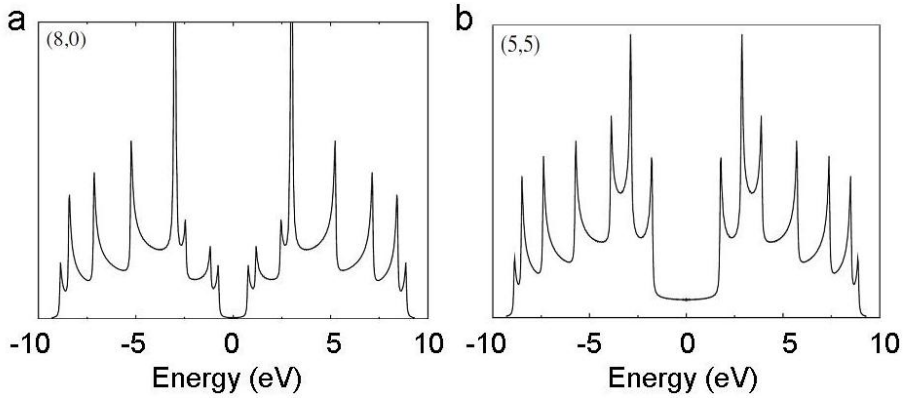

Figure 2.8. The density of states for a semiconducting (8,0) and a metallic (5,5) nanotube. A bandgap appears around the Fermi energy in a, which thus represents a semiconducting nanotube. The density of states at the Fermi energy is non-zero in b, which thus represents a metallic nanotube. Adapted from [17]

This explanation assumes that the band structure does not change when the graphene sheet is rolled. This is not correct since the bending of the bonds in the graphene sheet causes a mixing of the s and p states of the carbon atoms. The bonding and anti-bonding π bands therefore meet in a point shifted from the K point. This shift is small and does not influence the semiconducting nanotubes significantly since the quantised wavevectors are further away from the K points than this shift. It can, however, be important for the metallic nanotubes as a small bandgap appears for nanotubes where n_1-n_2 = 3m and m ≠ 0. This bandgap scales as one over the diameter squared and is about 10 meV for a nanotube with a diameter of 1.4 nm [16]. At room temperature this shift is therefore smaller than the thermal energy, 25 meV. Consequently, it becomes important only at low temperatures. The armchair nanotubes (n,n) are not affected at all and can therefore be said to be truly metallic.

2.3 Synthesis methods

Carbon nanotubes can be synthesised by a few different methods. The method that was used by Ijima was arc-discharge [1], where a high DC voltage is applied between two graphite rods, see Figure 2.9. Carbon atoms are evaporated and form many different carbon structures. Mainly multi-walled nanotubes can be found in this soot, but by adding a small amount of metal catalyst single-walled nanotubes can also be formed. More information on the arc-discharge method can be found in [18].

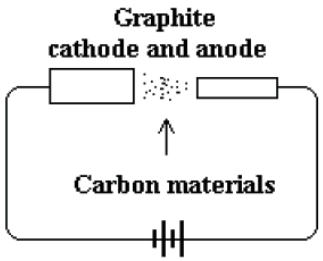

Figure 2.9. Schematic of the setup used in the arc discharge technique.

Laser ablation is another method used to produce carbon nanotubes. This technique is also based on evaporation of a graphite source material, but instead of an electric arc, short laser pulses are used to ablate a graphite source inside a furnace heated to about 1000 °C, Figure 2.10. The nanotubes are transported to a cold finger by inert gases where they condense. The laser ablation technique is further discussed in [19].

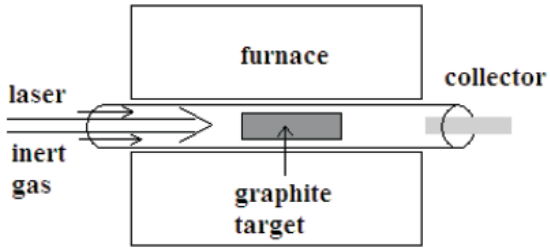

Figure 2.10. Schematic of the setup used in the laser ablation technique.

Both these techniques can produce carbon nanotubes of high quality due to the high formation temperature. Since a large amount of amorphous carbon and clusters also are formed, a purification step is often necessary. This step might damage the nanotubes. The nanotubes are usually dispersed in a solvent and can be either randomly deposited or deposited with some degree of control on a substrate. Dielectrophoresis [20] and fountain-pen lithography [21] are examples of some of the more controlled methods.

Chemical vapour deposition, CVD, is the most widely used technique to synthesise carbon nanotubes. Instead of using high energy to extract the carbon atoms from graphite targets, this method relies on decomposition of carbon-containing gases on metallic catalysts. One of the advantages with this method is that the nanotubes can be grown directly on a substrate. The location of the nanotubes can be controlled very accurately by only depositing the catalyst where the nanotubes are desired.

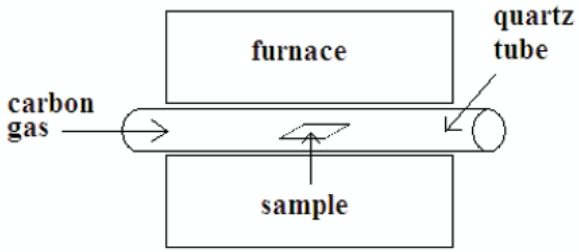

Figure 2.11. Schematic of the setup for chemical vapour deposition, CVD.

Many different variations of this technique exist, but the general principle is very similar in all of them. A nanometre thin metal film is first deposited on a substrate and then transferred to a furnace where the temperature and atmosphere can be controlled. The metal film oxidises during this transfer. The sample is heated to 600-1000 °C in for example hydrogen and argon atmosphere. The metal film is reduced during this process and breaks up into nanoparticles. A carbon-containing gas is supplied, which decomposes on these nanoparticles and leads to carbon nanotube growth. A schematic of a typical setup is shown in Figure 2.11.

One alteration is that the nanoparticles can be deposited in different ways, for example by deposition of pre-prepared nanoparticles by spin coating [22]. The heating process can also be varied in numerous ways by adding another heat source, for example hot filament CVD [23], radiation-heated CVD [24, 25], laser assisted CVD [26] and plasma enhanced CVD [27-30]. Local or resistive heating CVD where the furnace is replaced by a small local heat source is investigated in this thesis and will be discussed further in chapter 2.3.1, below, and in Chapter 3.

2.3.1 Resistive/Local heating CVD

Historically, all components in electronic devices have been made smaller and smaller in order to improve the performance. This is becoming more and more difficult and more problems appear, such as electromigration of the copper wires. The ITRS roadmap highlights problems that need to be solved for the rapid technological improvement to continue [31]. The exceptional properties of carbon nanotubes make them interesting as a solution to some of these problems, but the processing temperature needs to be kept below about 450 °C in order to be compatible with microelectronic fabrication. For example, diffusion of dopants or thermal stresses can damage the material at higher temperatures. The nanotubes can be grown *ex situ* and deposited on the substrate after the growth, but it would be a great advantage if the nanotubes could be grown directly on the substrate at predefined locations and only there. This is possible with the CVD method, but then the growth temperature has to be kept below 450 °C.

It has been shown that nanotubes can be grown at low temperatures [5] but the quality is generally rather low or the growth results in nanofibres instead of nanotubes [6]. A way around this problem is, instead of using a furnace which heats up the whole substrate, to create a small heater on the substrate which only heats a small part of the sample. A few groups have investigated this using different geometries and heater material, as will be discussed below, but the ideas are similar.

Englander *et al.* used suspended heaters made of silicon to grow both carbon nanotubes and silicon nanowires [32]. The temperature at the centre of the heater was found to be too high for nanowire growth, whereas it was too low on the sides, see Figure 2.12. Consequently, the nanowires were grown in localised regions close to the middle of the heater where the temperature was high but not too high. This effect was not as pronounced for nanotube growth.

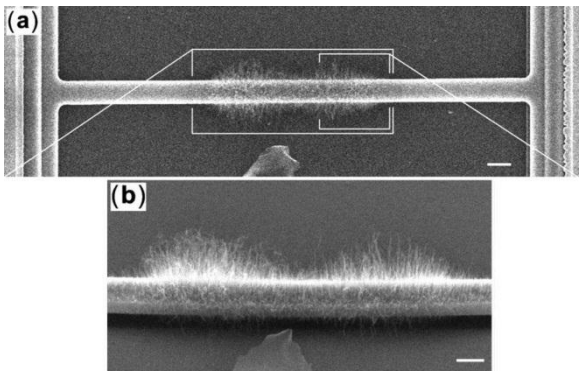

Figure 2.12. The local heater used in ref. [32] to grow silicon nanowires. The central part is too hot for nanowires to grow. The growth is therefore maximised approximately 10-15 µm to the sides. b is a zoomed and tilted image of the structure in a. The scale bars are 5 µm long. Adapted from [32]

A second electrode was added in order to control and monitor the growth better [33]. An electric field (1.3 V/µm) was applied to align the nanotubes. The nanotubes grow towards the second electrode and by connecting this to a multimeter, a signal is detected when the nanotubes reach the electrode. Connections of single nanotubes could thus be made by stopping the growth when a signal is first recorded. This gives information about the growth rates. More nanotubes would connect the electrodes for longer growth times.

Jungen *et al.* used a similar technique with heaters made of polysilicon [34]. They found that thinner nanotubes (< 20 nm) grew at locations with higher temperature and bundles of SWCNTs or thick MWCNTs grew in the colder regions.

Since these heaters are suspended there is no interaction with the substrate during the synthesis, but it also adds additional microfabrication steps.

The heaters can also be placed in series or in parallel in order to grow more nanotubes simultaneously at different locations. Nagato *et al.* grew WO_2 nanowires on an array of 20 x 20 tungsten heaters [35].

In most experiments, one single carbon-containing gas is used as precursor. This gas breaks up into fragments or oligomerises at elevated temperatures before reaching the substrate [36, 37]. Hart *et al.* used a local heating technique to investigate the influence of cold or hot gases reaching the catalyst [38]. A gas mixture of C_2H_4, H_2 and Ar was used to grow nanotubes at 810 °C. The nanotubes grew at an average rate of 7 µm/min when the supplied gases were kept at room temperature. This rate was increased to 100 µm/min by preheating the gases before they entered the growth chamber, keeping all other process

parameters identical. The quality and diameter of the nanotubes was found to be independent of this preheating process. It would have been interesting to investigate the gas species present in the chamber using the different approaches, but no such study was performed in ref. [38].

Molhave *et al.* have studied nanowire growth on silicon microbridges [39]. It was found that different epitaxial nanowires could be grown depending on the gas atmosphere. This was used to grow different nanowires on different heaters on the same chip. Silicon nanowires were first grown followed by the synthesis of gallium nitride (GaN) nanowires on another heater in a different gas atmosphere. In the second step GaN was also deposited on top of the already grown Si nanowires. The amount of deposited GaN was found, as expected, to depend on the distance from the heated microbridge, see Figure 2.13.

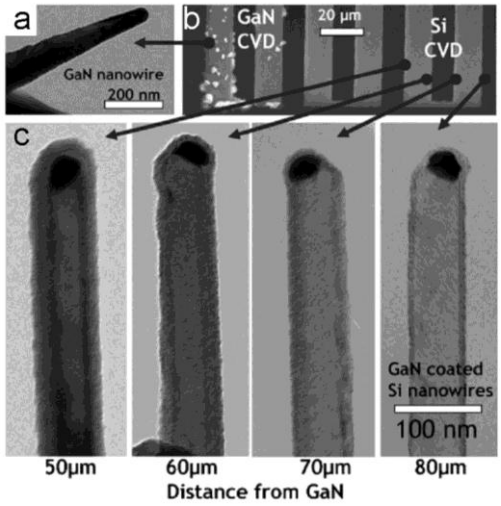

Figure 2.13. a, TEM image of a GaN nanowire grown on the heater to the left in b. b, SEM image of the heaters where Si nanowires were first grown to the right and GaN nanowires were grown to the left in a second step. c. TEM images showing that the silicon nanowires were covered by GaN that was formed during the 2nd growth. The deposited GaN layer can be seen to be thicker closer to the heater used for GaN growth. Adapted from [39].

Nanotubes have also been grown directly on AFM cantilevers using a local heating technique [40]. The mass of the grown nanotubes could be estimated from the change in resonance frequency before and after the growth. This resulted in a mass of about 1.4×10^{-14} kg. This technique could be used to create sharp tips for AFM. Unfortunately, the authors say that the fabrication process is too complex to replace the common silicon or silicon nitride cantilevers.

Micro heaters can also be buried in the substrate [41]. Micro-hotplates were created by placing tungsten electrodes a few microns below the surface with catalyst, see Figure 2.14. A current was sent through these so that the temperature at the catalyst was 725 °C. Acetylene was introduced into the system at this temperature, yielding carbon nanotube growth. Using this technique and by electrically connecting many of these micro-hotplates, nanotube growth could be achieved on a wafer scale. This technique was used to produce sensors [42], which were found to be able to detect methane. The selectivity was not discussed.

An IR (infra-red) camera was used to measure the temperature distribution on the chip [41]. These measurements were compared with ANSYS simulations. The maximum temperature that could be investigated with this equipment was 250 °C. It was found that the temperature dropped to ~100 °C approximately 50 μm outside of the hotplates, when they were heated to 250 °C. There was no discussion about what temperatures could be expected around the hotplates when they were heated to the 500 °C hotter growth temperatures. It was shown that transistors placed on the same chip still functioned after the nanotube growth, but these were placed far away from the micro-hotplates.

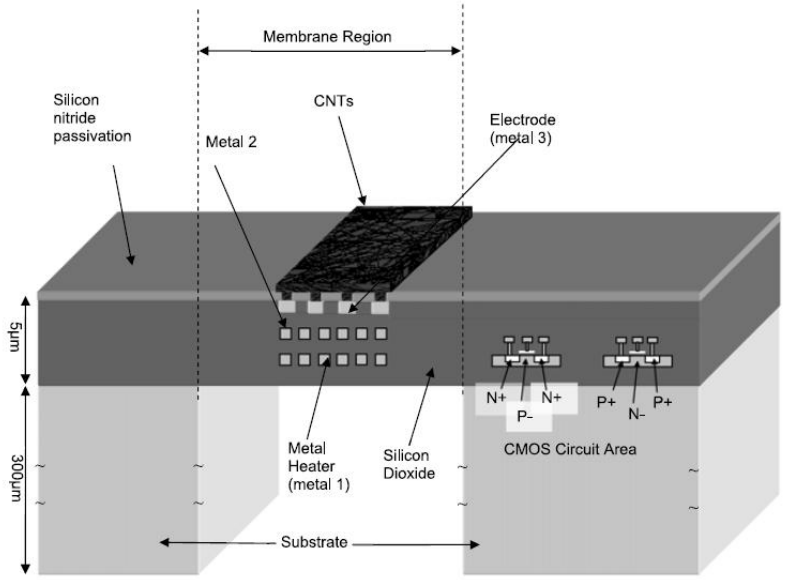

Figure 2.14. The local heating structure used in ref. [41]. The heater is located a few microns down from the surface in the silicon nitride layer. [41]

Suspended silicon heaters have also been fabricated to yield a temperature gradient along the heater [43]. The temperature could accurately be measured by monitoring the shift of the Si peak around 520 cm^{-1} in the Raman spectrum. The temperature was also measured and controlled by monitoring the conductivity of the Si heater using a four-point geometry.

The structure is shown in Figure 2.15. Nanotubes were grown in the temperature range 575-800°C. The length of the nanotubes gradually increased in this temperature interval. The length of the nanotubes rapidly decreased at even higher temperatures. Raman spectra were recorded along the temperature gradient and the G/D ratio was found to increase for higher temperatures. This implies that more defective or multi-walled nanotubes were grown or that more amorphous carbon was deposited at lower temperatures. See chapter 4.2 for more information about Raman spectroscopy and the G/D ratio.

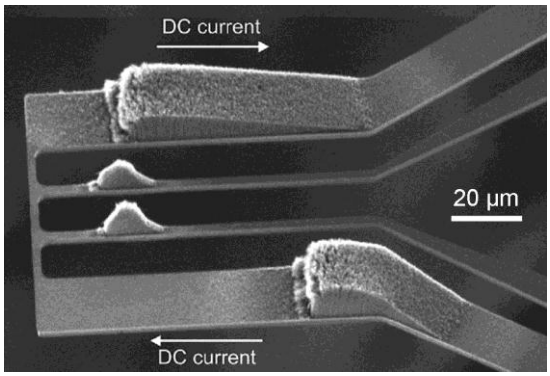

Figure 2.15. The design used in ref. [43]. The current was sent through the wider top and bottom electrodes. The thin metal wire became hot enough to heat the thinner electrodes to nanotube growth temperatures. The height difference of the nanotubes is due to a temperature gradient with higher temperatures on the left hand side. [43]

The power consumption is significantly reduced in the local heating method. The power depends on the actual material and geometry, but is typically <1 W. The power is usually not stated in most papers on conventional CVD growth, but the furnace in our lab has a maximum power of 2 kW. The plasma power in plasma-enhanced CVD is typically around several tens of watts or around 100 W [28, 44].

A review of the local heating growth technique focused on its application to growth of carbon nanotubes and nanowires can be found in ref. [45].

One advantage of this technique is that since no large furnace is required, the growth chamber can be made very small. It can be made small enough to be put inside a Raman spectrometer, allowing *in situ* studies of the growth. This will be discussed more in Chapter 6.

Chapter 3 Experimental techniques

Most of the nanotubes in this thesis have been synthesised using a local heating CVD technique. The nanotubes are grown on a small metallic electrode, which is resistively heated by sending a current through it. The metal is deposited in a design that only yields a high temperature locally at the catalyst. This is done by making the electrode narrower where a high temperature is desired. This smaller part will from now on be referred to as the heater. The heater is connected to 4 contact pads in order to allow 4-probe measurements. One of the designs is shown in Figure 3.1.

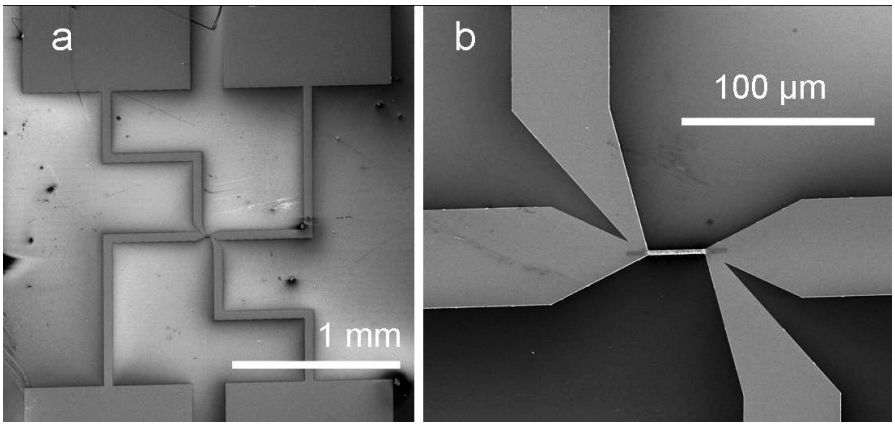

Figure 3.1. SEM images of the layout of the samples. The small heater in the centre is connected to four large contact pads enabling electrical contact. b, is a zoomed-in image of the centre of a.

3.1 Microfabrication

Most of the samples are made of n-type silicon with a layer of 0.4 or 2 µm silicon dioxide on top. The samples used for high frequency measurements in Chapter 8 were made in a different way. The reason for this is that a layer of electrons would build up between the silicon and the oxide layer, which would lead to losses along the transmission line [46], and would therefore interfere with the measurements. These samples were therefore made using wafers of p-type high-resistivity silicon (resistivity >9000 Wcm) with a layer of 200 nm polysilicon and 400 nm silicon dioxide on top. The polysilicon layer removes the problem of charges building up between the silicon and the oxide.

In general, patterns are created on a substrate using either photolithography or electron beam lithography in combination with either etching of the unwanted material or a lift-off process. In both lithography techniques, a polymer is spun onto the substrate. When

irradiated by light or electrons, this polymer either becomes soluble (positive resist) or insoluble (negative resist) in a developer. Consequently, a pattern can be formed in the resist/polymer by only irradiating parts of it followed by removing either the exposed (positive) or unexposed (negative) resist. In photolithography this is done by shining light through a mask that only lets through light in the desired pattern. In electron beam lithography the pattern is formed by only deflecting the electron beam to expose the polymer in the desired pattern. The pattern can now be transferred to the layer underneath the resist by etching the exposed part, leaving the covered parts intact. In the lift-off process the desired material is deposited on top of the resist and in the exposed parts of the substrate. By then exposing the sample to a solvent that removes the resist but leaves the deposited material, this forms a layer of the desired material in the pattern designed in the lithography process.

Here the lift-off process is used in combination with electron beam lithography. Two layers of photoresists are spun onto the sample in order to improve the lift-off process. The lower of the two resists is developed at a faster rate than the top layer. This is done so that an undercut will be formed such that the top layer hangs out at the edges of the pattern. The principle behind the whole process is shown in Figure 3.2.

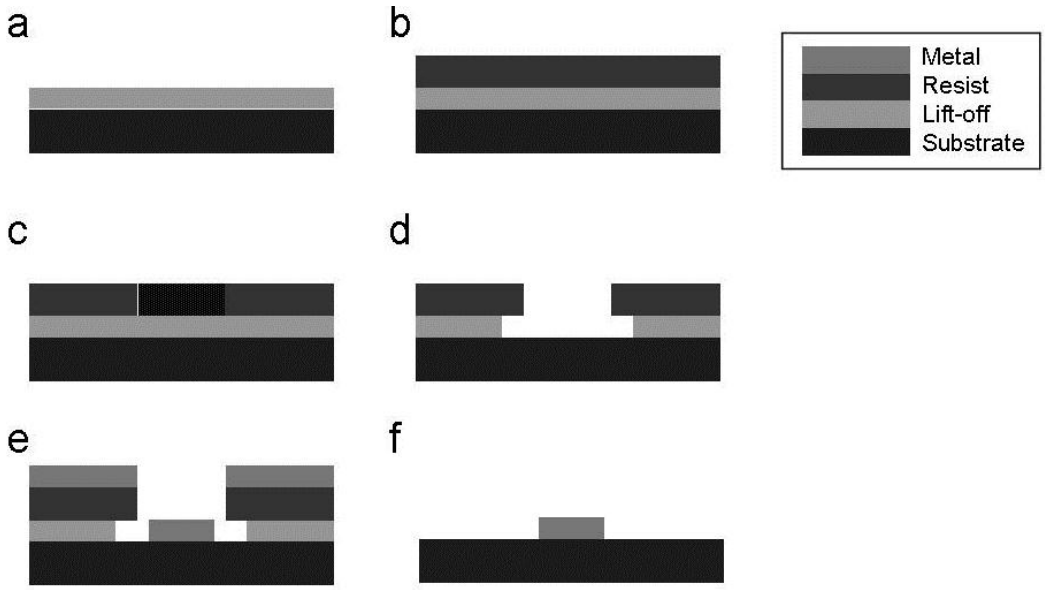

Figure 3.2. Illustration of the basic steps in the micro fabrication process. a, A lift-off resist is first spun onto the sample and baked. b, This is followed by spinning and baking of the resist layer. c, The resists are exposed using electron beam lithography, after which the resists are developed, d. e, The desired metal is then either electron beam evaporated or sputtered onto the sample, which is followed by lift-off of the resist and undesired metal, leaving the desired metal in the required pattern, f.

The metal film is deposited over the whole wafer after this process using electron beam evaporation. Here molybdenum is used since it has a high melting point (2880 K [47]) and is compatible with nanotube growth. The Mo layer is typically 100 nm thick. The heater is typically patterned to be 30 µm long and 2 µm wide. This is connected to 4 large contact pads to allow electrical contact and 4 point measurements. The connections between the heater and these pads are 50 µm wide in order to have a small resistance compared to the heater, and thereby not be heated when a current is sent through it. A layer of 5-10 nm Ti is deposited under the Mo as an adhesion layer. The catalyst is deposited in a subsequent step using the same process but a different pattern. 1 nm Fe with a supporting layer of 5 nm Al_2O_3 is typically used. This supporting layer is used to prevent sintering of the catalyst particles [29]. The choice of these thicknesses of support and catalyst layer is further discussed in Chapter 5. The catalyst was deposited as a series of stripes with a width of 0.5 µm and a length of 2 µm. These were typically separated by 0.5 µm, but some samples were made with only 2 or 3 catalyst stripes.

TiN was also tried as an alternative to the Mo in order to improve the electrical contact between the nanotubes and the electrode. No supporting Al_2O_3 layer was required in this setup. The TiN started "burning" when heated to a few hundred degrees, see Figure 3.3. The temperature was still too low to yield a reasonable blackbody signal. The figure shows snapshots from a movie recorded of a heater made of 7 nm Ti and 200 nm of TiN when heated in an Ar atmosphere. This "burning" could be due to the TiN being more sensitive to small amounts of oxygen leaking into the chamber. Since the heater is destroyed at temperatures lower than where nanotubes can be grown, these heaters could not be used for nanotube growth.

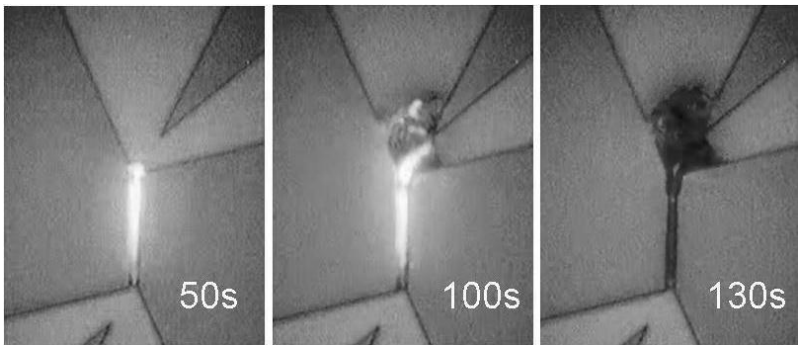

Figure 3.3. The heater is made of TiN and is heated to a few hundred degrees. The heater and the connecting electrode is gradually destroyed at temperatures significantly lower than where nanotubes can be grown.

The metal evaporation is performed at a base pressure of 10^{-6} mbar. The evaporation sources have a purity of ≥ 99.5 % and the thickness is monitored with a quartz crystal oscillator.

Sputtering is used instead of electron beam evaporation for the samples in Chapter 8 since it was found that sputtered Mo yields a resistivity one order of magnitude lower than that of electron-beam-evaporated molybdenum thin films, which is beneficial for the electrical measurements.

The thickness of the metal must be less than the thickness of the resist so that the metal deposited on the silicon is not in contact with the metal deposited on top of the edges of the resist. The resist, and consequently the metal on top of it, is then removed by a heated solvent. It is sometimes necessary to ultrasonicate the wafer for a couple of minutes to make sure that the excess metal and all resist is removed. Details of the process can be found in Appendix A.

Since the contact pads are large (almost 1 mm^2) but the heater itself needs to be smooth on a much smaller scale, a combination of photolithography and electron beam lithography could be used in order to save time and money for a larger scale production.

3.2 Growth procedure

The sample was placed in a growth chamber and needles were attached to the contact pads, see Figure 3.4. The chamber has a quartz window and a volume of about 200 cm^3. Two sourcemeters, Keithley 2611 and 2410, were connected to the contact pads, one to send a current through the heater and one to measure the potential drop over it. A LabVIEW program was written to control the current and to monitor the voltage drop. The program is attached as Appendix D. The chamber is placed under an optical microscope in order to allow optical video recordings and *in situ* Raman measurements. The objective has a magnification of x50 with a numerical aperture of 0.45 and a working distance of 15 mm. Figure 3.5 shows a schematic diagram of the setup with growth chamber, gas lines, electrical connections and the Raman spectrometer.

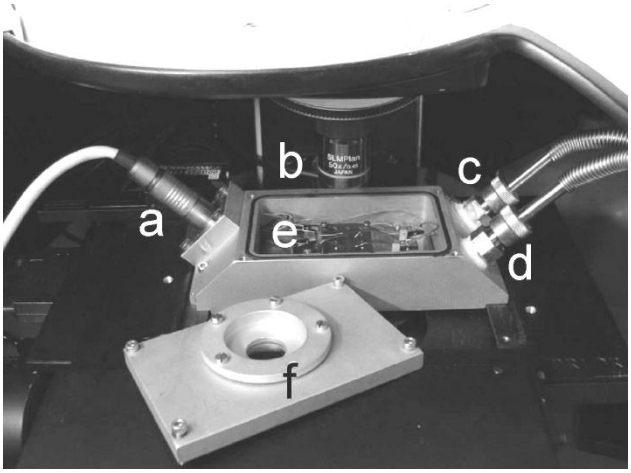

Figure 3.4. Photograph of the chamber used for local heating growth. a, electrical feedthrough, b, 15 mm long working-distance objective with 50x magnification, c, gas outlet and pump line, d, gas inlet, e, sample stage with contact needles, f, upper lid with optical port.

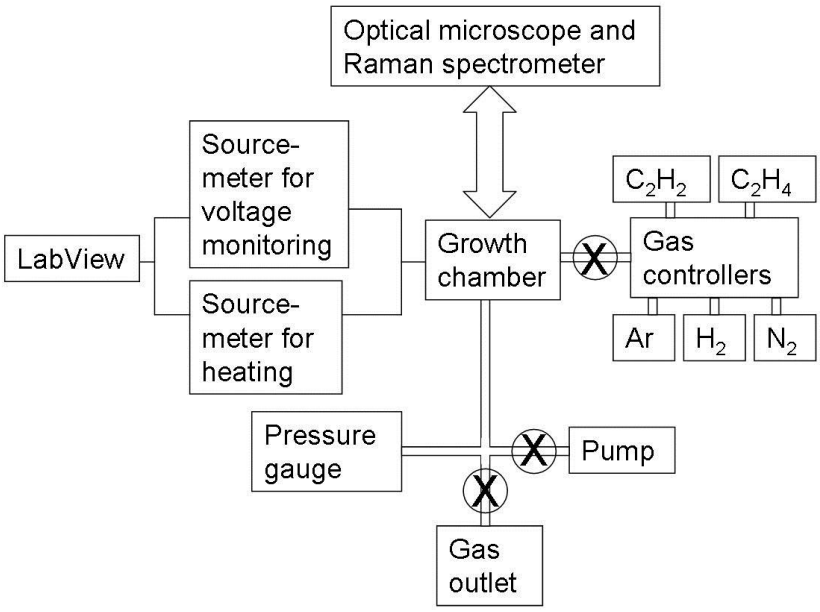

Figure 3.5. Schematic of the setup of the growth chamber, gas lines, electrical connections and the Raman spectrometer.

The chamber is first evacuated and filled with Ar twice in order to remove the air. The chamber is then filled with Ar, 500 sccm, and H_2, 300 sccm. When the pressure is just above the ambient an exhaust line is opened. This is in order to ensure that no gases are allowed to leak back into the chamber when the valve is opened. The current through the metal strip is thereafter ramped up stepwise in a current-limited mode as controlled by the LabVIEW program. The current and voltage time evolution can be seen in Figure 3.6. In the beginning,

the voltage across the heater follows the current increase as expected from Ohm's law (U=RI). After about 60 seconds this behaviour stops and the voltage does not vary as much, as shown in Figure 3.6. This is due to changes in the structure of the heater and thereby also the resistance. These changes are irreversible, as can be seen when the current is decreased and an ohmic behaviour is found. The resistance of the heater increases when the carbon feedstock reaches it, as can be seen after about 300 s in Figure 3.6. This is due to carbonization of the heater. The voltage drop thereafter slowly decreases due to annealing and restructuring of the heater.

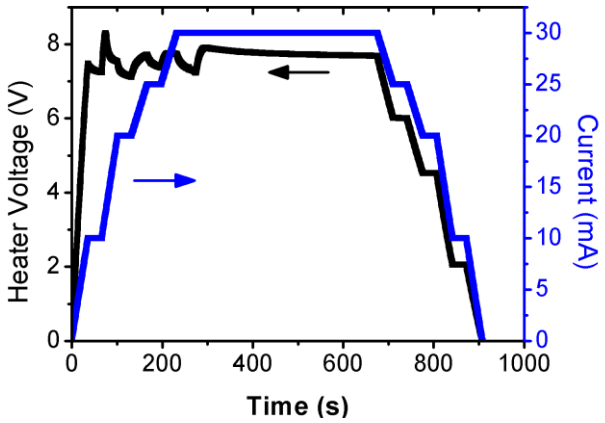

Figure 3.6. Typical time evolution of the voltage drop over the heater and the current through it. In this particular case the current is kept constant at 30 mA during growth. The voltage can be seen to increase when the carbon precursor is introduced after approximately 300 s. This is attributed to carbonisation of the heater.

The carbon precursor, ethylene or acetylene, is supplied at a significantly lower flow rate than the flow rates of argon and hydrogen, and is typically 6 sccm. Using ethylene, mainly SWCNTs are grown whereas mainly MWCNTs are grown when acetylene is used as carbon feedstock. Studies of the carbon nanotube growth are discussed in Chapter 5 and Chapter 6.

3.3 Temperature estimations

The temperature is a very important factor in nanotube growth. It is tricky to measure the temperature at the micro scale. The small thermal mass of the system makes any contacting probes useless since they would influence the temperature itself [48]. The

electrical resistance of the heater cannot be used either since the heater is chemically modified during the CVD process, which changes the resistance.

The method used here is to study the blackbody radiation from the heater. The intensity of light emitted by a blackbody is described by Planck's blackbody formula;

$$I(\lambda, T) = 2hc^2 \lambda^{-5} (e^{hc/\lambda k_B T} - 1)^{-1}, \quad 3.1$$

where h is Planck's constant, c the speed of light, λ is the wavelength, k_B is Boltzmann's constant and T is the temperature. The spectrometer was calibrated using a tungsten lamp with a known emission spectrum. The known and the measured spectra are shown in Figure 3.7a. These were used to create a transfer function from a measured to a real spectrum, shown in Figure 3.7b.

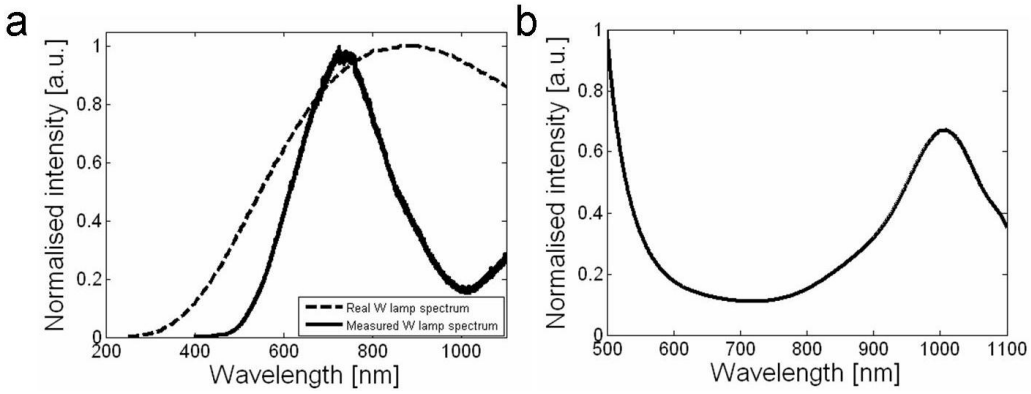

Figure 3.7. a, Real and measured spectrum of the tungsten calibration lamp. b, transfer function calculated from the difference between the measured and the real spectra of the tungsten calibration lamp.

Spectra of emission before and after correction with the thus obtained apparatus function of the system are shown in Figure 3.8a. By using Wien's approximation ($hc >> \lambda k_B T$) and rearranging the blackbody formula, it is found that $-\ln(I\lambda^5) \propto 1/\lambda T$. Consequently, the temperature can be found by determining the inverse gradient in a plot of $-\ln(I\lambda^5)$ versus $1/\lambda$, see Figure 3.8b.

Since the heater is not a true black-body we make the grey-body assumption that the emissivity does not change significantly over the wavelength range of interest. A wavelength range of 700-900 nm is typically used for temperature measurements since the emission intensity is low at short wavelengths and the detector efficiency drops rapidly at long wavelengths.

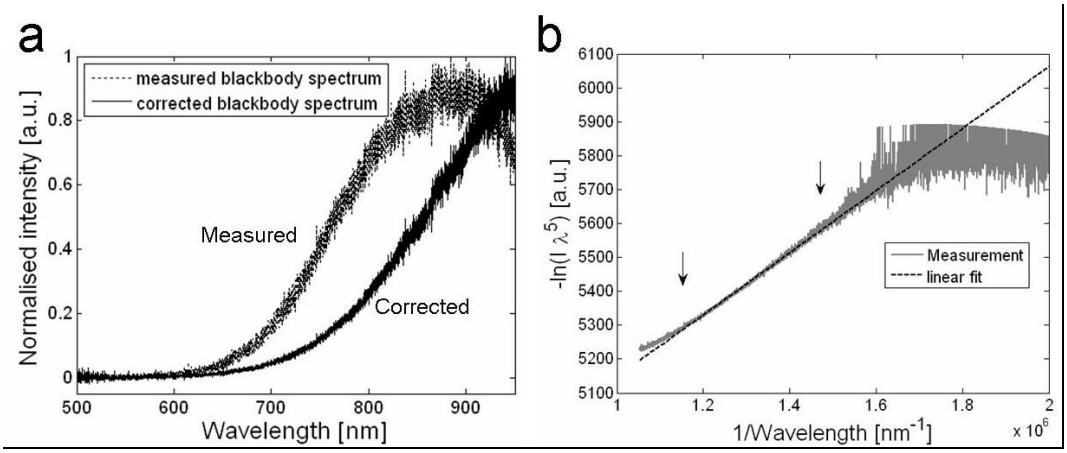

Figure 3.8. a, blackbody spectra before (grey) and after (black) calibration with the tungsten lamp. b, corrected spectrum in Wien's coordinates showing the straight line fit used to extract the temperature. The arrows indicate the fitted region.

Using this technique we found that the temperature range for nanotube growth is the same as in conventional CVD, approximately 600-900 °C. This is the temperature of the heater before the carbon precursor has reached the heater. Blackbody measurements were done in order to study how the addition of the carbon gas influences the temperature as well as to investigate the influence of cooling by the nanotubes. These measurements were performed on heaters with three small catalyst islands to avoid screening by the nanotubes. For a specific sample and current, the temperature just before the acetylene was introduced was found to be 750 °C, see Figure 3.9. The introduction of C_2H_2 then increased the temperature to 840 °C, after which there is an indication that it slowly dropped. This increase is related to carbonization of the heater, which increases its resistance as can be seen in Figure 3.6. The temperature of the heater is related to the supplied power, P;

$$P = I \times V = I^2 \times R, \qquad 3.2$$

where I is the current through the heater, V is the voltage over it and R is the resistance of the heater. Consequently, this increase in resistance leads to an increase in power and thereby also an increase in temperature. The small drop in temperature after the second measurement in Figure 3.9a is related to annealing of the heater which reduces the resistance, as can be seen in Figure 3.6, and thereby also the temperature. The same trend is observed when ethylene is used instead of acetylene and also for a heater without any deposited catalyst.

The temperature closer to the catalyst and the nanotubes was measured after about 5 min, and was found to be 800 °C. The temperature in the middle between the catalyst islands

was found to be 70 °C higher. These variations are due to the cooling effect of the nanotubes growing into the cold gas atmosphere.

The temperatures given in the cold gas atmosphere throughout the thesis are the temperatures of the heater determined just before the carbon precursor is introduced, unless otherwise stated.

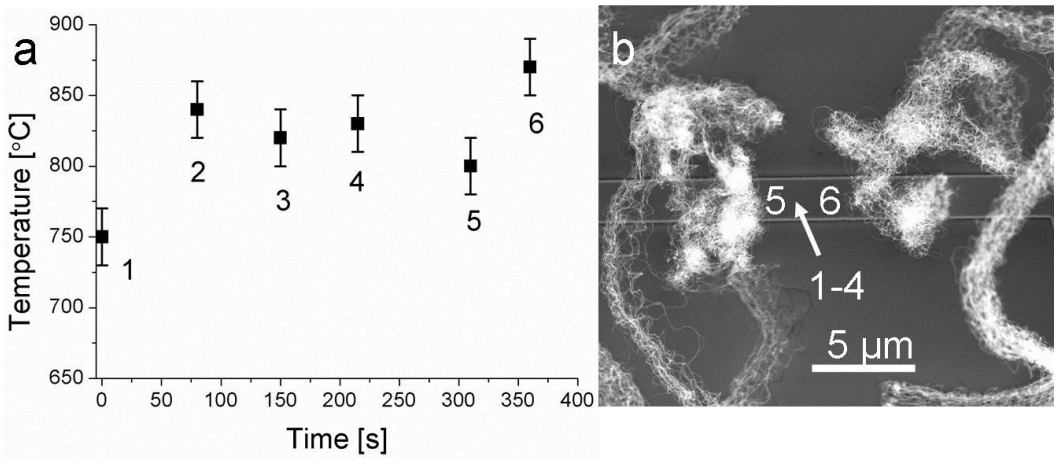

Figure 3.9. a, Temperature of the heater as a function of time. The first point is when the current has reached its maximum but before the carbon feedstock was turned on. The three following points are in the same spot , marked 1-4 in b, but after the introduction of the carbon feedstock. The fifth point after about 5 min is measured closer to the catalyst, labelled 5 in b, whereas the last point is measured in the middle between the catalyst islands, marked 6 in b.

3.4 Capacitance measurements

The capacitance of the vertically aligned carbon nanotube array devices in Chapter 8 was found by measuring the S-parameters from radio frequency experiments. The S-parameters are scattering parameters similar to the transmission and reflection coefficients in optics. More information about basic S-parameter theory can, for example, be found on the Agilent Technologies homepage and in their handbook [49]. The system was modelled by an equivalent electrical circuit. The response of the model was compared with the measurements using the capacitances and resistances as fitting parameters

Radio frequency (rf) signals with frequencies from 200 MHz to 1.5 GHz were applied to the devices using a probe station connected to an Agilent 5071B network analyser. These AC signals were separated from the DC signals required for actuation using a bias tee. This

is basically an electrical device with one input and two outputs. One of the outputs has a capacitor, which stops all DC signals, whereas the other has an inductor, which stops all AC signals. The DC actuation voltages will consequently not influence the rf measurements.

The samples were designed as two opposing T-shaped electrodes with the catalyst deposited at the top of the T shapes. The area of these electrodes was minimised and large shielding electrodes were deposited around these in order to reduce the parasitic capacitance and optimise the capacitance measurements [50], see Figure 3.10. These shield electrodes were grounded by the ground-signal-ground (GSG) probes that were used to contact the coplanar waveguide (CPW)- shaped electrodes. The devices were calibrated by a SOLT (Short-Open-Load-Thru) calibration.

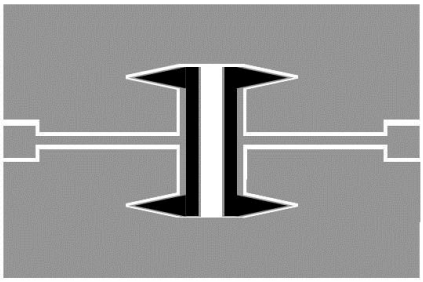

Figure 3.10. Illustration of the layout of the samples used for radio frequency measurements of the capacitance. The grey area shows the layout of the molybdenum whereas the black areas show the design of the catalyst layer.

The devices were modelled by the electrical equivalent circuit shown in Figure 3.11, using ADS (Advanced Design System) and the rf toolbox in Matlab. The simulated S-parameters of the devices were compared with the measurements, using the capacitance between the nanotube arrays, C_{CNT}, as a fitting parameter. The resistances through the transmission lines were modelled by the resistances R_1 and R_2, whereas the capacitances to the shield electrodes were modelled by the capacitances $C_{ground1}$ and $C_{ground2}$. The capacitances between the electrodes themselves were modelled by the capacitance $C_{parasitic}$. The resistances were found from THRU measurements where a short had been added between the electrodes. These samples had been exposed to growth conditions but did not have any catalyst in order to not grow any nanotubes so that values for the resistances could be found. This was also the case for OPEN samples from where the capacitances could be extracted. These capacitances might change as the applied bias voltage is increased due to interactions with the substrate. No such dependence was found here, just as Gamble *et al.* have reported for the same substrate material [46].

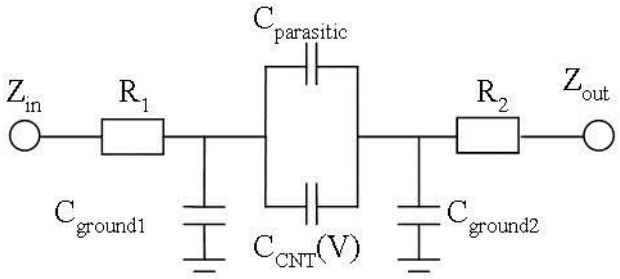

Figure 3.11. Equivalent circuit used to model the devices. $C_{CNT}(V)$ is the active varactor device, the capacitance between the nanotube arrays. R_1 and R_2 are the resistances of the transmission lines, $C_{ground1}$ and $C_{ground2}$ are capacitances to the grounded side electrodes and $C_{parasitic}$ is the capacitance between the electrodes on which the nanotubes are grown.

Chapter 4 Characterisation techniques

4.1 Scanning electron microscopy, SEM

Electron microscopes function in basically the same way as optical microscopes except that they use a focused beam of electrons instead of light. The main advantages of an SEM compared to an optical microscope are, for example, the much better resolution and the increased depth of focus. One possible drawback is that the surface of the sample has to be conducting in order to avoid charging of the sample. It is possible to get around this by using an environmental SEM which allows a gaseous environment in contrast to the high vacuum requirement in other electron microscopes. The gases remove the excess charge that is accumulated on insulating materials. A thin layer of a conducting material can also be deposited on top of the specimen to make it conducting.

In SEM, an electron beam is scanned across the surface of the sample by a couple of magnetic lenses. The electrons are accelerated to typically between 1 and 30 keV and are scattered in a drop-shaped region at the surface of the investigated sample, see Figure 4.1a. This results in electrons being scattered out of the sample with a distribution as shown in Figure 4.1b.

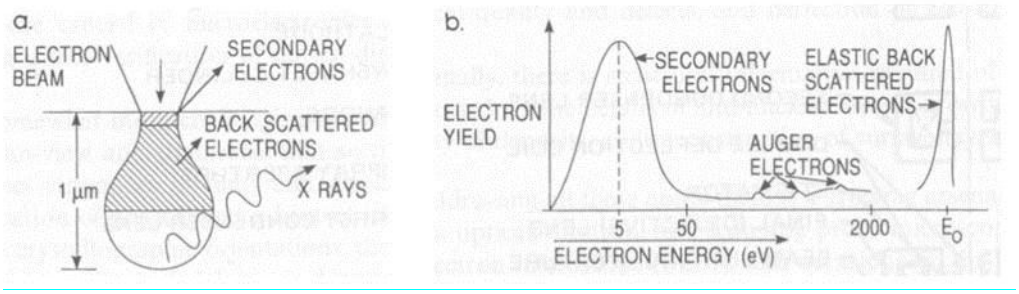

Figure 4.1. a, Electrons and photons emitted from the surface when hit by the incident electron beam. b, Energy spectrum of the electrons that are emitted from the surface. Adapted from [51]

The low energy electrons, also called the secondary electrons, are scattered from the surface of the sample, from a depth of less than a nanometre. The amount of secondary electrons depends on the topography, as can be seen in Figure 4.2. A sloping surface will yield a larger volume close to the surface than a horizontal one and will thus give a stronger signal. Detecting these electrons will therefore produce an image of the topography. This is the most common method and all SEM images in this thesis are recorded in this mode.

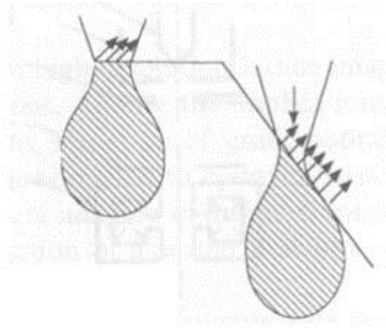

Figure 4.2. The effect of different surface topography on the amount of secondary electrons that are produced. Adapted from [51]

The high energy electrons, termed backscattered electrons, are elastically scattered further inside the sample. The amount of backscattered electrons increases with the atomic number of the sample. Since it is a quite weak dependence this is not used to identify specific elements but rather to provide contrast between regions with a large difference in atomic number. Energy-dispersive X-ray spectroscopy, EDS or EDX, can be used to chemically characterise the sample. In this technique electrons from the electron beam excite an electron from an inner shell in the investigated material, ejecting it from its shell. An electron from an outer shell can then fill this hole and thereby release the energy difference between the shells as an X-ray. Since this energy is characteristic for each element this can be used to identify what elements are present in the sample.

The resolution can be increased by increasing the acceleration voltage, but this also damages the sample more. A short working distance also improves the resolution. The emission current can be reduced in order to minimise damage to the nanotubes.

4.2 Raman spectroscopy

Raman spectroscopy has got its name from C. V. Raman who received the Nobel Prize in physics in 1930 for this discovery [52]. Landsberg and Mandelstam independently discovered the effect at almost the same time [53]. It has therefore been discussed if the discovery of the effect (and thereby the Nobel Prize) should have been shared between Raman and the Russians [54]. In Raman spectroscopy, light is shone on the investigated molecule. The light interacts with the molecule and distorts (polarises) the electron cloud around the nuclei forming a short lived excited state, called a “virtual energy state”. A photon is quickly emitted, relaxing the molecule to either the ground state or to a vibrationally excited state, see Figure 4.3. This can be seen as elastic or inelastic scattering.

The most likely process is elastic scattering, Rayleigh scattering, which is approximately 10^7 times more likely than the inelastic process, which is studied in Raman spectroscopy. Consequently, the Rayleigh light has to be filtered out. In the inelastic process, a phonon is either created, Stokes, or annihilated, anti-Stokes. The scattered photon thus has lower energy than the incoming photon in a Stokes process, and vice versa for anti-Stokes. Therefore, the molecule must be in an excited vibrational state for the anti-Stokes process to occur. The intensity of the anti-Stokes process is therefore usually significantly lower than that of the Stokes process at room temperature.

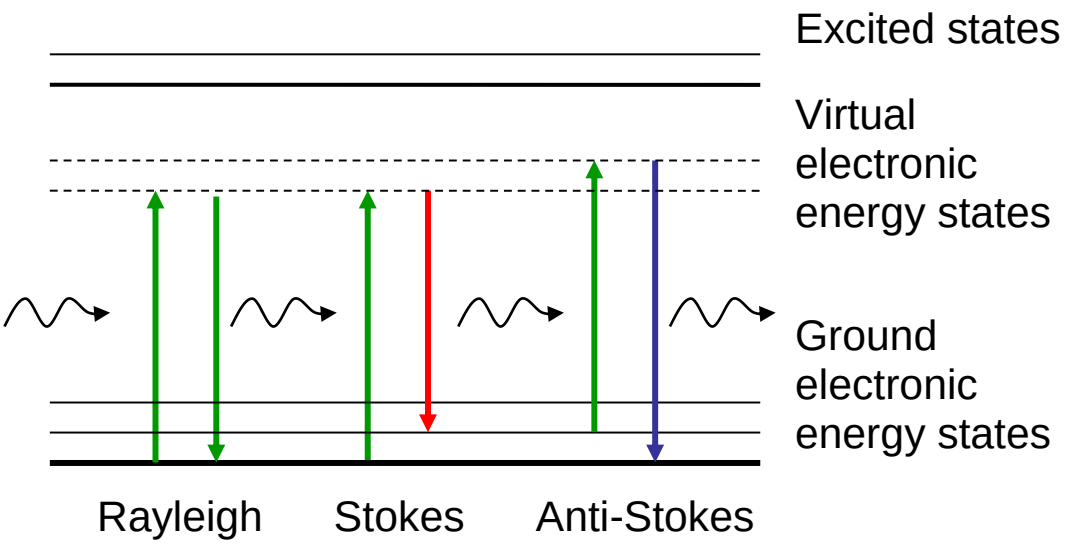

Figure 4.3. Sketch of the different Raman processes. The emitted photon has the same energy as the incident in Rayleigh scattering whereas it is lower (higher) in a Stokes (anti-Stokes) process.

The signal is significantly increased (approximately 10^3 times [14]) if the virtual excited state coincides with an actual excited state of the molecule. This is what is used in resonant Raman spectroscopy, which is the main technique used when studying carbon nanotubes.

4.2.1 Raman spectroscopy of carbon nanotubes

The density of states for carbon nanotubes consists of many sharp peaks, van Hove singularities, as described in chapter 2.2. These are very important in the Raman process. The Raman signal is significantly increased when the laser energy is equal to the difference in energy between two of these states (one in the conduction band and one in the valence

band) with the same symmetry, corresponding to a resonant Raman process. The transitions between these states are labelled E_{ii}, where i is a positive integer. The van Hove singularities are located at different energies for nanotubes with different chiralities. Consequently, only some of the nanotubes can be probed for a specific laser energy. This is often represented by a Kataura plot where the E_{ii} energies are plotted versus the diameter, see Figure 4.4.

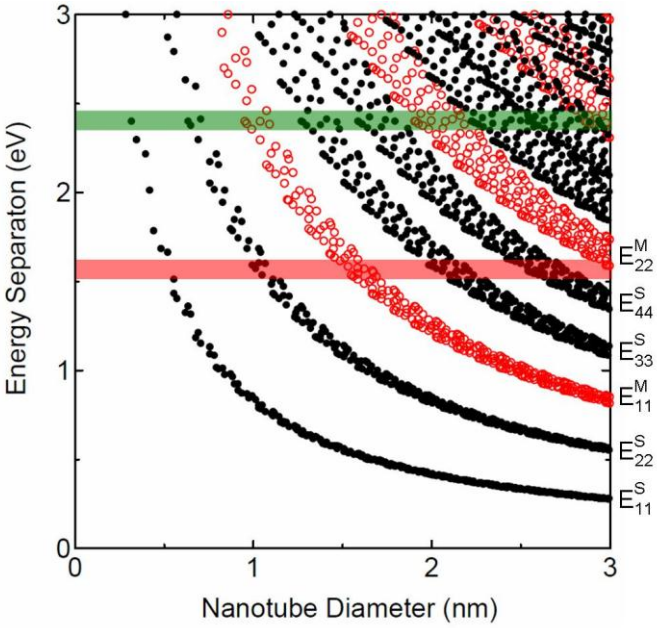

Figure 4.4. Kataura plot where each point denotes a nanotube with a specific chirality. Red circles show metallic nanotubes and the black points represent semiconducting nanotubes. The green horizontal line shows the nanotubes that are resonant with a 514 nm laser, whereas the red horizontal line shows the nanotubes that are resonant with a 785 nm excitation laser. Adapted from [55]

The largest and most important features in the Raman spectra of carbon nanotubes are the radial breathing modes (RBMs) and the D, G and G' bands, see Figure 4.5. Other smaller peaks can also be visible in the spectra, such as the intermediate frequency modes (IFMs), the iTOLA and the M band [56].

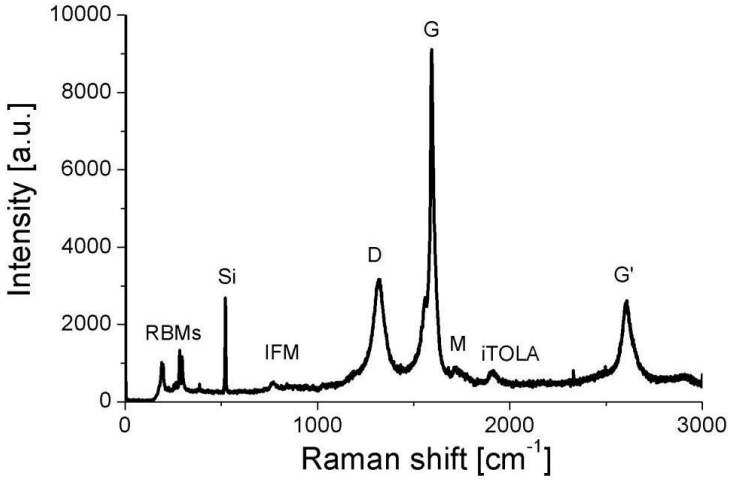

Figure 4.5, Typical Raman spectrum showing the different nanotube peaks. The spectrum was recorded using a laser excitation wavelength of 647 nm and a power density of approximately 0.05 mW/μm^2.

4.2.1.1 The radial breathing mode, RBM

The radial breathing mode, RBM, corresponds to completely symmetric vibrations of the carbon atoms in a radial direction in relation to the nanotube axis. These modes are therefore unique to carbon nanotubes and are not seen for other forms of carbon. MWCNTs where the inner tube has a diameter of less than ~2 nm can give a RBM signal, otherwise the RBMs are limited to SWCNTs because the frequency shift is too low to detect [14]. The frequency of these range from approximately 100 cm^{-1} to 400 cm^{-1}. The resonance window for these peaks is small, on the order of a few tens of millielectron volts [57, 58].

The most important feature of the RBMs is that their frequency is inversely proportional to the diameter of the nanotube. Most reported relations are of the form $\omega_{RBM} = A/d_t + B$. Many different values of the A (nm cm^{-1}) and B (cm^{-1}) parameters have been reported due to differences in the actual experimental setup. A=248 nm cm^{-1} and B=0 cm^{-1} has been reported for nanotubes on a SiO_2 substrate [59], A=218 nm cm^{-1} and B=16 cm^{-1} for nanotubes dispersed in an aqueous solution [57] and A=204 nm cm^{-1} and B=27 cm^{-1} has been found for free standing nanotubes [60]. More complicated relations have also been reported, $\omega_{RBM} = (239\text{-}5(n\text{-}m)/n)/d_t$ was, for example, found for bundled nanotubes [61]. Even if the exact values of these parameters vary, the low frequency region of the Raman spectra gives information about the approximate diameters of the present nanotubes as well as their distribution. The actual difference in diameter when using the different parameters is on the level of Å.

4.2.1.2 The G band

The G band in carbon nanotubes is directly related to the G peak in graphite (found at 1582 cm^{-1}), which originates from an in-plane tangential optical phonon. That is, stretching of the carbon atoms in the unit cell. Since the carbon nanotubes can be seen as a rolled up graphene sheet, the G band here is very similar. However, since the nanotubes are rolled the symmetry is broken and the peak splits up into several peaks where the two main peaks (G^- and G^+) originate from vibrations along the circumference and from vibrations along the axis of the nanotube respectively. The resonance window of the G peak is much broader (approximately 100 meV dependent on diameter and chirality [62]) than for the RBMs. Consequently many more nanotubes can contribute to the measured G-band intensity than to the detected RBM peaks using a specific laser energy.

The frequency of the G^- peak depends on the diameter of the nanotube and whether the tube is metallic or semiconducting [63], see Figure 4.6. The G^+ peak, on the other hand, is independent of both the diameter and the chirality of the nanotube. This was found by studying the RBMs and the G band of the same nanotube [63]. The shape of the G^- peak is also strongly dependent on whether the nanotube is metallic or semiconducting, showing a Breit-Wigner-Fano shape if the tube is metallic [64, 65]. The D' is a (typically) small peak that can appear as a shoulder on the high frequency side of the main G peaks. In graphene this is located around 1620 cm^{-1} and is related to defects or disorder in the nanotube [66].

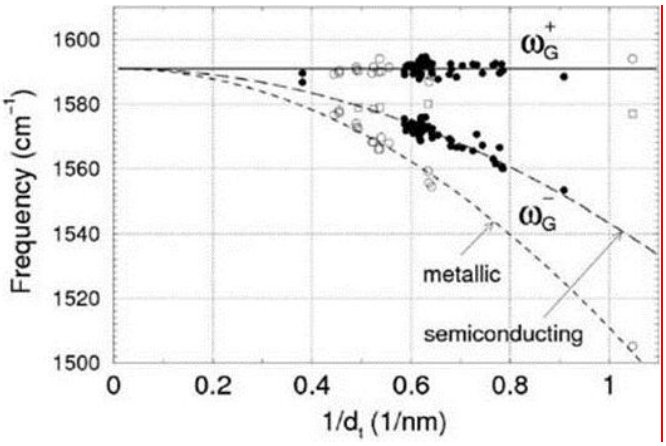

Figure 4.6. The dependence of the frequency of the G^+ and G^- peaks on diameter for semiconducting (filled circles) and metallic (open circles) nanotubes. It can be seen that the frequency of the G^+ peak is independent of the diameter, whereas the G^- peak shifts more for a metallic nanotube than for a semiconducting. The open squares are from a peak around 1580 cm^{-1} that sometimes appears in metallic nanotubes. From [63]

4.2.1.3 The D band

The D band is a second order Raman feature located around 1300-1400 cm^{-1}. The frequency of the D band depends on the laser excitation energy [67]. The origin of the D band can be understood as a double resonance (or second order) process involving a phonon and a defect [14, 68]. An electron-hole pair is created when the photon is absorbed. The electron is then scattered by a phonon (defect) with wavevector q and scattered back by a defect (phonon) with wavevector -q, see Figure 4.7. The electron then recombines with the hole and emits a photon.

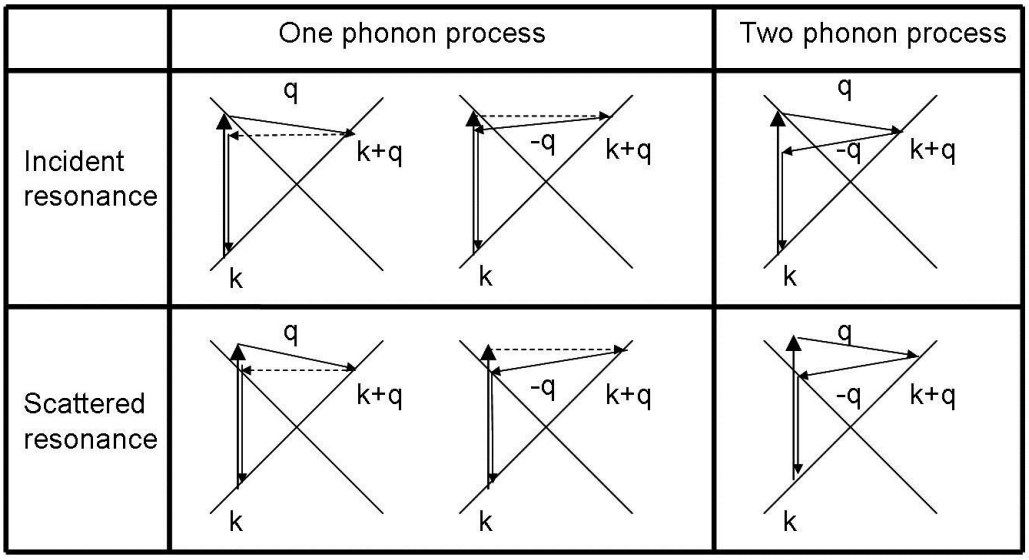

Figure 4.7. 2nd order resonance Raman processes for both one and two phonon processes. The top part shows incident resonance and the bottom shows scattered resonance. One of the scattering events in the one phonon process is an elastic transition, shown by the dotted lines. Adapted from [14, 68]

Since the nanotube has to fulfill this double resonance condition, the frequency of the D peak shifts for different tubes [67]. It has also been found that the frequency increases with increasing nanotube diameter [67]. When investigating a collection of different nanotubes, the D band therefore consists of many peaks slightly shifted in relation to each other. The D peaks are generally relatively broad and most often appear as a single peak.

Since the D peak only appears if there are defects in the nanotube (or if there is amorphous carbon present) it is a measure of the quality of the material. The area of the D peak is normalised to the area of the G peak in order to get a measure of the quality. A very

small D peak compared to the G peak indicates defect free nanotubes, whereas if the peaks are comparable in size, the tubes are more defective and/or amorphous carbon is present. The relative intensity also depends on the excitation wavelength, which makes comparisons between measurements with different lasers more difficult.

4.2.1.4 The G' band

The G' band is an overtone of the D band and is located in the region 2600-2800 cm^{-1}. The position depends, for example, on the laser wavelength, the nanotube diameter and on dopants [69]. Whereas the D band originates from a double resonance process involving a phonon and a defect, the G' band originates from a double resonance process involving two phonons with opposite momentum. For thin graphite samples, it has also been found that the position and shape of the G' peak depend on the number of graphene layers [70]. A single peak appears for a single graphene layer, whereas four peaks appear for multiple layers with an intensity that depends on the number of layers. The G' peak can therefore be used to identify the number of graphene layers.

4.2.2 Our instrument

A Renishaw In-Via Reflex micro-Raman system is used for Raman spectroscopy. The system is equipped with 5 available laser lines; 488, 514, 568, 647 and 785 nm. The 488 and 514 nm wavelengths are produced by a Modu-Laser argon ion gas laser, the 568 and 647 nm lasers are from a Melles-Griot argon/krypton mixed gas laser, whereas the 785 nm line is generated by a Renishaw near-IR diode laser. An objective with 50x magnification, numerical aperture of 0.45 and a working distance of 15 mm is used.

Chapter 5 MWCNT growth studies

The rapid growth of carbon nanotubes using acetylene as carbon feedstock in the local heating technique is investigated in this chapter. The growth procedure explained in chapter 3.2 was used with acetylene as the carbon feedstock.

The nanotubes grow with a relatively high surface density and can therefore be followed *in situ* using an optical microscope. This allows accurate measurements of the start and end times of the nanotube growth. The length is more difficult to estimate *in situ* through the optical microscope due to the tendency of the nanotube bundles to move around in the gas flow and due to the resolution. The final length is therefore measured *ex situ* on tilted samples by SEM. An average growth rate can thus be estimated from these measurements.

The catalyst is a very important factor in the growth of carbon nanotubes. Different catalysts can produce quite different nanotubes, and we have focused on Fe. The support layer underneath the actual catalyst is also very important. Many different layers have been investigated in the literature [71, 72]. Here we focus on using Al_2O_3 as support layer since it has a high thermal stability at nanotube growth temperatures and since it is very porous. The porosity reduces the agglomeration of the catalyst as the temperature is increased, it may also reduce the melting temperature of the catalyst [73]. However, this layer also reduces the electrical and thermal contact between the nanotubes and the metal electrode underneath. Consequently a thickness as low as possible that still yields good nanotube growth is desired. The growth results for 0, 1 and 5 nm of Al_2O_3 with 2 nm of Fe can be seen in Figure 5.1. A layer of 5 nm was found to be sufficient to yield carbon nanotube growth. Thicker layers were investigated, but were found to not improve the growth. Nothing was grown when the Al_2O_3 layer was too thick, which partly could be due to the increased thermal insulation from the heater. The nanotubes grow in strands keeping the geometry of the patterned catalyst and are entangled within each of the strands.

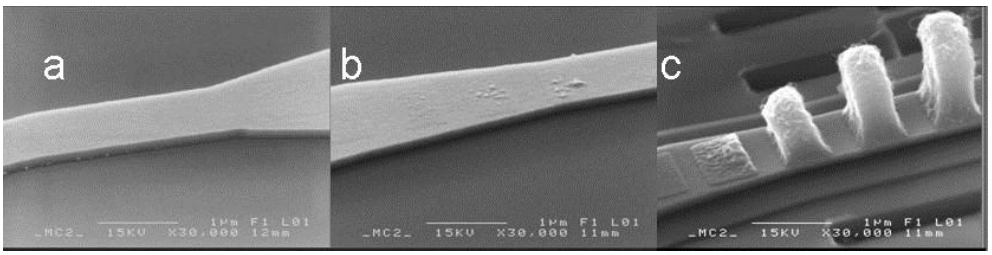

Figure 5.1. SEM images showing the effect of different thicknesses of the alumina support layer. 0, 1 and 5 nm of alumina were used in a, b, and c respectively. All other parameters are the same for all of the images, that is a catalyst layer of 2 nm Fe, an initial growth temperature of 700 °C and a growth time of 15 s.

The thickness of the deposited catalyst layer is another crucial parameter. It is even more sensitive in the local heating technique than for standard CVD techniques, where thicker Fe films have been used to grow nanotubes [74]. The growth rate is lower and significantly more amorphous carbon is deposited when 2 nm of Fe is used instead of 1 nm, see Figure 5.2. A layer of 1 nm Fe on top of 5 nm Al_2O_3 was therefore chosen for the experiments. Most of the thus synthesised nanotubes are multiwalled with only a few walls and are relatively thin, ≤ 10 nm, as found by TEM [75].

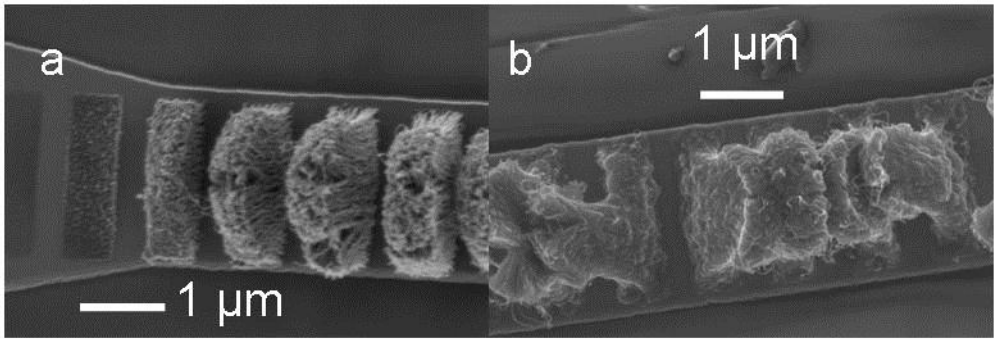

Figure 5.2. SEM images showing the effect of different thicknesses of the iron catalyst layer. 1 nm was used in a, whereas 2 nm was used in b. All other parameters were kept the same in both images.

Videos of the growth of multiwalled nanotubes grown at 600-900 °C were recorded using an optical microscope. Snapshots from one of these at 850 °C are shown in Figure 5.3. Similar videos were recorded for the other temperatures. Time is counted from when the acetylene reaches the heater. The acetylene was supplied for 1 min at each temperature, but the growth stopped by itself after a few seconds. A slight colour change can be observed immediately when the acetylene reaches the heater, which suggests a sudden change in the

temperature of the heater, as was seen in Chapter 3.2. The resistance of the heater also rapidly increases at this point, which can be seen in Figure 3.6, as discussed in Chapter 3.2.

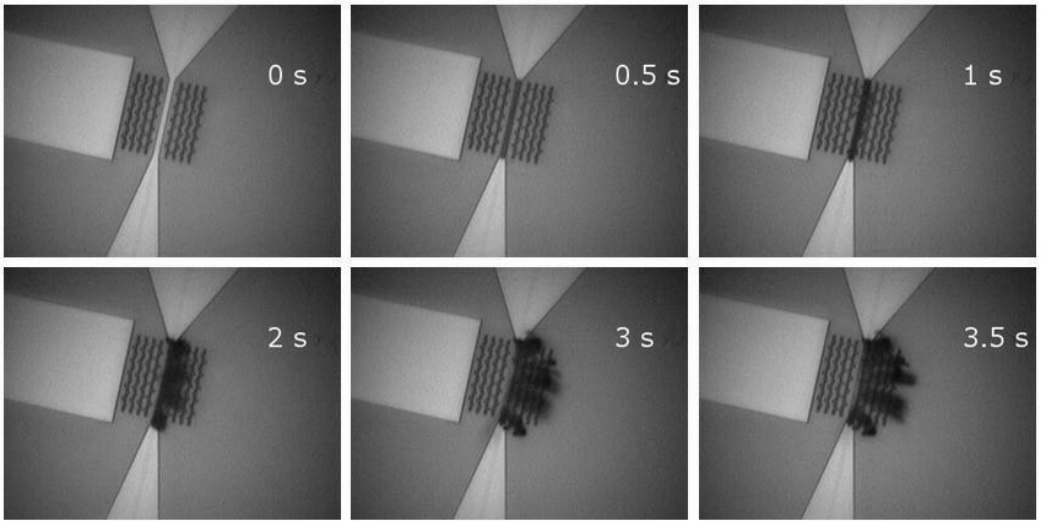

Figure 5.3. Snapshots from a video recording the growth evolution using an optical microscope. The nanotubes were grown on 5 nm Al_2O_3 and 1 nm Fe at 850 °C. The growth abruptly stopped after 3.5 s. For an indication of the sizes, the Mo heater is 30 µm long and 2 µm wide.

Carbon nanotubes can be seen to start growing already after 0.5 s. In the beginning the nanotubes grow vertically but after 2 s they all lean over to the right hand side. All the nanotubes suddenly stop growing after about 3 s. This collective start and end of the growth is found for the most efficient growth conditions at 800 °C and above. For lower temperatures the growth starts and ends slightly earlier in the hotter parts of the heater. This sudden stop of growth is due to poisoning of the catalyst. The growing nanotubes also locally cool the heater and could in some cases cool the catalyst to temperatures below the growth window. This cooling effect was discussed in Chapter 3.3. In order to more accurately estimate the length of the nanotubes, they were studied using SEM after the growth, see Figure 5.4. It can clearly be seen that there is an optimal temperature window, with less growth at higher and lower temperatures. The longest measured growth time in this series was found to be 7 s at 800 °C, but this did not result in the longest final length of nanotubes. The longest nanotubes were instead grown at 850 °C with a final length of 30 µm. Longer nanotubes were later grown in a different but similar series, see Figure 5.5. This sample was fabricated in a different batch, which results in slightly different thicknesses of the various layers, and in particular of the catalyst layer. The thickness of the layers is a

crucial parameter and small variations can lead to significant differences in the growth results.

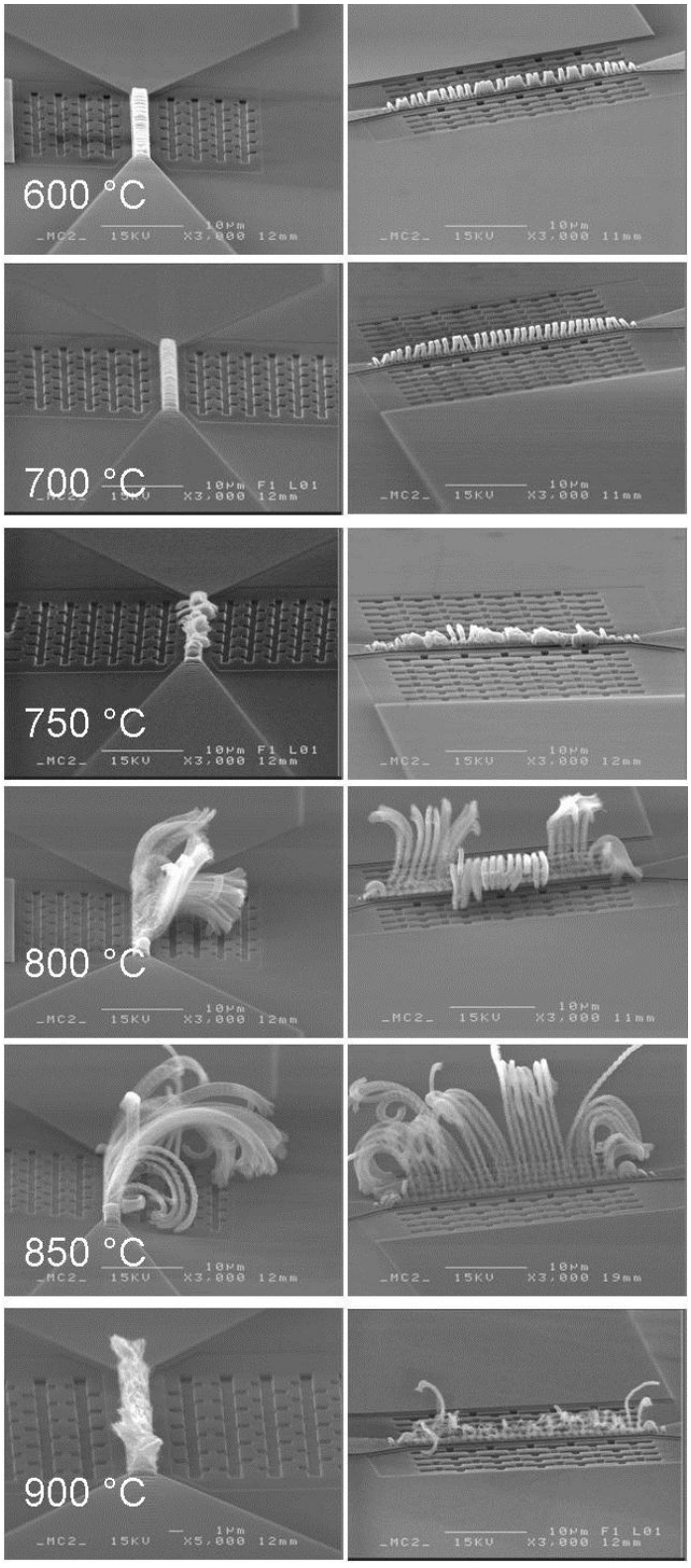

Figure 5.4. SEM images showing the effect of different growth temperatures for nanotubes grown using acetylene and a catalyst layer of 5 nm Al_2O_3 with 1 nm Fe. Images on the same row are of the same structure but at different angles.

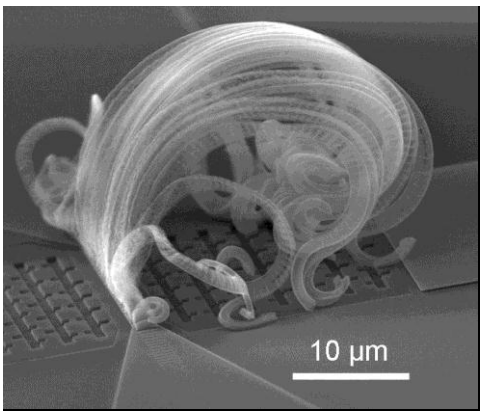

Figure 5.5. SEM image of carbon nanotubes grown at 800 °C on a sample fabricated in a different batch compared to the samples in Figure 5.4. This shows that a slight variation in thickness of the catalyst layer can result in different final lengths of the nanotubes.

The average growth rate was calculated from the growth time from the video and the terminal length from the SEM images, and is plotted together with the growth time and the final length of the nanotubes in Figure 5.6. The highest growth rate, 8.5 µm/s, was measured at 850 °C, but this growth only lasted for about 3.5 s. The lowest growth rate in this series was 0.25 µm/s at 600 °C. These are very high growth rates compared to what has been reported on conventional CVD growth of carbon nanotubes from acetylene using iron as catalyst. Puretzky *et al.* [76] investigated many different temperatures in the range 575-850 °C and found a maximal growth rate of about 0.2 µm/s. Samples fabricated in a different batch were found to yield growth rates up to about 0.7 µm/s. The difference was attributed to slightly different thicknesses of the catalyst layer due to difficulties in controlling the film thickness with Ångström precision. Significantly higher growth rates have also been recorded, but for quite different setups. Growth rates of 40 µm/s were found in ref. [77] using previously grown nanotubes as a supporting frame for the catalyst and water-assisted CVD with ethanol as carbon precursor.

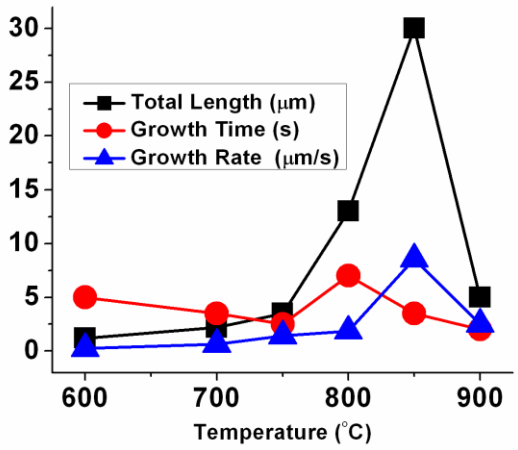

Figure 5.6. Summary of the final length, growth time and growth rate for nanotubes grown at different temperatures using acetylene growth on 1 nm Fe and 5 nm Al_2O_3.

The activation energy can be calculated from an Arrhenius plot by plotting the logarithm of the mean growth rate as a function of the inverse temperature, see Figure 5.7. By taking the temperature just before the acetylene reached the heater, a lower limit is found. This is a lower limit since the temperature increases almost 100 °C when the carbon feedstock is introduced. The growing nanotubes also cool the heater, but this effect is smaller than the temperature increase when the carbon feedstock reaches the heater, as was shown in Figure 3.9 in Chapter 3.3. The activation energy calculated this way was found to be 1.1 ± 0.2 eV (106 ± 19 KJ/mol), which is a bit lower than what has been reported for thermal CVD using Fe as catalyst and acetylene as carbon feedstock (126 ± 21 kJ/mol [78] to 159 ± 5 kJ/mol [79]). This lower value was attributed to diffusion of carbon in the iron catalyst [78], whereas the higher value was attributed to heterogeneous decomposition of the acetylene [79] precursor. By increasing the measured temperature just before the acetylene introduction by 100 °C an activation energy of 1.35 ± 0.25 eV (131 ± 24 KJ/mol) was found. Since the activation energy measured here is close to that of ref. [78], the rate determining step can be the diffusion of carbon in the iron catalyst.

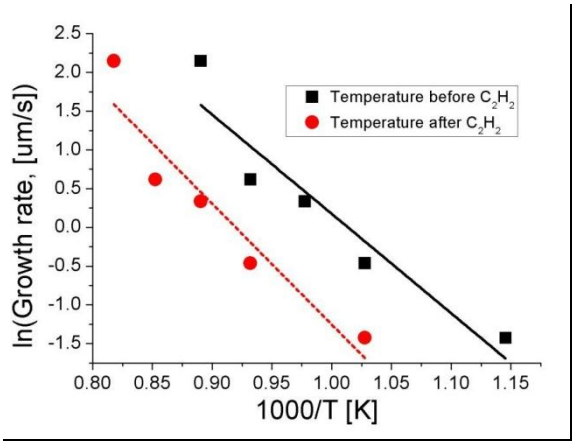

Figure 5.7. Arrhenius plot of the logarithm of the average growth rate versus the inverse of the temperature. The upper black squares are using the initial temperature just before the acetylene is introduced whereas the lower red circles are with an added 100 °C due to the temperature increase when the acetylene reaches the heater. The straight lines are linear least square fits from which the activation energy is determined.

The growth is uniform along the middle of the heater where also the temperature is uniform. In most of the images here it can be seen that the nanotubes are shorter closer to the edges of the heater. This is due to cooling from the much larger and thereby colder contacts just outside the heater itself. The metal contacts thus act as heat sinks.

There is also a temperature gradient across the short length of the heater. This can be seen in Figure 5.8 where shorter nanotubes are grown on the sides of each individual strand and longer nanotubes are grown in the middle. Due to the large contacting surface area between the growing nanotubes, strong van der Waals forces are holding back the faster growing nanotubes in the middle of the heater where it is warmer. Therefore these have to be compressed, whereas the shorter nanotubes at the edges are pulled straight. This difference in growth rate therefore create the waves in Figure 5.8.

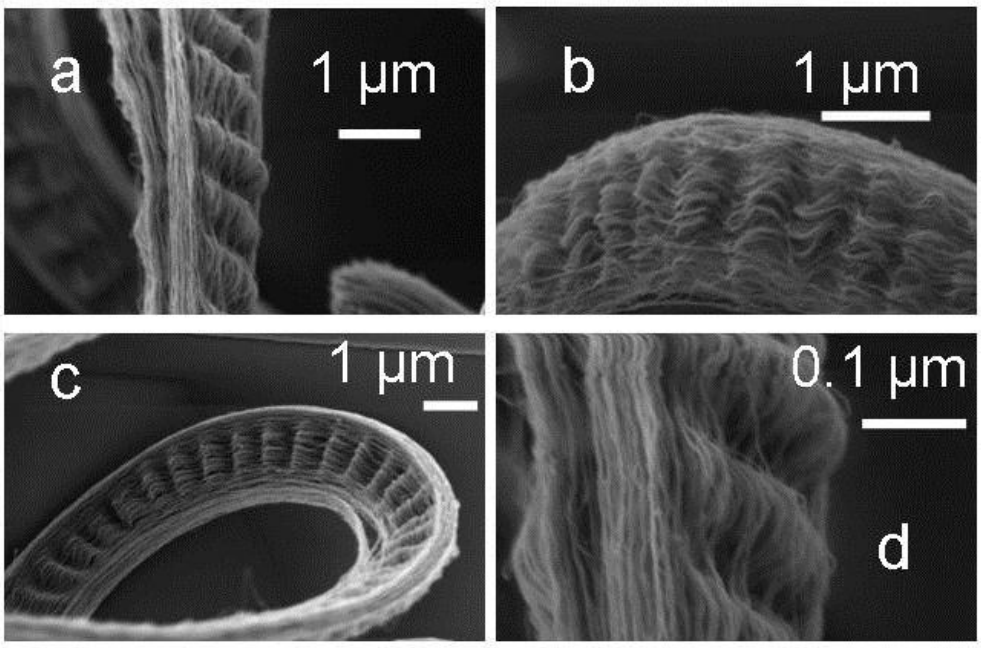

Figure 5.8. High resolution SEM images of the curled nanotubes grown at an initial temperature of 800 °C on 1 nm Fe and 5 nm Al_2O_3. This wavy structure is formed due to a temperature gradient across the heater, resulting in the inner tubes growing faster than the outer nanotubes.

These waves have a constant period for most of the growth, which gives an indication that the difference in growth rate between the inner and outer nanotubes stays constant for most of the growth. The top parts of the strands do not show this behaviour but instead appear quite uniform, see Figure 5.9. This is the parts of the nanotubes that were grown first since they are grown by a root growth mechanism. The contact area between the nanotubes is small in the beginning of the growth since the nanotubes are short. Consequently, the van der Waals forces between the nanotubes are also small, which allows the nanotubes to slide against each other instead of forming these ripples. The nanotubes at the bottom are curly but do not show this wavy structure indicating the transition to abrupt cessation of growth. It is interesting to note that the period of these waves is the same length as the wavelength of visible light.

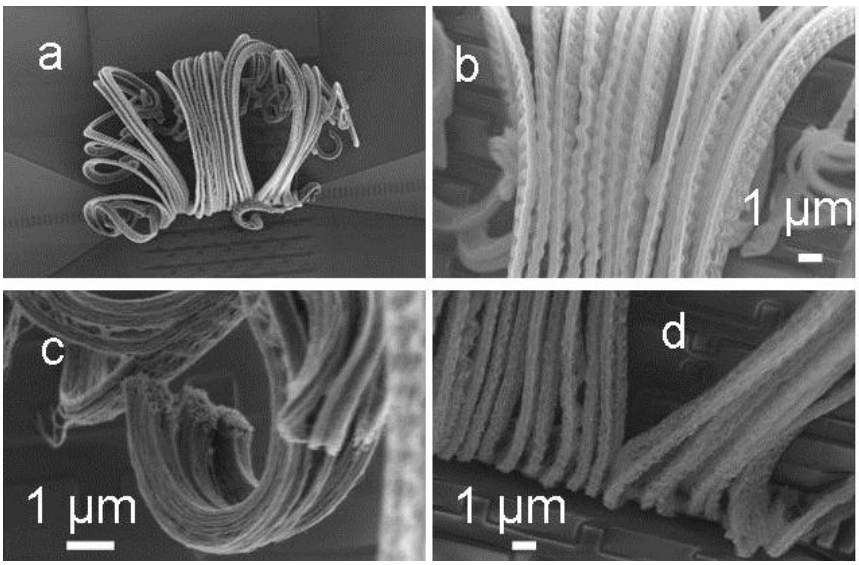

Figure 5.9. SEM images of nanotube arrays grown at 800 °C using 1 nm Fe and 5 nm Al_2O_3, showing the change in structure of the arrays during growth. a, full view, b, central region, c, tip view and d, base view.

Other groups have also observed rippled nanotube growth [80-83]. Some of these are a consequence of externally applied forces [80] whereas other are due to different growth rates of the nanotubes due to different sizes of the catalyst particles [81-83] or due to non-uniform supply of carbon [80]. In some cases the ripples are randomly located in the sample [81-83], whereas the rippled nanotubes in [80] are located at the outer edges of the forests, where the better gas supply leads to faster growth.

5.1 Temperature gradient

The temperature along these heaters is very uniform. The temperature is slightly lower close to the ends where it is connected to the larger electrodes, which work as heat sinks as already mentioned. This can be seen in Figure 5.4, where the length of the nanotubes is uniform apart from very close to the ends where shorter tubes are grown.

Using this technique only a few temperatures are sampled. In order to investigate the temperature influence with more sampling points a heater shaped as a trapezium was fabricated instead of the usual rectangular one. One end of the heater was 4 µm wide, whereas the other end was 2 or 3 µm wide. The temperature is then continuously raised across the heater since the resistance, and thereby the heating power, is continually increased along it. This way also ensures that it is only the temperature that differs as all other parameters are identical for the growth.

In Figure 5.10a it can be seen that long nanotubes are grown in the central part of the heater. On the colder side of these the length of the tubes is slowly decreased, whereas there appears to be an abrupt stop of growth at the hotter side. A similar effect was found by Engstrøm *et al.* [43]. It can also be noted that the front of the growing bundles stick together even for bundles grown at different temperatures, see Figure 5.10a and Figure 5.11. The nanotubes grow with different growth rates, but the whole group of bundles bend instead of separating and growing as individual bundles. Consequently, there are strong forces between the bundles that keep them together. A long bundle can be seen to grow to the far left where the heater meets the electrodes. The temperature is suitable for growth due to overheating from the heater side but cooling from the large contact electrodes.

The growth was also stopped after less than 10 seconds in order to see the distribution at an earlier stage and to eliminate any effects of cooling from the growing nanotubes. This resulted in a continuous change in terminal length of the nanotubes grown at different temperatures, see Figure 5.10b. Both heaters in Figure 5.10 were 4 µm wide in one end and 3 µm in the other. Blackbody spectra were measured close to both sides and in the middle of the heater. From these the temperature was estimated to be 670 °C, 700 °C and 750 °C on the cold, middle and hot side respectively.

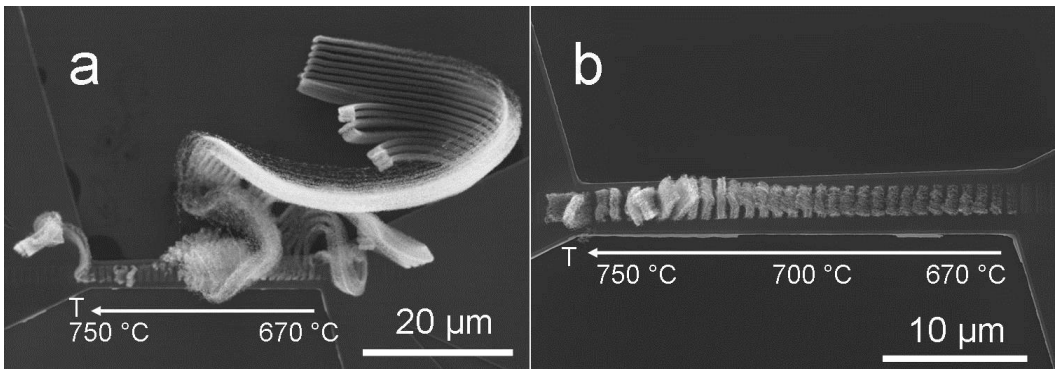

Figure 5.10. Nanotubes grown on a heater with a thermal gradient. One side of the heater is 4 µm (the right hand side) whereas the other is 3 µm wide (the left side), resulting in temperatures of 670 °C and 750 °C respectively. The nanotubes in a grew for 150 seconds whereas the growth in b, was stopped after 10 s. In a it can be seen that the nanotubes grow longer as the temperature increases until the growth suddenly is quenched when the temperature becomes too hot. The front of the arrays can be seen to grow together even though the growth rate is quite different, the different lengths of nanotubes results in bending of the group of arrays with the shorter arrays on the inside with a shorter curvature.

The nanotubes grown in the centre are not buckled as was shown in Figure 5.8 and Figure 5.9, see Figure 5.10 above and Figure 5.11 below. This is because no catalyst was deposited close to the edges of the heater, where there is a temperature gradient perpendicular to the length of the heater. The catalyst was instead only deposited in the middle of the heater to ensure that the only temperature gradient was along the length of the heater. This absence of the effect shown in Figure 5.8 and Figure 5.9 thus confirms that the ripples shown in those figures are due to the short nanotubes grown on the sides holding back the faster growing nanotubes in the centre.

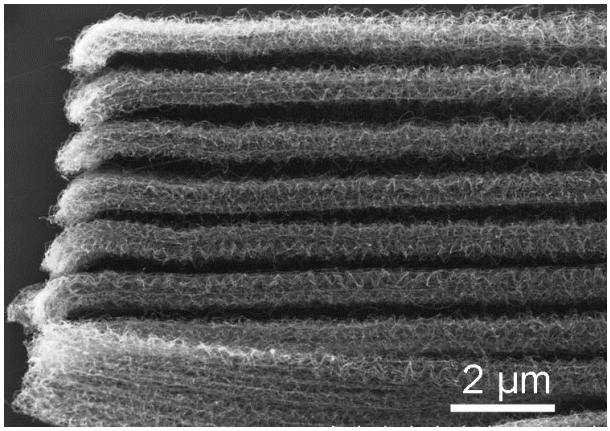

Figure 5.11. Zoomed SEM image of the top of the nanotubes in Figure 5.10a. The nanotubes have not formed ripples as in Figure 5.8 and Figure 5.9 because no catalyst was deposited on the sides of the heater where the shorter nanotubes that held back the faster ones in the middle were grown.

The temperature gradient is increased along the heaters with one end 4 µm and the other 2 µm instead of 3 µm as above. This also narrows the area where nanotubes are grown, see Figure 5.12. The temperature was here estimated to be 660 °C, 690 °C and 770 °C on the cold, middle and hot side respectively. Another interesting observation can be made in Figure 5.12c. This is the same image as Figure 5.12a but with different contrast and brightness settings. Here we see that when the temperature becomes too hot to grow the large arrays on top of the heater, individual nanotubes grow out the cooler sides of the heater.

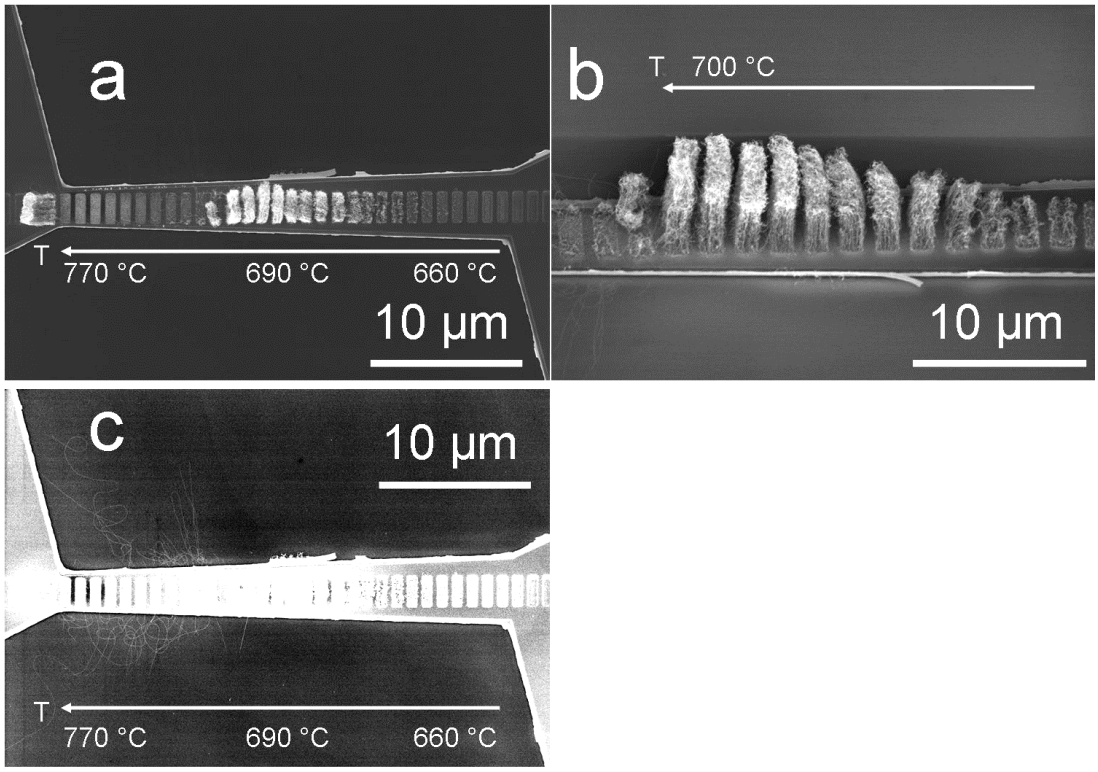

Figure 5.12. Nanotubes grown on heaters with a greater temperature gradient. One side of the heater is 4 µm wide whereas the other end is 2 µm wide, resulting in temperatures of 660 °C and 770 °C respectively. The images in a, and c, are the exact same picture but with different contrast and brightness settings in order to see the individual nanotubes growing perpendicular to the heater at high temperatures in c. b, is a tilted and zoomed image of the central region showing that the length of the nanotube arrays continuously increases as the temperature increases until the arrays stop growing and the individual nanotubes start growing.

Raman spectra were recorded along the heater in order to investigate the temperature dependence. Figure 5.13 shows the Raman spectra in the D-G region, where the spectra are normalised to the height of the G peak. It can be seen that the peaks are broader and the relative size of the D peak is significantly larger at lower temperatures.

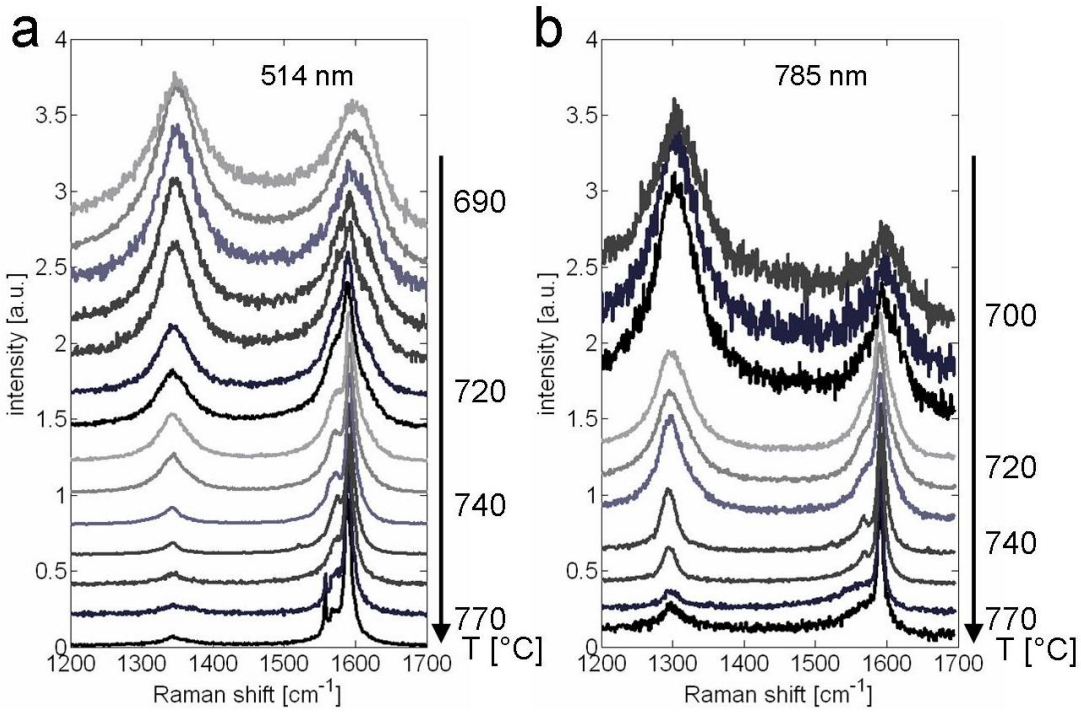

Figure 5.13. Raman spectra in the D-G region along the heater shown in Figure 5.12. The spectra in a, were obtained using a laser excitation wavelength of 514 nm whereas the spectra in b, were obtained with a 785 nm laser. All spectra have been normalised to the height of the G peak. It can be seen that the size of the D peak and the width of the G peak decrease as the temperature is increased. The spectra were obtained using a laser power density of approximately 0.1 mW/μm^2.

Figure 5.14a shows the G/D ratio at different positions along the heater. It can be seen that the G/D ratio increases as the temperature increases. The nanotubes grown at lower temperatures are therefore more defective. It can be seen that there is a sudden decrease in G/D ratio at about 8 μm from the left, which is at a higher temperature. This is where the individual nanotubes stop growing and the arrays of nanotubes start to appear on the colder side. The increase in G/D ratio can also be due to different amounts of amorphous carbon present at the different temperatures. Hydrogen becomes more reactive at higher temperatures and therefore removes more of the amorphous carbon, consequently yielding a higher G/D ratio, at higher temperatures.

The D' peak is located around 1610 cm^{-1} and is related to defects in the nanotube, just as the D peak. Figure 5.14b shows the ratio of the whole G band to the D' peak. It can be seen that the D' peak increases as the temperature decreases, compare with Figure 5.13.

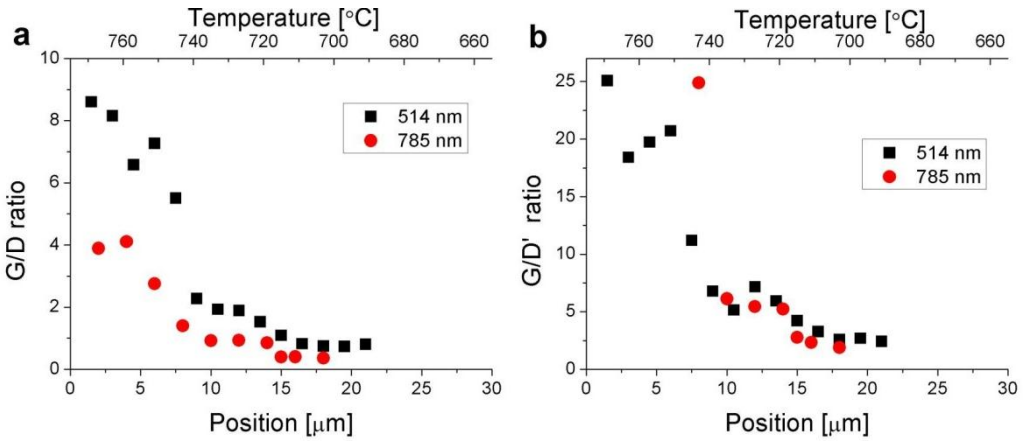

Figure 5.14. G/D ratio in a, and G/D' ratio in b, along the heater with a gradually varying temperature shown in Figure 5.12, calculated from the areas of the D and G peaks in the Raman of Figure 5.13. The sudden drop in G/D ratio after about 8 µm is where the arrays of nanotubes start growing and the individual nanotubes cease to grow. There is no D' peak to the left of the heater where the individual nanotubes are grown. The relative size of the D' peak compared to the whole G peak increases for the arrays of nanotubes grown at lower temperatures.

The individual nanotubes that grow at high temperatures yield a strong RBM signal in the Raman spectrum, see Figure 5.15. Consequently, these nanotubes are SWCNTs with a diameter of approximately 1.1-1.6 nm. More peaks appear in the spectra when going from the bottom up, that is from a higher temperature towards a lower temperature. This could both be due to more nanotubes being grown and that more of the nanotubes are resonant with the 514 nm excitation laser that was used. When the individual nanotubes stop growing and the bundles appear the RBM peaks disappear, indicating that these are MWCNTs.

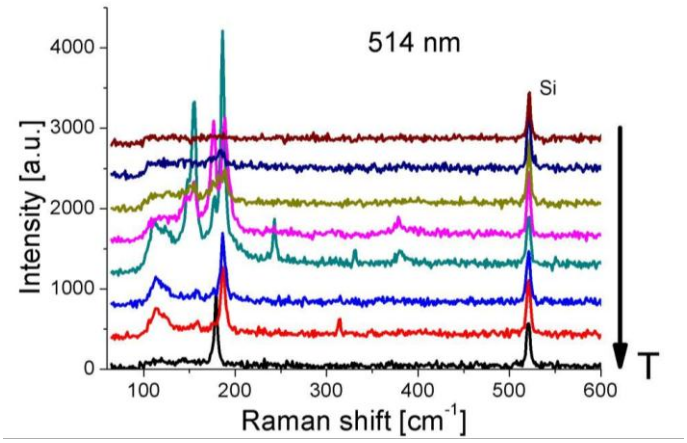

Figure 5.15. RBM spectra along the heater with a gradually varying temperature, shown in Figure 5.12. More peaks appear as the temperature is decreased, going from the bottom up in the graph. The top three curves are measured to the right where there are bundles in Figure 5.12, whereas the five lower curves are measured to the left where the individual nanotubes grow. The top three curves show fewer and weaker RBM peaks, indicating that the individual nanotubes are SWCNTs and the arrays are MWCNTs.

As a summary, the temperature dependence can be divided into different regions. At low temperatures no nanotubes are grown. When the temperature is increased MWCNTs start growing. These grow longer for higher temperatures until they abruptly stop growing when the temperature is too high. At this temperature SWCNTs start growing, which grow with a significantly higher growth rate than the MWCNTs, see Figure 5.12. A change from MWCNT to SWCNT growth at high temperatures (900 °C) was reported for conventional CVD in ref. [84]. Jungen *et al.* used a local heating technique and also found that SWCNTs grow at high temperatures whereas MWCNTs or bundles of SWCNTs grow at lower temperatures [34]. In ref. [85] it was shown that the growth can be switched from SWCNT to MWCNT growth by an increase in acetylene flow rate from 1 to 10 sccm. A model was developed in ref. [86] that predicts that SWCNTs are the fastest growing nanotubes at any given temperature and that an oversupply of carbon at this temperature will result in growth of MWCNTs and not in an increase in growth rate of the SWCNTs. This therefore predicted that the growth could be changed from SWCNTs to MWCNTs either by increasing the flow rate of the carbon feedstock or by decreasing the temperature, just as was seen here.

The melting temperature of the iron nanoparticles decreases as their size decreases and with an increase in carbon concentration [87, 88]. The nanoparticles are expected to have

approximately the same diameter as the nanotubes that grow from them [89]. The SWCNTs here have a diameter in the range 1.1-1.6 nm and the nanoparticles can be estimated to have a similar diameter. The melting temperature of nanoparticles of this size can be estimated to be approximately at the temperatures where the nanotubes above are grown [88]. The abrupt change from MWCNTs to SWCNTs could therefore be due to a change from a solid to a molten catalyst particle. The carbon diffusivity through the molten catalyst is significantly higher than through the solid [76], which also could explain the faster growth rate of the SWCNTs compared to the MWCNTs.

By comparing for example Figure 5.4 with Figure 5.10 or Figure 5.12, it appears that the temperature window for nanotube growth is significantly narrower for heaters with a temperature gradient than for the rectangular heaters. This could partly be because the samples were fabricated in different batches, which will be discussed further down. Another reason could be because these different growth series were performed in different laboratories. All the equipment was the same, but the gas bottles were stored indoors when these first experiments were done, whereas they were kept outside at approximately 10 °C for the later experiments. Different gas bottles produced in different countries were used, all at industrial purity, but it has been shown that impurity levels on the order of 1 ppm can be important [90]. In ref. [90], it was found that additional purification of industrial grade gases can significantly decrease the growth lifetime and the final height of the nanotubes. Consequently, small impurities can significantly change the growth conditions and results.

5.2 Laser-assisted growth

It has been found that lasers can be used to reach the temperatures required for nanotube growth [26, 91-94]. The growth can be very localised using this technique since the nanotube growth is limited to where the laser is aimed. Nanotubes can be grown using lasers with a broad range of wavelengths. In [93] a wavelength of 532 nm was used whereas both near- and far-infrared lasers were used to grow SWCNTs in [94]. The authors of [94] speculated that due to the sharp van Hove singularities, different nanotubes could be affected differently by the lasers and that nanotubes with selected chiralities therefore could be grown using lasers with different wavelengths. No such results were however presented.

In [92] it was found that there are three stages in the growth using the laser assisted method. A laser with a wavelength of 800 nm, irradiance of 2.2×10^5 W/cm^2 and with a spot size of 100 µm was used in the experiments. Ethylene was used as carbon feedstock. During

the first 9 seconds the catalyst film is broken up into islands, but no nanotube growth occurs. The nanotubes instead grow during the second stage, 11-15 s after the laser is turned on. If the laser is kept on for a longer time, around 3 minutes, amorphous carbon is deposited. MWCNTs were also grown both at the beam spot and around it.

The laser can also heat the sample from the backside through a quartz substrate [93]. A laser wavelength of 532 nm and power density of 1.8 to 2.5 × 10^5 W/cm^2 was used. This produced vertically aligned carbon nanotubes with a height of 60 µm. If the laser was irradiating the sample from the front, no nanotubes were grown but instead graphitic material of poor morphological structure was deposited. Acetylene was used as the carbon feedstock since no vertically aligned nanotubes were grown when using methane or ethylene.

Si nanowires have also been grown using a similar technique [91].

Here we find that nanotubes can be grown in a similar fashion by combining the local heating method with laser-assisted growth. The heater was heated to an intermediate temperature, that is a temperature too low for any growth to occur. By then firing a focused laser at a small part of the heater, nanotubes are selectively grown where the laser spot was aimed, see Figure 5.16a, where nanotubes were grown using acetylene as carbon feedstock. The effect is not laser wavelength dependent and both an excitation wavelength of 514 nm and 785 nm were used. If the heater is at a high temperature, the addition of heat from a laser can also quench the growth by increasing the temperature to above the growth window, see Figure 5.16b, where long nanotubes are grown on the sides but only short or no nanotubes are grown in the middle where the laser was aimed.

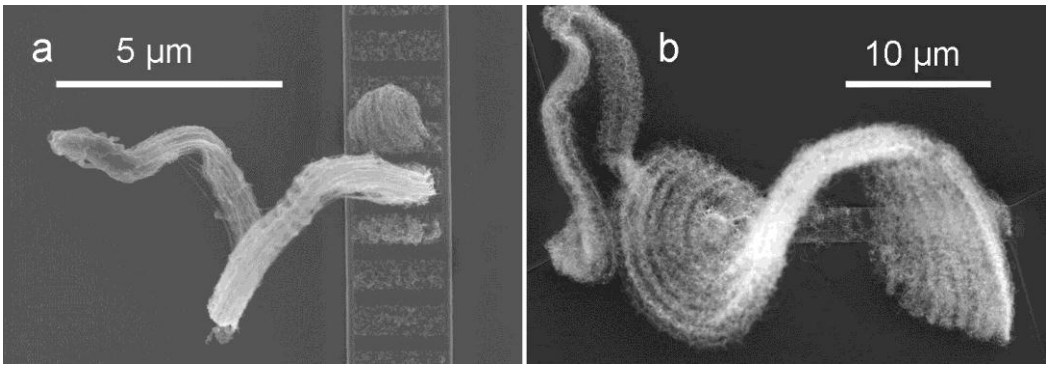

Figure 5.16. Nanotubes grown with a focused laser. a, shows an example where the laser increased the temperature into the nanotube growth window whereas b shows an example where the laser increased the temperature to above the growth window. The laser was aimed slightly to the right of the middle of the heater where it can be seen that only some short or no nanotubes are grown.

When using acetylene as carbon feedstock a significant amount of amorphous carbon is deposited on top of the nanotubes, see Figure 5.17. This is due to the laser heating the nanotubes to very high temperatures where amorphous carbon is easily deposited. In Figure 5.17a it can be seen that longer nanotubes are grown where the laser irradiated the heater. These nanotubes are also covered in amorphous carbon which the shorter non-irradiated nanotubes are not.

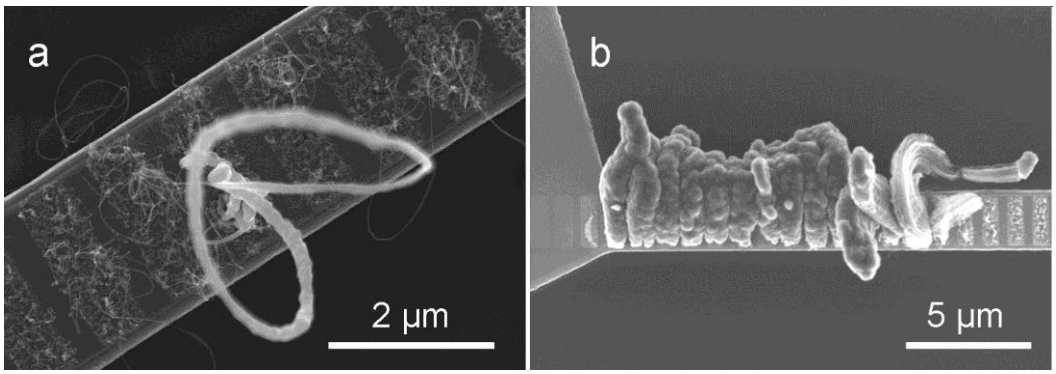

Figure 5.17. The nanotubes grown using the laser-assisted method become covered in amorphous carbon. a, shows an example with a small laser spot whereas b, shows an example where the laser was focused in a large line shape, aligned along the heater. Especially in a, it can be seen that the long nanotubes grown at the laser spot are covered in amorphous carbon whereas the shorter nanotubes on the sides are not.

5.3 Conclusions

MWCNTs were efficiently grown by the local heating technique using acetylene as carbon feedstock and an iron based catalyst. Fast growth rates of up to 8.5 µm/s were recorded. The activation energy was determined from a combination of *in situ* and *ex situ* measurements and was found to be consistent with earlier reports on the activation energy for carbon nanotube growth using conventional CVD and otherwise similar conditions.

An interesting structure, waves or ripples, of the arrays where nanotubes in the central part of the heater grow longer than the ones on the sides, show that the temperature is inhomogeneous across the heater. The evolution of this structure gives indirect information on the stability of the temperature during growth.

Nanotubes were grown on a heater with a temperature gradient such that growth where all other conditions were identical could be studied. These experiments showed that the G/D ratio increases as the temperature is increased. This shows that more defective

nanotubes are grown at lower temperatures. A sudden shift from MWCNTs to SWCNTs was also found as the temperature increased. The width of the Raman peaks and the relative height of the D' peak compared to the G peak decreased as the temperature was increased.

It was shown that the light from a laser can heat the heater from an intermediate temperature either into the growth window or to temperatures above it. This can be used to only grow nanotubes on a small part of the heater. The laser also heats the nanotubes to high temperatures such that amorphous carbon deposition becomes significant. The effect of laser heating of nanotubes will be discussed further in Chapter 7, where the influence of laser power on Raman spectra will be investigated.

Since the thickness of the different layers (catalyst, support and heater) is such a crucial parameter it can be difficult to compare samples fabricated in different batches. Even if the batches are processed with as identical methods as possible there might be slight differences in the metal layers made in different batches. This can in turn lead to different growth results when using samples from different batches. If the thickness of the Mo layer is changed, the current required to heat the heaters to nanotube growth temperatures can be significantly different for samples from different batches. This is not a major issue since the growth results do not depend on the current itself but on the temperature of the heater. After finding proper conditions this issue is therefore eliminated. However, if there is a slight difference in the thickness of the alumina or iron layers, the grown nanotubes can be quite different. Differences as small as parts of an Å might be important. Direct comparisons between different samples are therefore only made between samples fabricated in the same batch.

Chapter 6 *In situ* Raman spectroscopy studies of nanotube growth

The mechanism of carbon nanotube growth has been the subject of much speculation. The factors limiting the growth rate and final length of the nanotubes are still not known in detail. The ultimate goal of selectively synthesising nanotubes with only one predetermined chirality is also far from being reached. The best method of obtaining chirally pure nanotube samples is currently to separate the nanotubes after growth [95]. There are many factors influencing the properties of the grown nanotubes such as the temperature, composition of the gas mixture, size and material of the catalyst, pressure *etc*.. The most common method to study the effect of different parameters and to optimise the growth is first to grow the nanotubes under varying conditions and thereafter study them by electron microscopy or optical spectroscopy. The drawback of this scheme is that the effects are only studied *ex situ* after the growth. Consequently, no information is obtained on the evolution during the synthesis.

More and more research is being done on *in situ* studies of carbon nanotube growth in order to better understand the growth. The growth evolution has been studied using optical microscopy [96, 97], optical absorbance [98], laser reflectivity of the growing nanotube film [76, 99], mass spectrometry [36, 100], electron microscopy [101-103] and Raman spectroscopy [104-109]. Detailed structural information can be found by the electron microscopy investigations, but the growth conditions are typically not comparable to conditions used in conventional CVD. The optical methods can provide real-time *in situ* information but with poorer resolution. An additional advantage with *in situ* Raman spectroscopy is that it can give structural information. A drawback with *in situ* spectroscopy is the strong thermal background from the surroundings.

A few similar growth models have been formulated from these *in situ* studies [76, 108]. The carbon precursor diffuses to the surface of the catalyst particle, where it dissociatively adsorbs. This decomposition may include many steps but is normally summarised as one step described by one activation energy. The carbon atom can then follow one of two different paths [108]. One path is that it diffuses to the edge of the nanotube and integrates into the sp^2 network of the growing nanotube. This can be either through the bulk or on the surface of the catalyst. If the mobility of the atom is low or if the concentration of carbon atoms is high, they can form a disordered or defective network. This will then lead to poisoning of the catalyst and termination of the growth.

According to the model in ref. [76] the carbon atoms that reach the catalyst form a highly disordered 'molten' surface catalyst layer. The diffusion in this layer is significantly higher (almost three orders of magnitude) than the diffusion in the ordered solid phase. A similar molten layer of the catalyst to facilitate nanotube growth was proposed in ref. [87], where it was found that the melting point of 5 nm iron-carbide particles is about 10 % lower than that of the bulk material (1400 K). This is still a higher temperature than that typically used in carbon nanotube growth. The authors instead suggest that a molten layer is formed on the surface and that nanotubes start growing when this layer becomes supersaturated.

It has been found that the growth can be characterised by a self-exhausting process, such as irreversible catalyst poisoning, which can be expressed by the differential equation [98, 108, 110]:

$$\frac{d^2G}{dt^2} = -\frac{1}{\tau}\frac{dG}{dt} \qquad 6.1$$

This can be solved to give:

$$\frac{dG}{dt} = \nu \exp(\frac{-t}{\tau})$$
$$G(t) = \nu\tau(1-\exp(\frac{-t}{\tau})) \qquad 6.2$$

where ν is the initial growth rate, τ the catalyst lifetime, *t* the time and *G(t)* is the temporal evolution of the quantity of nanotubes [108] or the length of the nanotubes [98, 110]. This shows that the growth rate is maximal in the beginning and then exponentially decays. It can also be seen that the highest possible *G* can be found by the product of the initial growth rate and the catalyst lifetime.

As mentioned above, one issue with *in situ* Raman spectroscopy of growing carbon nanotubes is the strong thermal background. This thermal background is minimised in the present studies since the hot parts are limited to the small heater. There is also a drawback with the small heater; the amount of nanotubes is relatively low which leads to longer Raman acquisition times. Two different modes have been used in this chapter; the real time and "intermittent" modes. Real time refers to continuous acquisition of Raman spectra in the D-G region as the nanotubes are growing. In this mode the thermal background is strong at longer wavelengths, which limits the excitation wavelength to short wavelengths.

The "intermittent" mode uses the fact that the temperature of the heater can rapidly be varied since the thermal inertia of it is very small. A quick change in current through it

rapidly changes the temperature significantly, up to a few hundred degrees in less than a second. The growth chamber is very small (200 cm^3), which makes it possible to change the gas environment quickly. The pressure in the chamber can be reduced by two orders of magnitude in about 7 seconds. These two facts make it possible to quickly stop the nanotube growth by both decreasing the temperature and by removing the carbon feedstock. The growth can thereby be frozen in time after selected growth times. This allows longer acquisition times and thereby less noisy Raman spectra compared to real time *in situ* Raman studies. Another advantage of this technique is that the laser excitation wavelength is not limited to shorter wavelengths where the thermal radiation from the surroundings is reduced, as for real time *in situ* studies. Since the growth is stopped, spectra can be obtained both in the RBM region and in the D-G region after the same growth time.

6.1 In situ *studies using the "intermittent" mode*

6.1.1 Experimental

The growth process was slightly modified compared to the description in Chapter 3.2. The heater is heated up using the same technique, but the chamber is sealed and evacuated immediately before the carbon gas is introduced. 6 sccm of ethylene is then added to the gas flow of 300 sccm of hydrogen and 500 sccm of argon. This builds up a slight overpressure in the gas line, which allows immediate filling of the growth chamber once the valve is reopened.

The ethylene is kept on for the desired growth time, after which the chamber is evacuated in order to remove all of the carbon feedstock and the current through the heater is decreased rapidly to 10 mA corresponding to a temperature well below the growth window. The growth can be started again by increasing the temperature and by supplying a carbon feedstock. A flow of hydrogen and argon is then restarted and Raman spectra are obtained. This procedure is used because noise and blackbody radiation become strong at the high temperatures required for nanotube growth. The RBM Raman signal from the nanotubes can consequently be drowned in the background and the signal to noise ratio for the D and G peaks is significantly reduced. The intermittent technique eliminates this problem and it also allows the growth to be studied using several different excitation wavelengths. Laser wavelengths of 514 nm, 568 nm, 647 nm and 785 nm were used here and both the RBM region and the D-G region of the Raman spectrum were investigated. The laser spot was approximately 3 μm in diameter focused on the heater and the power was kept below 1

$mW/\mu m^2$. The growth was uniform along the heater, both on and off the laser spot, which shows that the additional heating from the laser did not affect the nanotube growth.

The nanotubes were grown at 800 °C, as estimated from blackbody measurements as described in Chapter 3.3.

6.1.2 Results and discussion

The growth was stopped after 5s, 15 s, 1 min, 5 min and 15 min and Raman spectra were recorded. The low wavenumber region of the Raman signal is shown in Figure 6.1, and the higher wavenumber region is shown in Figure 6.2. The evolution should be seen as a statistical average and not as the evolution of an individual nanotube since the nanotubes can move around during the growth. Corresponding SEM images are presented in Figure 6.3. Individual nanotubes can be seen to be lying perpendicular to the heater on the surface. It can be seen that SWCNTs with a small diameter start growing very quickly. In the SEM images nanotubes can be seen already after 5 s of growth, growing with a rate of at least 1 μm/s. More peaks appear in the RBM region as the growth time increases and the spectra tend to broaden. Thicker nanotubes are thus also grown, since the RBM shift is proportional to the inverse of the diameter as was discussed in chapter 4.2.1.1. In the SEM images, it can be seen that more tubes are grown as the time increases and possibly also an indication of thicker nanotubes.

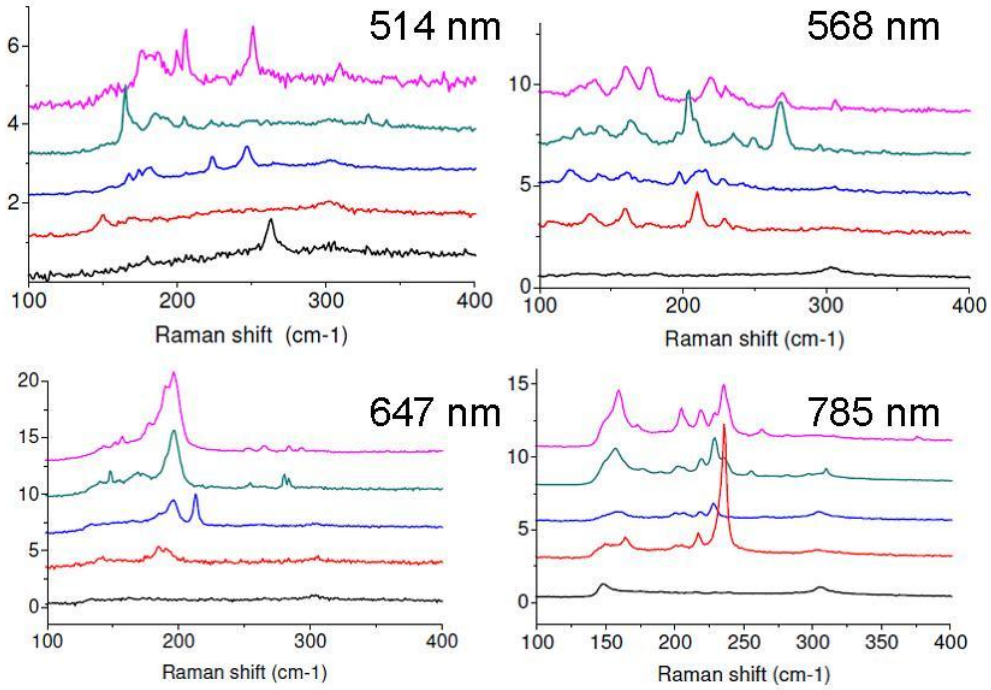

Figure 6.1. Raman spectra in the RBM region obtained from *in situ* measurements using the intermittent method. Four different wavelengths of the excitation laser were used, as shown in the images. The growth time increases from bottom up and the spectra were recorded after 5 s, 15 s, 1 min, 5 min and 10 min of growth.

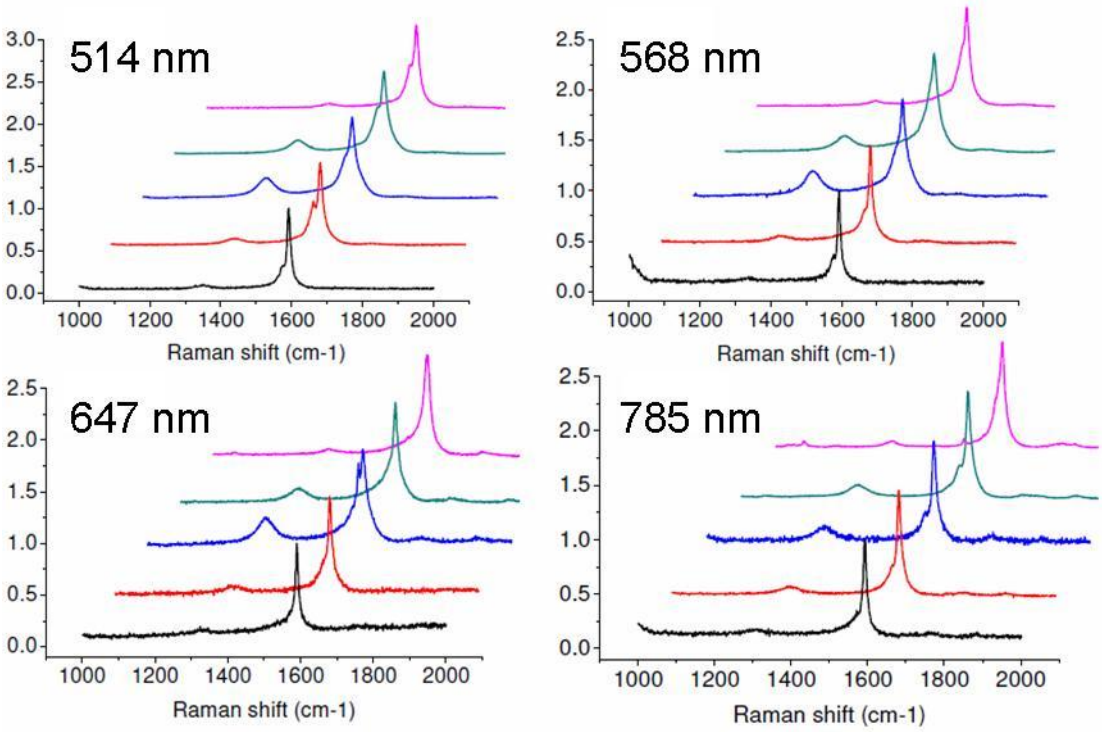

Figure 6.2. Raman spectra in the D-G region obtained from *in situ* measurements using the intermittent method. The spectra have been normalised to the G peak height. Four different wavelengths of the excitation laser were used, as shown in the images. The growth time increases from bottom up and the spectra were recorded after 5 s, 15 s, 1 min, 5 min and 10 min of growth. The spectra have been shifted horizontally for clarity.

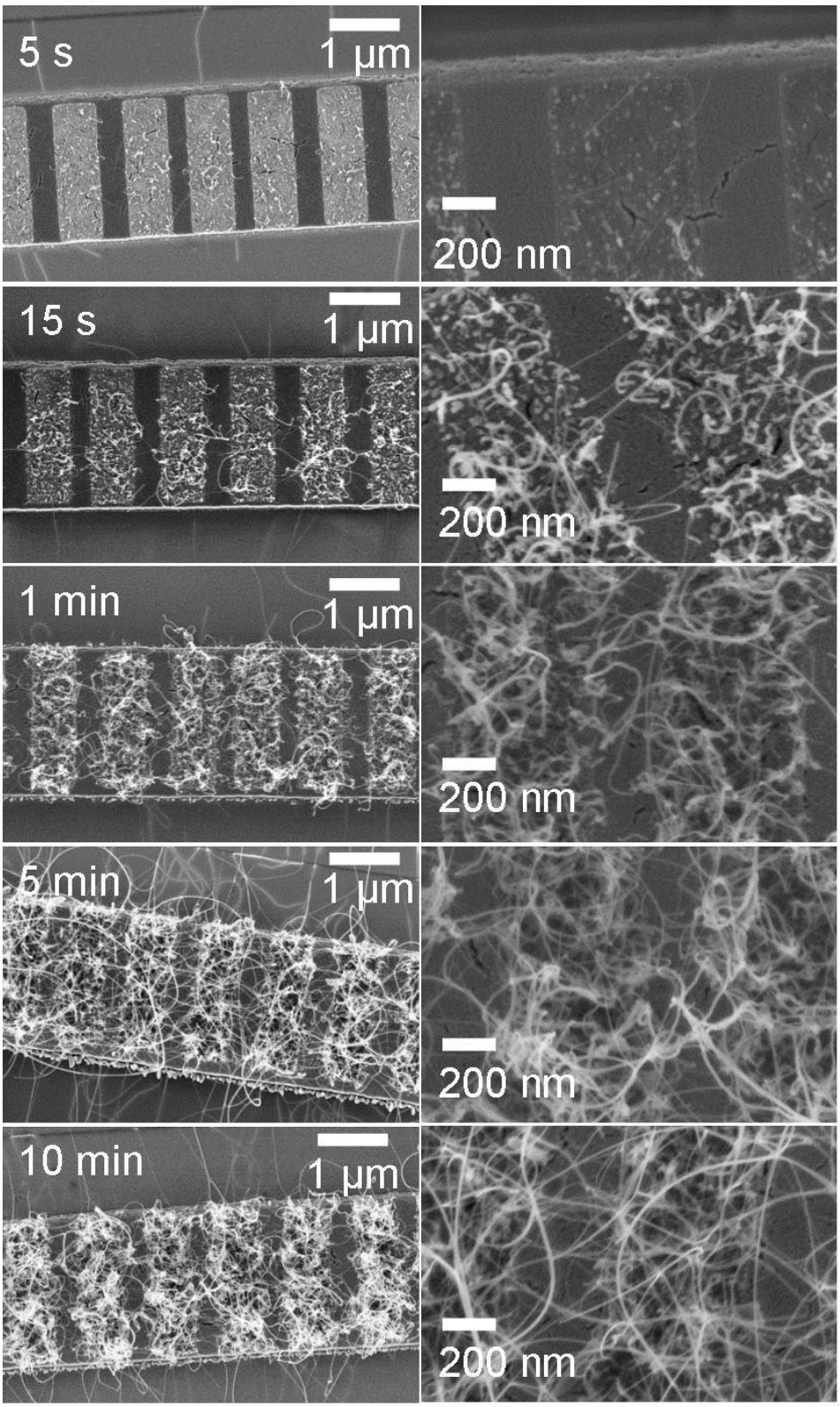

Figure 6.3. SEM images corresponding to the growth times studied using the Raman spectra, shown in Figure 6.1 and Figure 6.2. Images on the same row are after the same growth time, with the ones on the right are with higher magnification.

The high wavenumber spectra, shown in Figure 6.2, have all been normalised to the same G peak height. The width of the G^+ and G^- peaks increases slightly as the density of nanotubes increases. These peaks remain at the same position all through the growth. The D peak, on the other hand, is seen to first appear and thereafter disappear again. It reaches a maximum, compared with the G peak, after about 1 min after which it slowly decreases. The G/D ratio is plotted in Figure 6.4a, where this trend easily can be seen for all the different excitation wavelengths. This indicates the formation of a layer of amorphous carbon or may be indicating that the nanotubes grown during the first few seconds have very few defects and are followed by more defective tubes. The D peak is later seen to decrease again, suggesting that the nanotubes undergo a self-annealing process. The absolute intensities after 5 min and 10 min, using the 647 nm laser, are plotted in Figure 6.4b. It can clearly be seen that it is the absolute intensity of the D peak and not only the ratio that is decreased. This behaviour could be due to small patches of graphitic carbon being deposited in the earlier stages of the growth, which would increase the D peak. These could then grow together and form larger graphitic material, which would decrease the defects and thereby also the size of the D peak. Heat from the heater and from the laser could anneal these patches and fuse them together.

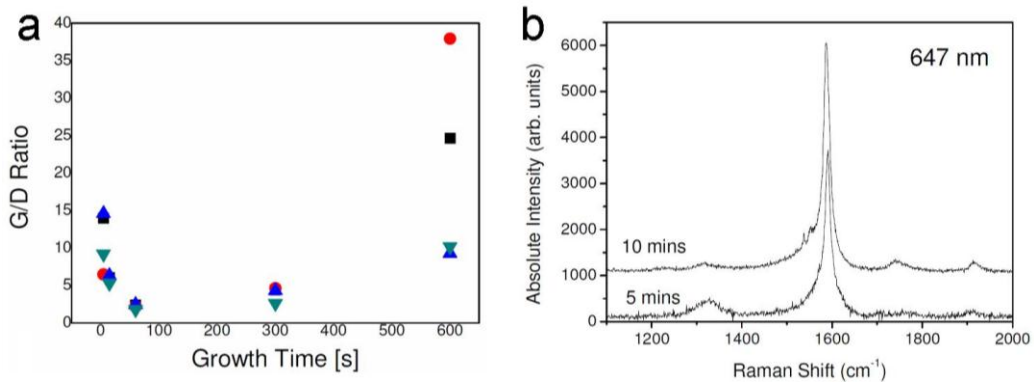

Figure 6.4. a, Plot of the G/D ratio as a function of growth time. The different symbols represent measurements using different excitation wavelengths (squares: 514 nm, circles: 568 nm, up-triangles: 647 nm, down-triangles: 785 nm). The G/D ratio first decreases and then slowly starts to increase after about 1 min. b, Raman spectra showing the absolute intensity in the D-G region after 5 and 10 min growth using the 647 nm laser. The absolute intensity of the D peak decreases as the growth times goes from 5 to 10 min.

6.2 In situ *studies using the real time mode*

6.2.1 Experimental

Carbon nanotubes were grown for 10 minutes using the technique described in Chapter 3.2. Ethylene was used as carbon feedstock since the nanotubes become covered more easily in amorphous carbon when acetylene is used. This is because acetylene decomposes more readily than ethylene. The ethylene flow rate was varied between 6 and 100 sccm (6, 12, 30, 100 sccm). The argon and hydrogen flow rates were kept at 500 and 300 sccm respectively. The current through the heater was varied between 36 and 40 mA. This resulted in temperatures from 630 °C to 670 °C according to blackbody radiation measurements.

The *in situ* Raman spectra were thus taken at high temperatures. The background from blackbody radiation can become significant at these temperatures. Since the blackbody intensity decreases for shorter wavelengths a laser with a wavelength of 514 nm was chosen for the Raman measurements. No effect of any blackbody signal was detected in the experiments.

It has been shown that the Raman signal is enhanced for suspended nanotubes [111]. In order to probe more of the nanotubes suspended from the heater down to the silica surface the laser was aimed slightly towards the edge of the heater. In order to measure a reasonable signal an acquisition time of 15 s was used. This is longer than what was used in several other *in situ* Raman studies [105, 107-109]. These studies investigated the Raman spectra from nanotubes grown using conventional CVD and consequently probed a significantly larger amount of nanotubes, which results in higher intensity. In our case, 40 spectra were recorded in order to follow the growth during 10 minutes.

6.2.2 Results and discussion

Figure 6.5 shows an example of the evolution of the Raman spectrum using 30 sccm ethylene at 640 °C. Another example where an ethylene flow of 12 sccm and a temperature of 630 °C was used is shown in Appendix B. It can be seen that the intensity of the G peak first rapidly increases in time and thereafter appears to level off or slowly increase. The sharp peaks in the spectra are from cosmic rays and have nothing to do with the nanotubes. It can also be seen that there is no signal from any D peak, indicating that the growing nanotubes do not have many defects and that no or only a small amount of amorphous carbon is deposited.

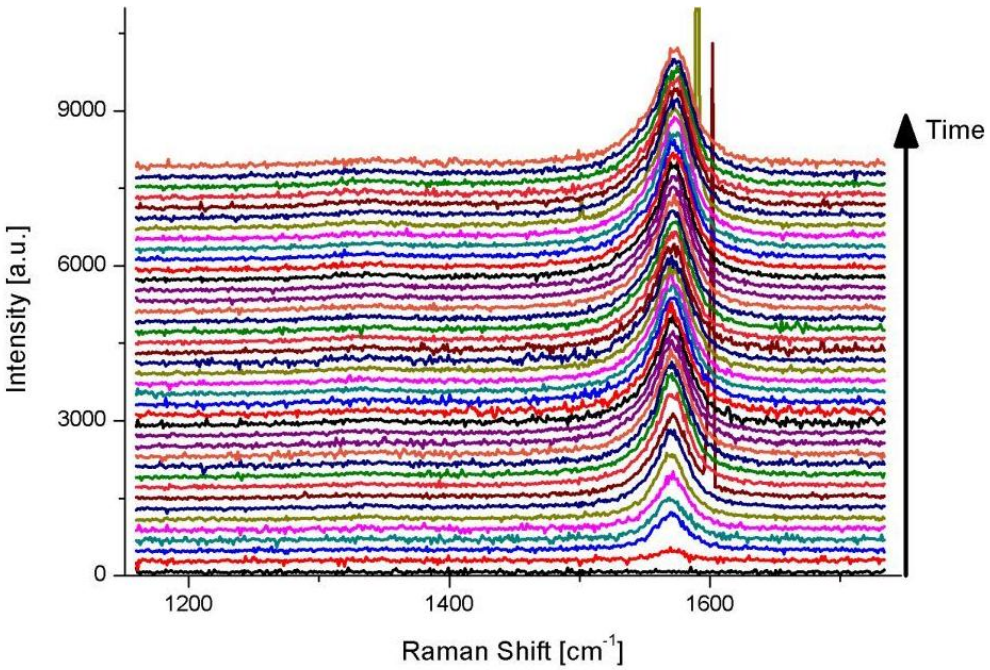

Figure 6.5. Time evolution of the Raman spectrum in the D-G region for nanotubes grown at 640 °C using an ethylene flow rate of 30 sccm. Growth proceeds from the bottom to the top and each spectrum is recorded using an acquisition time of 15 s. The two sharp peaks are cosmic rays.

The G band can consist of several peaks and was here fitted with up to four Lorentzian peaks. In general, more peaks were necessary at the highest flow rates and fewer at the lowest temperatures. Two examples of the fits are shown in Appendix B. The total area of the G band was thus calculated by summing the area of all the G peaks. This was then plotted as a function of time, see Figure 6.6, where each image shows the time evolution of the G band at different ethylene flow rates but equal temperatures. Time 0 s is defined as when the first Raman measurement was started and when the ethylene flow was turned on.

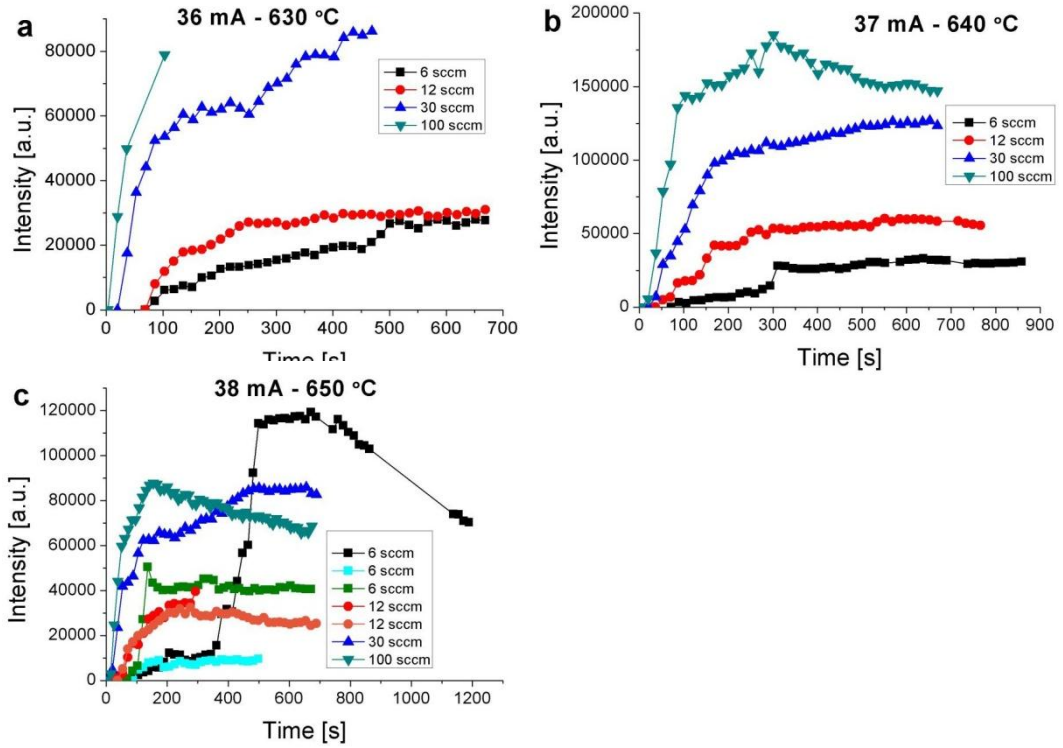

Figure 6.6. Time evolution of the area of the G band. Each image shows the evolution at a constant heater current and temperature for different ethylene flow rates. The temperature is 630 °C in a, 640 °C in b, and 650 °C in c.

The same trends as were seen in Figure 6.5 can be seen in Figure 6.6. That is, the intensity of the G band first rapidly increases and then either levels off or increases but at a significantly slower rate. It can also be seen that there is a delay between the start of the carbon flow and the time when a signal is recorded in the Raman spectrum. This delay is longer for lower flow rates. The intensity is increased at higher flow rates, which indicates that more nanotubes are grown.

The increase in intensity of the G band mirrors the nucleation of nanotubes and the early stages of the growth. After a certain time the intensity stays approximately constant, indicating that no new nanotubes are nucleated. The nanotubes can very well continue to grow outside of the laser spot.

The first rapid increase shows that most nanotubes are nucleated at the same time, after which no new nanotubes are nucleated. The increase in intensity that sometimes can be seen after the first rapid increase is instead due to deposition of amorphous carbon, as will be discussed later. In a couple of cases the intensity can be seen to start decreasing. This can be

due to a small drift of the laser spot away from the heater and thus to a location with less nanotubes. It can also be due to growing nanotubes falling out of the laser spot. Another explanation could be that the nanotubes fall down on the surface. This would result in a lower Raman signal since the Raman signal is stronger for suspended than for supported nanotubes [111]. A similar trend of a decreasing signal in time was found using laser absorbance in ref. [98]. The authors attributed this to burning of the nanotubes which occurred due to air leaking into the chamber. By varying the leak rate of air into the system, it was also found that the initial growth rate is very sensitive to the environment immediately before growth, whereas the lifetime did not change. Burning of nanotubes or amorphous carbon can not be ruled out as an explanation for the results shown here.

The opposite trend can be seen, for example, in Figure 6.6c for a temperature of 650 °C and an ethylene flow rate of 6 sccm. After approximately 350 s the intensity significantly increases due to nanotubes grown outside of the laser spot falling in to the probed area and therefore increasing the intensity of the G band. This experiment was repeated three times due to this sudden increase in G band intensity. The trend is the same until this happens. This is much more important for low flow rates and high temperatures since the amount of growing nanotubes is limited, as will be seen further down. Consequently, this can result in a significant increase even if only a few nanotubes fall into the probed area. These nanotubes will also be suspended which results in a strong Raman signal.

The growth at 650 °C with a flow rate of 12 sccm was also repeated since the heater was about to break. This could be seen since the voltage drop over the heater quickly started to increase during the growth. The experiment was therefore aborted after approximately 5 min as can be seen Figure 6.6c.

Figure 6.7 shows the same time evolutions but grouped together by different temperatures but equal flow rates. Here it can be seen that the incubation time before any growth is recorded is very similar for all temperatures as long as the gas flow is kept constant. Consequently, the incubation time depends on the ethylene flow rate and not on the temperature. This is in contrast to what was found in ref. [107], where a temperature dependence was found and characteristic energies of 1.8 ± 0.6 eV and 4.7 ± 0.8 eV were found for nanotubes grown using Co as a catalyst with and without a support layer of alumina, respectively. The authors of ref. [107] discuss that the large energy found without a support layer could be due to pyrolysis or desorption of chemisorbed carbon. The large difference between the two setups was explained as that the alumina might act as a reservoir

that has to be filled. Another discussed possibility was that surface or bulk diffusion in or on the substrate could be a rate-limiting step. The incubation time is further discussed in chapter 6.2.3.

In Figure 6.7a there appears to be an optimal temperature for nanotube nucleation at 640 °C, since the intensity of the G band is strongest at this temperature. However, at this temperature there is a change from MWCNTs that are grown at lower temperatures to SWCNTs that are grown at higher temperatures, see Figure B.2 in Appendix B and Figure 6.11 with the discussion about the RBM measurements. The Raman signal from the nanotubes grown at 630 °C is lower than that from the nanotubes grown at 640 °C. If similar nanotubes were grown at the different temperatures this would indicate that more and/or longer nanotubes are grown at 640 °C. This is not the case here since the nanotubes grown at 630 °C are MWCNTs, which yield a weaker Raman signal than the SWCNTs grown at 640 °C. When the temperature is increased further, fewer and fewer nanotubes are grown which leads to the decreased intensity of the G band.

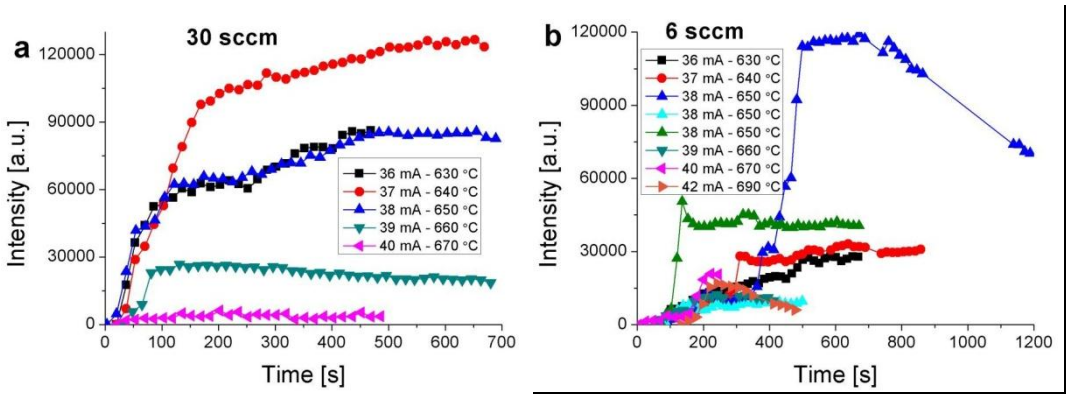

Figure 6.7. Time evolution of the area of the G band. Each image shows the evolution at a constant ethylene flow rate but for different temperatures. The flow rate is 30 sccm in a, and 6 sccm in b.

It was only at the lowest temperature, 630 °C, that the evolution of the D peak could be followed. The intensity was too low at all other temperatures. The reason that the D peak could be followed during the intermittent growth studies but not during the *in situ* investigation could be that the acquisition time is shorter here, such that the D peak might disappear in the noise. The samples were also fabricated in different batches which might influence the growth, as discussed in Chapter 5. The time evolution of the D peak for different flow rates at 630 °C is plotted in Figure 6.8a. It can be seen that the D peak follows the same trend as the G peak. For example, longer incubation times before any signal is detected for lower flow rates and a stronger intensity for higher flow rates. The G/D ratio

grows in time before it stabilises, see Figure 6.8b. The G/D ratio stabilises faster at higher flow rates.

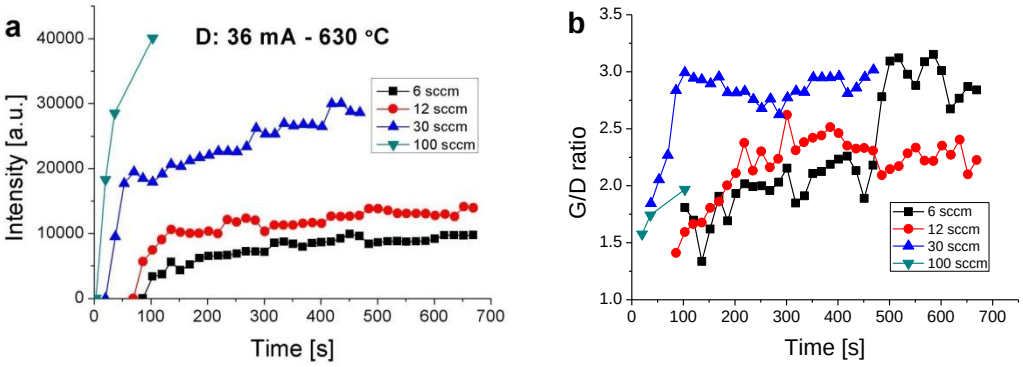

Figure 6.8. a, Time evolution of the D peak for MWCNTs grown at 630 °C for different ethylene flow rates. b, Time evolution of the G/D ratio for the same samples as in a.

Figure 6.9 shows SEM images of the nanotubes grown at 37 mA, 640 °C. SEM images for all the other investigated growth conditions can be found in Appendix B. Curly nanotubes are found to grow on top of the heater, whereas longer nanotubes grow out to the sides of the heater. It can be seen that more and more nanotubes are grown when the ethylene flow rate is increased. These trends are in agreement with the evolution of the G peak in the Raman spectrum, as was shown in Figure 6.6b.

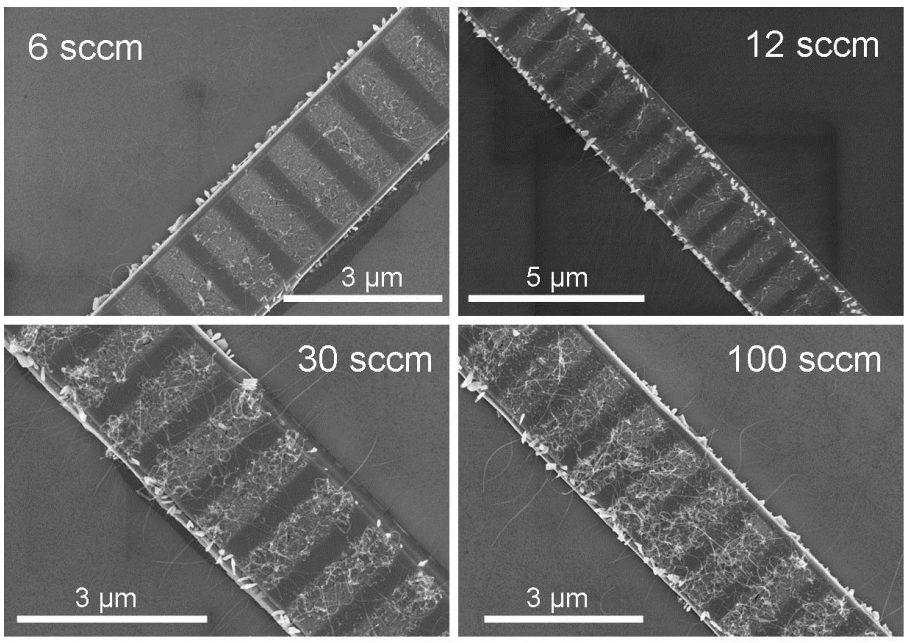

Figure 6.9. SEM images of nanotubes grown at 640 °C for different ethylene flow rates, as shown on the different images.

At low temperatures (630 °C) and high flow rates (30 and 100 sccm) many more long curly MWCNTs are grown, see Figure 6.10 and figures in Appendix B. The laser spot was aimed at the right hand side of Figure 6.10, where a significant amount of amorphous carbon was deposited. This is due to the extra heating of the nanotubes from the laser. The laser power is kept low so that the temperature is uniform across the heater. Therefore also the growth is uniform along the heater. When the carbon concentration in the atmosphere is high, the laser heats the nanotubes sufficiently for amorphous carbon to be deposited on the nanotubes.

The same indication of deposition of amorphous carbon at high ethylene flow rates can be seen in the plots of the time evolution of the G peak in the Raman spectra. The intensity of the G band levels off and remains approximately constant for low flow rates, whereas the intensity continues to increase at a low rate for higher flow rates. This is therefore attributed to deposition of amorphous carbon.

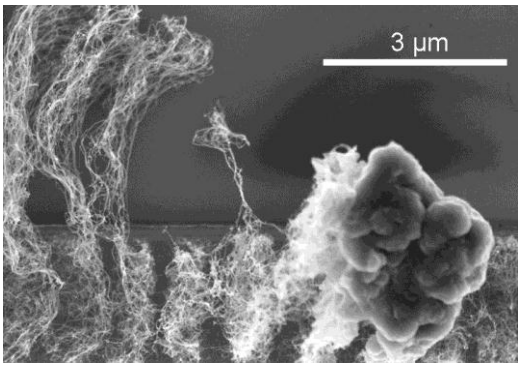

Figure 6.10. SEM image of the effect of laser irradiation of the nanotubes during growth in an ethylene atmosphere at low temperature (630 °C) and high ethylene flow rate (30 sccm). A significant amount of amorphous carbon is deposited where the laser spot was, whereas none or very little was deposited outside the laser spot.

RBM measurements were recorded at room temperature after the growth had finished. The laser was aimed in the same spot as where the Raman signals had been recorded during growth. The spectra of nanotubes grown at higher temperatures show strong RBM peaks mainly in the region 150-200 cm^{-1}, see Figure 6.11, which corresponds to SWCNTs with diameters approximately in the range 1.1-1.5 nm. At low temperatures and high carbon flow rates, no RBM peaks are found. This could either be due to the nanotubes being MWCNTs or that they are not resonant with the 514 nm excitation wavelength that was used. In order to check this, more spots along the heater were measured with laser excitation wavelengths of both 514 nm and 785 nm, but no RBM signals were found. This indicates that the

nanotubes grown at low temperatures and high flow rates are MWCNTs, whereas the other nanotubes in the measurement series are SWCNTs. This agrees with the effects discussed above where many more long curly nanotubes are grown at these conditions. It also agrees with the decreased G band signal measured for these nanotubes, as was seen in Figure 6.7a. This is the same effect as was discussed in Chapter 5.1. It was also predicted by the model in ref. [86] that the growth can be changed from SWCNTs to MWCNTs by decreasing the temperature or increasing the flow rate of the carbon feedstock. In ref. [85] it was shown that the growth can be switched from SWCNTs to MWCNTs by increasing the acetylene flow rate from 1 to 10 sccm.

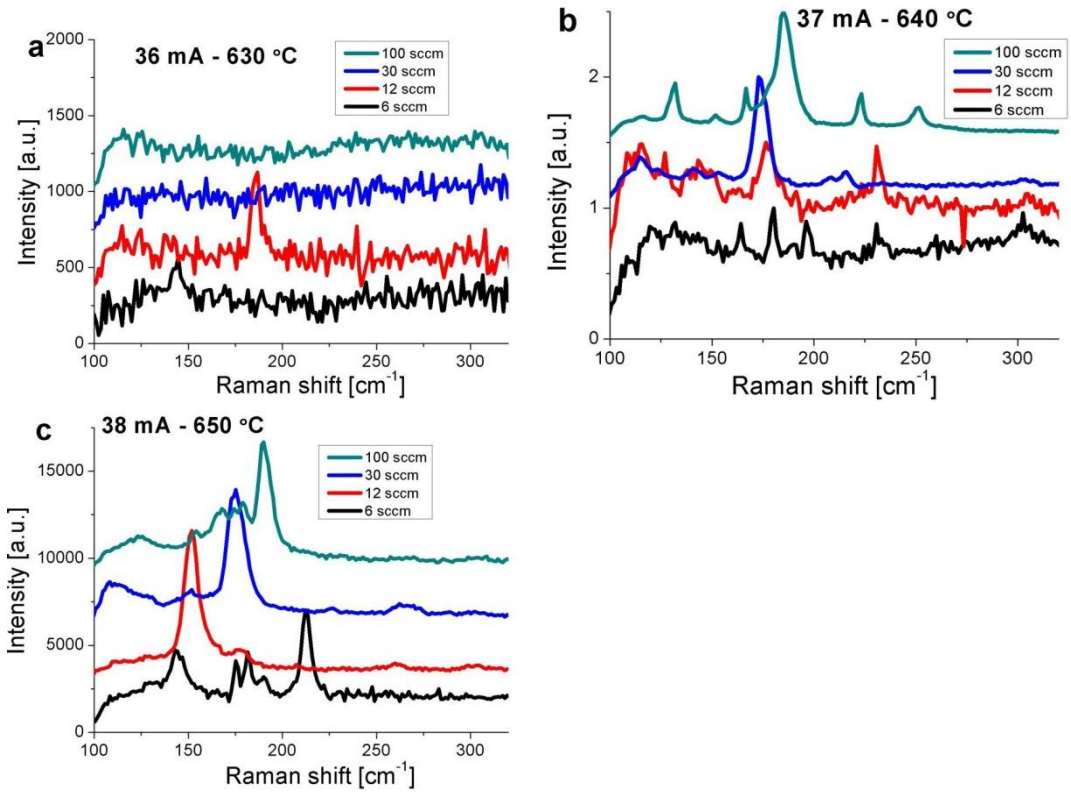

Figure 6.11. RBM measurements of the nanotubes that were followed using *in situ* Raman measurements in the D-G region. a, b, and c show measurements of nanotubes grown using different gas flows and at 630 °C, 640 °C and 650 °C, respectively. The spectra were recorded at room temperature after growth using a laser excitation wavelength of 514 nm.

A heater patterned as a trapezoid and thus forming a temperature gradient along it was used under similar growth conditions, see Figure 6.12a and b. The temperature was estimated to be 660 °C, 690 °C and 770 °C on the cold, middle and hot side respectively and

the growth time was 5 min. Similarly to what was found for the same samples used for nanotube growth with acetylene as carbon feedstock, it can be seen that vertically aligned arrays of nanotubes grow on the colder end of the heater, whereas long individual nanotubes grow on the hotter end. Figure 6.12c shows a heater with a different temperature gradient, where the temperature was 670 °C at the colder wider end and 750 °C at the hotter narrower end. These nanotubes were grown during 90 s. It can be seen that relatively long individual nanotubes have been grown but the nanotubes where the arrays are expected to appear are still relatively short. Consequently, the nanotubes grown using ethylene grow significantly slower than the nanotubes grown using acetylene as carbon feedstock. Acetylene is more reactive than ethylene because of its triple bond compared to the double bond in ethylene. Acetylene has been found to be orders of magnitude more efficient for nanotube growth than other small carbon containing molecules [37].

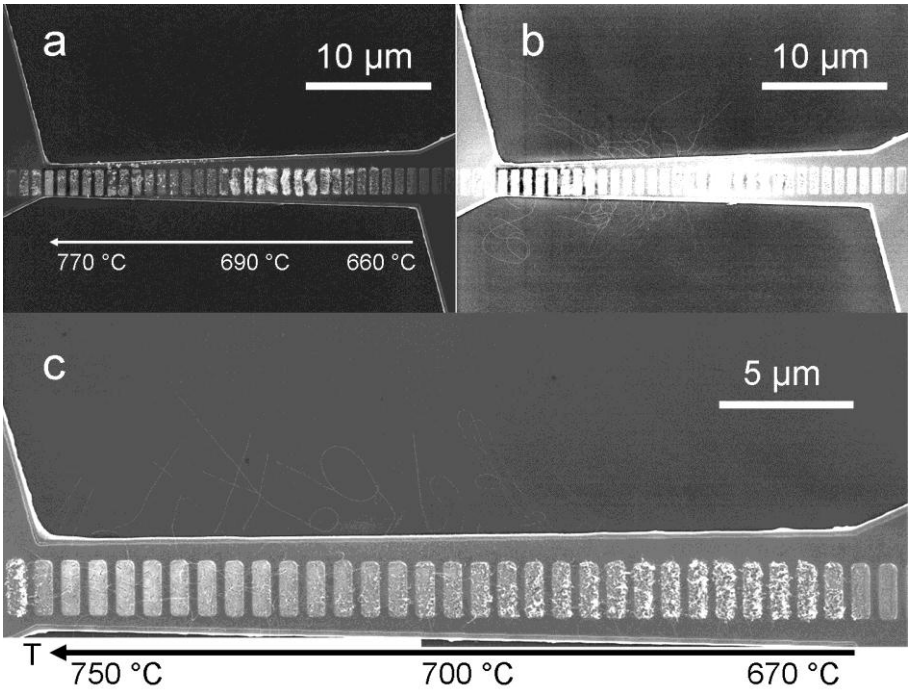

Figure 6.12. a and b, Nanotubes grown on a heater with a temperature gradient. One side of the heater is 4 µm wide whereas the other end is 2 µm wide, resulting in temperatures of 660 °C and 770 °C respectively. The images in a, and b, are the exact some picture but with different contrast and brightness settings in order to see the individual nanotubes growing perpendicular to the heater at high temperatures in b. The nanotubes in a, and b, were grown for 5 min. c, nanotubes grown on a heater with one end 4 µm wide and the other end 3 µm wide, resulting in

temperatures of 670 °C and 750 °C respectively. The nanotubes in c, were grown during 90 s.

Raman spectra were recorded after the growth along the heater. These are shown in Figure 6.13, where the spectra are normalised to the height of the G peak. It can be seen that the width of the peaks and the relative size of the D peak increases for lower temperatures, as observed for acetylene growth, see Figure 5.13 in chapter 5.1.

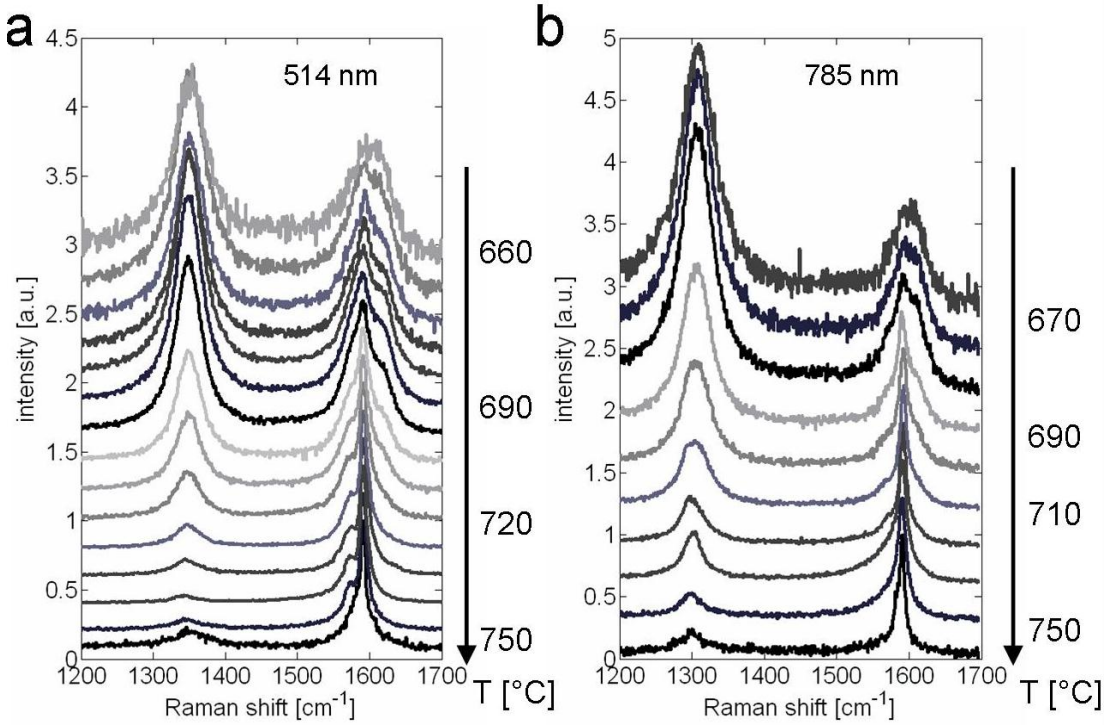

Figure 6.13. Raman spectra in the D-G region along the heater shown in Figure 6.12. The spectra in a, were obtained using a laser excitation wavelength of 514 nm whereas the spectra in b, were obtained with a 785 nm laser. All spectra have been normalised to the height of the G peak. It can be seen that the size of the D peak and the width of the G peak decreases as the temperature is increased. The spectra were obtained using a laser power density of approximately 0.1 mW/μm^2.

Figure 6.14a shows the G/D ratio at a number of positions along the heater shown in Figure 6.12a and b. The G/D ratio increases as the temperature is increased. The ratio is reduced at high temperatures where the temperature was too hot for efficient nanotube growth and amorphous carbon was slowly deposited, compare with the SEM images in Figure 6.12a and b. It can be seen that the G/D ratio is significantly higher on the left hand side of the heater where the individual nanotubes are grown. The relative size of the D' peak compared to the G band increases for lower temperatures and appears where the nanotube

arrays start growing, see Figure 6.14b. All of these trends are very similar to the nanotube growth with acetylene as carbon feedstock, see Figure 5.14 in Chapter 5.1. The main difference is the decrease of the G/D ratio of the nanotubes grown from ethylene at high temperatures. This difference is because the acetylene growth took place over 10 s whereas the growth time using ethylene was 5 min. Significantly more amorphous carbon was deposited at these higher temperatures during the significantly longer growth time with the ethylene precursor.

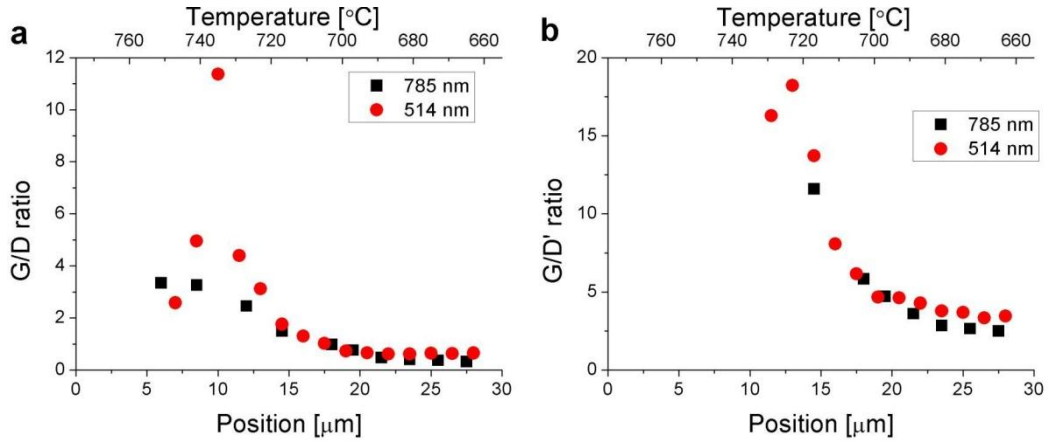

Figure 6.14. G/D ratio in a, and G/D' ratio in b, along the heater with a gradually varying temperature shown in Figure 6.12a and b, calculated from the areas of the D and G peaks in the Raman spectra of Figure 6.15. The G/D ratio increases for higher temperatures until a spot with no or little CNT growth but with amorphous carbon deposition appears. The D' peak appear for the arrays of nanotubes and is not measurable for the individual nanotubes. The D' peak continuous to grow as the temperature is decreased.

6.2.3 Heater characterisation

At the same time as the LabVIEW program controls the current through the heater it also monitors the voltage drop across it as measured in the four point setup. Figure 6.16 shows this voltage drop versus time for different temperatures at an ethylene flow of 30 sccm. The general behaviour was discussed in Chapter 3.2. Here we focus on the behaviour just after the ethylene flow is started, which is defined as time 0 s. The Raman spectra are also started at this time.

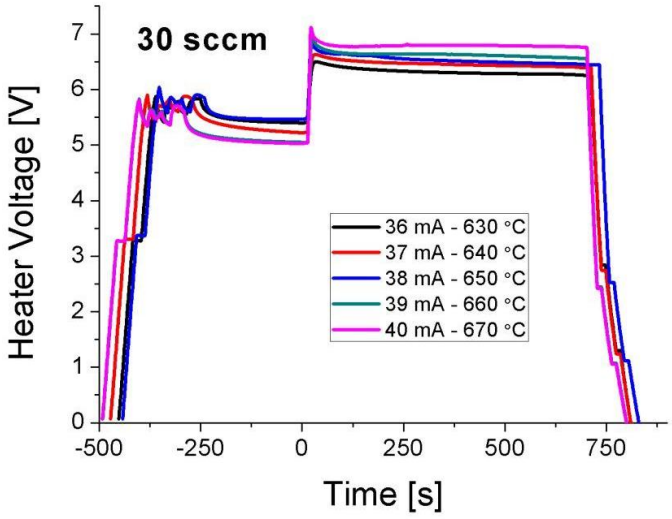

Figure 6.16. Voltage across the heater, as measured using a four-point setup, versus time. Time 0 s is set when the Raman measurements and the ethylene flow were started. The different curves are at different temperatures and all are at an ethylene flow rate of 30 sccm.

The first 150 s after the ethylene flow is started is shown in Figure 6.17. Figure 6.17a shows that there is an incubation time before the voltage is rapidly increased. This incubation time is longer for lower ethylene flow rates, as can be seen in Figure 6.17a where the voltage drop is plotted for different ethylene flow rates at 630 °C. This incubation time does not depend on the temperature, see Figure 6.17b where the voltage drop across the heater is plotted versus time for different temperatures at an ethylene flow rate of 6 sccm. The logarithm of the incubation time versus the logarithm of the partial pressure of ethylene is shown in Figure 6.18. The time it takes for the gas to travel through the feed line and reach the heater has here been removed. It can clearly be seen that the incubation time depends on the partial ethylene pressure but not on the temperature, just as was seen for the Raman measurements.

The increase in voltage that follows the incubation time is due to molybdenum carbide formation on the heater. Ethylene absorption on a clean Mo(100) surface was investigated in ref. [112], where it was found that a significant amount of carbides are formed above 400 °C. This increases the resistance and thereby the voltage drop at a constant current. The rate of this voltage increase, and thereby also this carbonisation, increases for higher ethylene flow rates, see Figure 6.17a, and for higher temperatures, see Figure 6.17b. Similarly, it takes a longer time for the heater to saturate for lower flow rates, see Figure 6.17a, and lower temperatures, see Figure 6.17b.

Similar figures but at different temperatures and ethylene flow rates are shown in Appendix B.

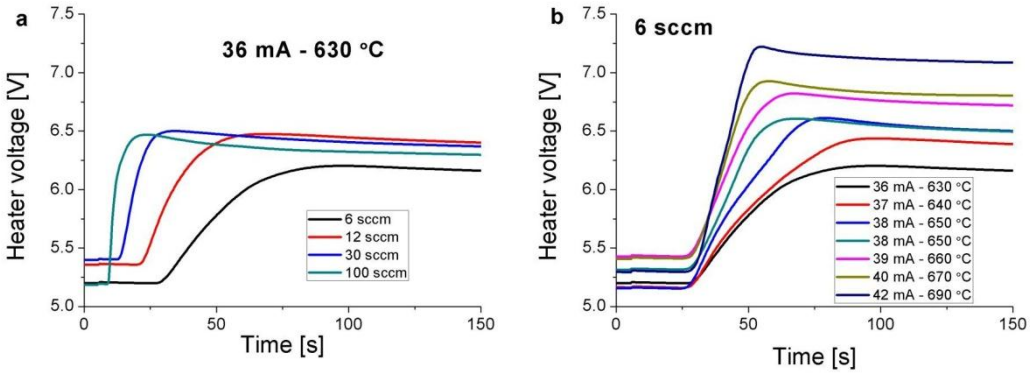

Figure 6.17. Zoomed in images of the voltage drop across the heater just after the ethylene has been started. a, shows the effect of different carbon flow rates at a constant temperature (630 °C), whereas b, shows the voltage drop for the same ethylene flow rate (6 sccm) at different temperatures.

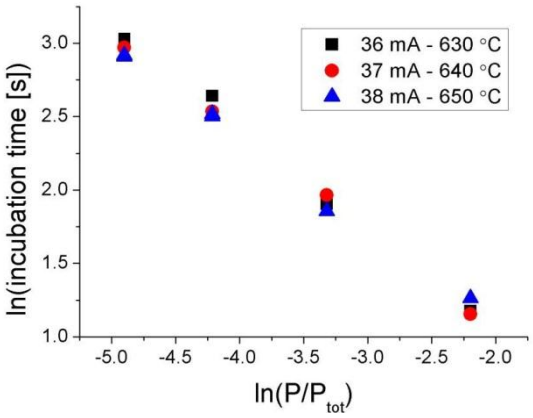

Figure 6.18. Plot of the logarithm of the incubation time before the voltage across the heater starts increasing as a function of the logarithm of the partial pressure of ethylene, plotted for different temperatures.

The incubation time before a Raman signal is detected is plotted versus the time it takes for the heater to reach its maximal voltage drop in Figure 6.19. It can be seen that these times are very similar, which indicates that the carbides form before the nanotubes start growing. This also suggests that the onset of nanotube growth is limited by the carbon supply rate and not on any temperature dependent reaction rate.

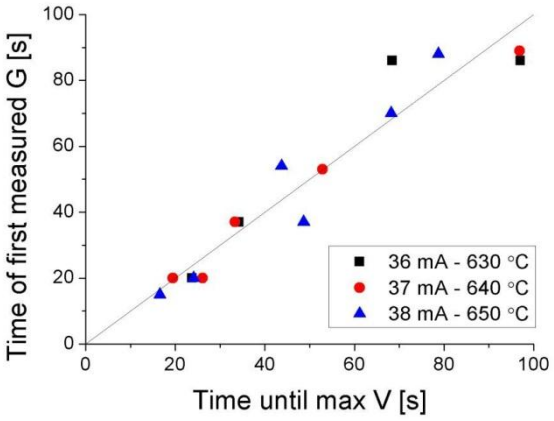

Figure 6.19. Plot of the time before a signal is detected in the G band area of the Raman spectra versus the time before the maximal voltage is measured across the heater. The line is not a fit but shows where the different times are equal, that is y=x.

The rate of increase of the voltage over the heater is faster at higher temperatures, as seen in Figure 6.17b. This rate of voltage increase is plotted in an Arrhenius plot in Figure 6.20. The gradient in this plot can be used to estimate an activation energy for the carbonisation process of the molybdenum heater. Activation energies of 2.1±0.2 eV and 2.7±0.1 eV were found for ethylene flow rates of 6 sccm and 30 sccm respectively. This can be compared with the activation energy for ethylene metathesis using molybdenum as catalyst, which is 2.4±0.2 eV [113]. This metathesis reaction creates degenerate ethylene molecules by recombination of carbenes on the surface of the molybdenum.

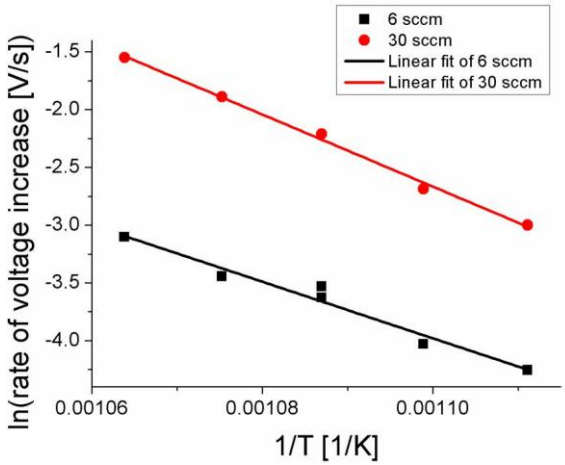

Figure 6.20. Arrhenius plot of the logarithm of the rate of voltage increase across the heater versus the inverse temperature for an ethylene flow of 6 and 30 sccm. The straight lines are least square fits of the data points.

6.2.4 Growth model

As previously discussed, the growth can be fitted by the relation [98, 108, 110]:

$$G(t) = v\tau(1 - \exp(-t/\tau)), \qquad 6.3$$

where G is the temporal evolution of the quantity of nanotubes, ν is the initial growth rate, τ is the lifetime and t the time. The fitted curves are shown in Appendix B, where the incubation time has been subtracted since this model does not take this into account. The evolution of the initial growth rate and the catalyst lifetime as a function of partial pressure is shown in Figure 6.21. It can be seen that the initial growth rate increases as the partial pressure of ethylene is increased, whereas the lifetime decreases. This behaviour can be described by a process where the growth is limited by mass transport of the carbon precursor. The evolution of the lifetime and the initial growth rates indicate that they are inversely correlated to each other. The growth and the deactivation process thus appear to be linked together. A similar trend was found in ref. [108], where a wider range of partial pressures was investigated. The same trend of increasing initial growth rate and decreasing lifetime was observed at low partial pressures of ethanol. At higher partial pressures both the initial growth rate and the lifetime became independent of the ethanol pressure. The lifetimes in ref. [108] are similar to the ones here. It is not possible to compare the initial growth rates since this depends on the area of the G band which is in arbitrary units and depends on the investigated system. In ref. [98] it was found that there is an optimal pressure of the carbon feedstock (ethanol was used) where the nanotube yield is maximised. The initial growth rate linearly increased with the pressure below this optimal pressure.

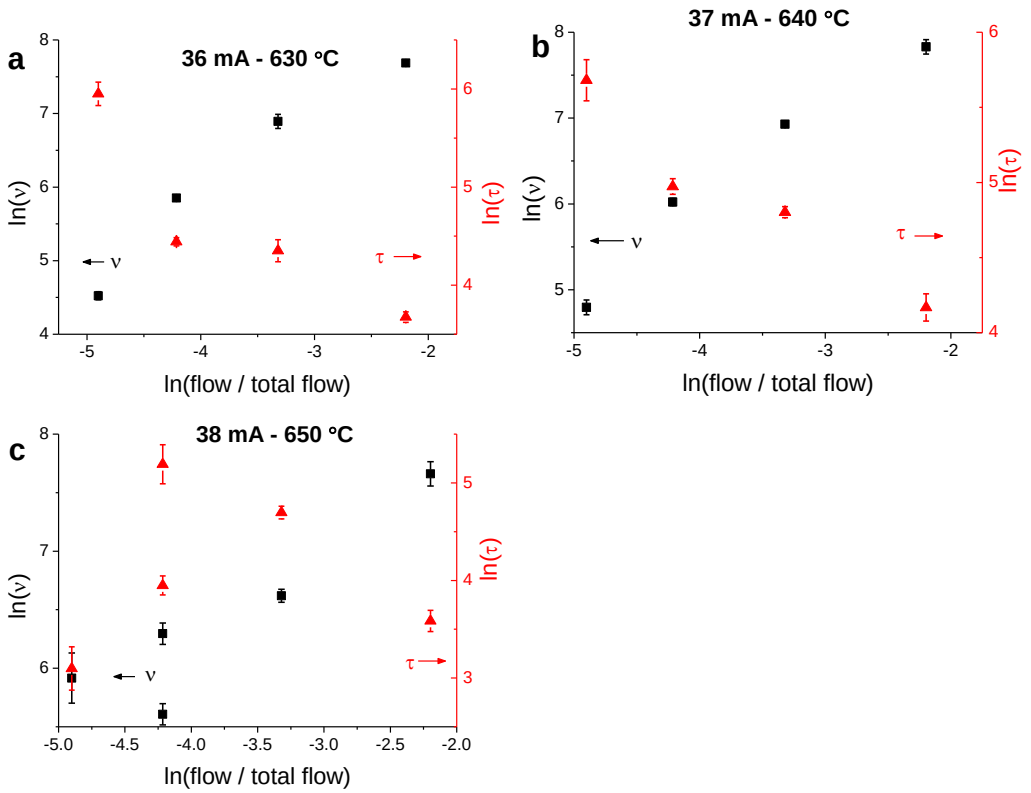

Figure 6.21. Plots of the logarithm of the initial growth rate (squares) and of the logarithm of the catalyst life time (triangles) versus the logarithm of the partial pressure of ethylene. a, is at a temperature of 630 °C, b, at 640 °C and c, at 650 °C.

A similar trend can be seen in the plot of initial growth rate and lifetime against inverse temperature for an ethylene flow of 6 sccm, see Figure 6.22a. That is, the initial growth rate increases and the lifetime decreases as the temperature is increased. This again suggests that the initial growth rate and the lifetime are inversely correlated. It is more difficult to see any trend in the case of a flow rate of 30 sccm, Figure 6.22b, although the catalyst lifetime appears to be independent of the temperature for lower temperatures. A similar trend was found for low temperatures in ref. [108], whereas the initial growth rate became independent of the temperature while the lifetime started to increase at high temperatures.

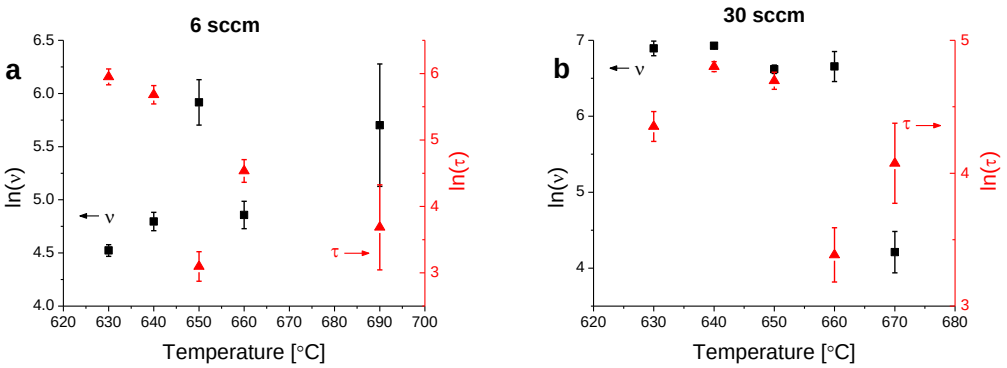

Figure 6.22. Plots of the logarithm of the initial growth rate and of the logarithm of the catalyst life time versus the temperature. a, is for an ethylene flow rate of 6 sccm and b, is for 30 sccm.

Figure 6.23 shows that the D peak follows the same trend, that is an increasing initial growth rate and a decreasing lifetime for higher ethylene partial pressures. It can also be seen that the values are similar but lower for the D peak compared to the G peak.

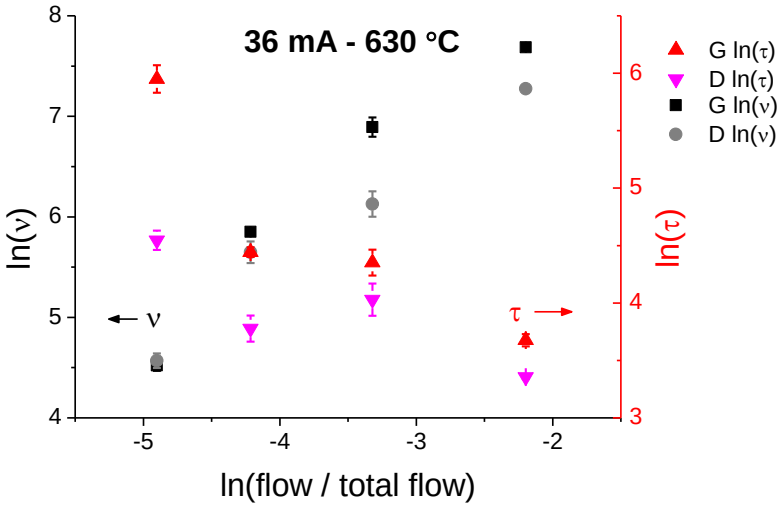

Figure 6.23. Plots of the logarithm of the initial growth rate of the G and D peaks and of the logarithm of the catalyst life time versus the logarithm of the partial pressure of ethylene.

The carbon not only reacts with the catalyst directly from the gas phase, but can first react with the molybdenum heater. The resistance of the heater is seen to increase when the carbon feedstock is supplied, which is due to carbide formation on the heater. This process can also form carbon chains on the heater. Carbon chains of up to eight carbon atoms have been found to form on molybdenum in an ethylene atmosphere at elevated temperatures [113]. Raman peaks in the range where polyynes and cumulenes are resonant have also been

observed here, see Figure 6.24. Polyynes are linear carbon chains with alternating triple- and single-bonds (C≡C-C), whereas cumulenes are linear carbon chains with double bonds between the carbon atoms. The position of the peak in the Raman spectrum depends on the length of the polyyne chain, see Figure 6.25, and also on the wavelength of the excitation laser and on the environment [114]. The Raman spectra of polyynes and cumulenes encapsulated inside CNTs was investigated in ref. [115]. Four different excitation wavelengths (514, 532, 633 and 785 nm) were used but the polyyne and cumulene peaks could only be observed by the 785 nm laser, which resulted in spectra very similar to what is shown in Figure 6.24. It would be interesting to investigate the time evolution of these peaks *in situ* during nanotube growth, but just as in ref. [115] no Raman peaks were observed by short excitation wavelengths whereas the thermal background is too strong when using a laser wavelength of 785 nm.

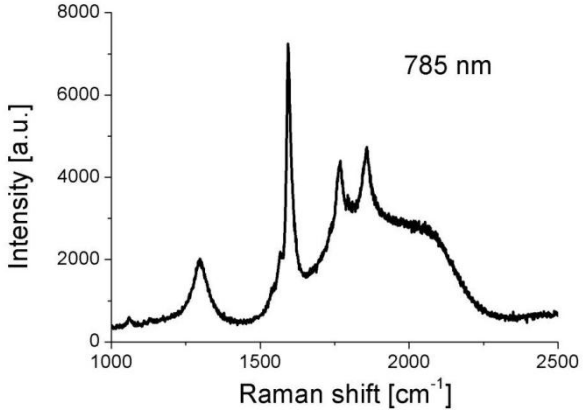

Figure 6.24. The peaks to the right of the G band (~1600 cm^{-1}) originate from linear carbon chains. This spectrum was obtained using a laser excitation wavelength of 785 nm and a laser power density of approximately 0.1 $mW/\mu m^2$.

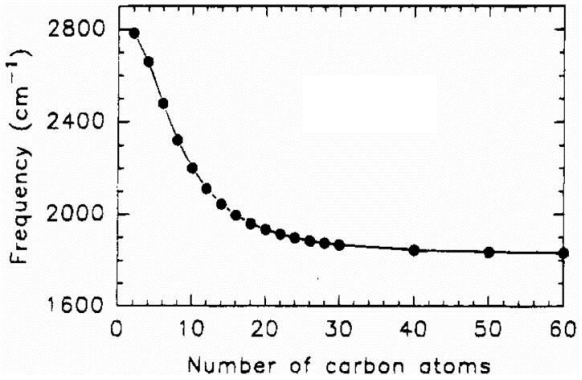

Figure 6.25. Graph showing how the frequency changes as the number of atoms in the polyyne chain increases. From [114]

These polyyne chains could play a very important role in the growth of carbon nanotubes. Eres et al. discuss in ref. [116] that the carbon feedstock self-assembles into progressively larger structures, such as polyynes and graphene fragments, and eventually form nanotubes. In this model, the active site is therefore moved from the catalyst particles to the carbon itself.

In Figure 6.19 it could be seen that the heater is chemically modified before the nanotubes start growing. The heater thus may form carbides and polyyne chains on the surface which are transported along the heater to the catalyst where they form nanotubes. Another indication of this additional pathway is that the longest nanotubes that have been grown using the local heating technique here, were grown on samples with only three separated catalyst islands instead of the 30 that typically are deposited on the heater, see Figure 6.26. Consequently, the carbon deposited on the heater is here only supplied to one tenth of the number of catalyst islands. If there is a limited amount of carbon that can reach the catalyst by going through or on the heater (instead of directly reacting with the catalyst) before the molybdenum is poisoned or saturated, this would explain why longer nanotubes can be grown from these three catalyst islands since more carbon is supplied to fewer catalytic sites.

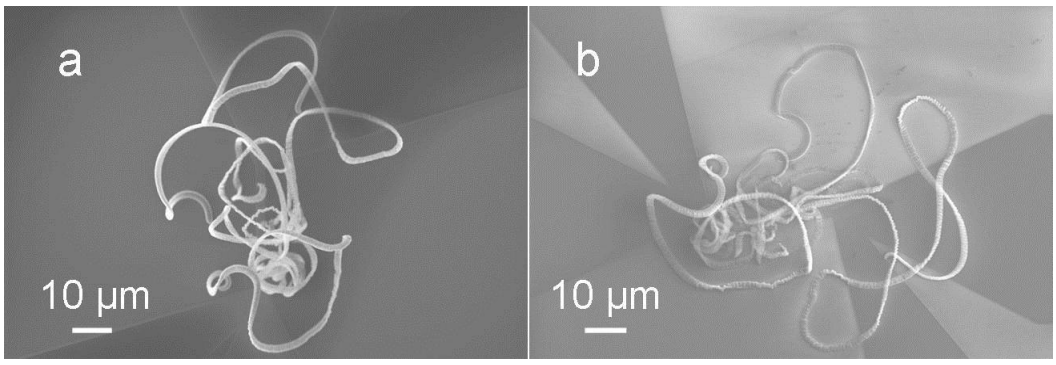

Figure 6.26. SEM images of nanotubes grown on a sample with three separated catalyst islands. These nanotubes were grown using 6 sccm of acetylene. b, shows the same nanotubes as in a, but after these had been exposed to the electron beam in the SEM for a few minutes, they fell down on the substrate.

The carbon nanotube growth rate can be very high in this system, as discussed in Chapter 5. Reported growth rates are often in the range of fractions of µm/s, sometimes more conveniently measured in µm/min, whereas values higher than 8 µm/s have been measured here. This difference becomes more significant when considering that the gases in the local heating setup are cold, whereas the gases are heated to several hundred degrees in

conventional CVD. Hart *et al.* found that heating the gases can increase the growth rate by more than an order of magnitude [38]. This increase was attributed to decomposition of the ethylene precursor into species that could be processed faster by the catalyst. Consequently, from this point of view the growth rates should be significantly lower in the local heating method used here where the carbon precursor is cold when it arrives at the heater. This could indicate that the high growth rates achieved here may be due to the additional carbon pathway through or along the heater.

6.3 Conclusions

Carbon nanotube growth was investigated by *in situ* Raman spectroscopy using two different modes. In one mode the nanotube growth was rapidly stopped after selected growth times, which allowed careful investigation by Raman spectroscopy at these time steps. Several different laser excitation wavelengths were used to study the growth at each time step and Raman spectra were measured both in the RBM and in the D-G regions. It was found that the G/D ratio initially decreases, which could be due to formation of amorphous carbon or growth of more defective nanotubes. As the growth continues the D peak starts to decrease in size again, suggesting that the nanotubes are annealed. More peaks appear in the RBM region as the growth time increases showing that the distribution of nanotube diameters broadens and appears to shift to nanotubes with a larger diameter.

The carbon nanotube growth was also investigated by Raman spectroscopy in real time. The growth could be well described by a growth model using the initial growth rate and the catalyst lifetime as parameters. It was found that the growth was limited by mass transfer of carbon to the catalyst. The IV characteristics of the heater were monitored during the nanotube growth. It was found that the heater is carbonised before the nanotubes start growing. The cold gases that are used in the local heating technique are expected to significantly reduce the nanotube growth rate. Despite this, extremely fast growth rates have been recorded for nanotube growth using acetylene as carbon feedstock. One explanation for this could be that the molybdenum heater creates an additional pathway for the carbon from gas phase to nanotube formation at the catalyst.

Arrays of MWCNTs grow at low temperatures whereas SWCNTs grow at higher temperatures. The temperature where this change occurs depends on the concentration of the carbon precursor such that higher concentrations increase the crossover temperature. For

growth of arrays of MWCNTs it was found that the growth rate is significantly slower when ethylene is used as carbon feedstock compared to when acetylene is used.

Chapter 7 Effect of laser heating on the Raman spectra of carbon nanotubes

When a molecule is heated it can change its properties. This is reflected in the Raman spectra as a shift of the position of the Raman peaks. The temperature dependence of the Raman spectra of carbon nanotubes has been studied by several groups [117-120].

The effect of different temperatures on the Raman spectra for double-walled carbon nanotubes, DWCNTs, in liquid methanol was studied in ref. [119]. It was found that both the D and G peaks shift to lower wavenumbers at the same rate (-0.024 cm^{-1}/K) as the temperature is increased at the relatively low temperatures that were investigated (180-320 K). The laser power was kept at 1 $mW/\mu m^2$. The Raman shift of the DWCNTs was also investigated in air as a function of laser power [119]. The laser power was varied from 1 to 100 mW but it is not mentioned how large the laser spot was. Under these conditions it was found that the spectral positions of the G and D peaks shift nonlinearly and that the G peak shifts approximately twice as much as the D peak when the laser power is increased.

The Raman shift as a function of temperature for SWCNTs was investigated in a wide temperature range (4-1000 K) in vacuum (< 10^7 Torr) in ref. [117]. A nonlinear shift of the G peak as a function of temperature was found for the whole range of temperatures. At high temperatures this shift can be estimated by a linear slope with a slope of about -0.03 cm^{-1}/K. A low laser power of 0.1 $\mu W/\mu m^2$ was used in these experiments.

MWCNTs were investigated in ref. [118] and shifts of about -0.019 cm^{-1}/K and -0.025 cm^{-1}/K were found for the D and G peaks respectively. The temperature was varied by changing the laser power in the range 0.32-6.4 $\mu W/\mu m^2$, which resulted in temperatures up to 550 °C.

In ref. [120], the temperature influence on the Raman spectrum of bundled HiPCO SWCNTs was investigated both by Raman spectroscopy and by molecular dynamics simulations. A shift of -0.0189 cm^{-1}/K was reported for the G peak, which shifted approximately twice as much as the D peak. The laser power was kept at 3 $mW/\mu m^2$ during the measurements and the acquisition time was 10 s. The authors mention that the laser heating effects were minimal. It was found that the negative shift of the RBM and G peaks mainly are due to softening of the intratubular C–C bonds and due to intertubular (van der Waals) interaction between the SWCNTs. The effect of thermal expansion of the SWCNTs at high temperatures was also investigated, but was found to not contribute significantly.

In this chapter the shift of the G and D peaks in the Raman spectra are investigated at different temperatures. The nanotubes are heated by the same laser as is used for the Raman measurements. The temperature is estimated from the blackbody radiation emitted by the hot nanotubes. This shows that the laser used for Raman measurements can significantly heat the nanotubes and that the temperature can be estimated from the blackbody radiation of the hot nanotubes.

7.1 Experimental

MWCNTs grown using the local heating method were investigated where they had been grown and MWCNTs grown by conventional catalytic CVD, CCVD, and deposited on silicon or quartz were investigated, see Figure 7.1. Three different samples grown using the local heating method were studied, labelled LH1-LH3. All of these were grown at 650 °C using 6 sccm acetylene, 300 sccm hydrogen and 500 sccm argon. Since these nanotubes are well aligned, see Figure 7.1a, the laser was aligned both parallel and perpendicular to the nanotubes in order to investigate any polarisation dependence.

SWCNTs are not investigated since they yield a too strong Raman signal, which makes it difficult to estimate the temperature from the blackbody shaped background. The nanotubes were placed under the Raman microscope in the chamber used for growth of nanotubes using the local heating technique. The chamber was evacuated and filled with Ar twice in order to remove all oxygen in the chamber. A flow of 50 sccm Ar was kept on during the measurements to minimise any effect of any possible leaks. One experiment was performed in nitrogen instead of the argon. Since the temperature is estimated from the blackbody radiation in the spectra, a long laser excitation wavelength was used (785 nm) in order to collect a maximal part of the blackbody spectrum. This is in contrast to most other cases when it is desirable to minimise the contribution from the blackbody radiation. The laser was focused to a spot size of about 15 μm^2.

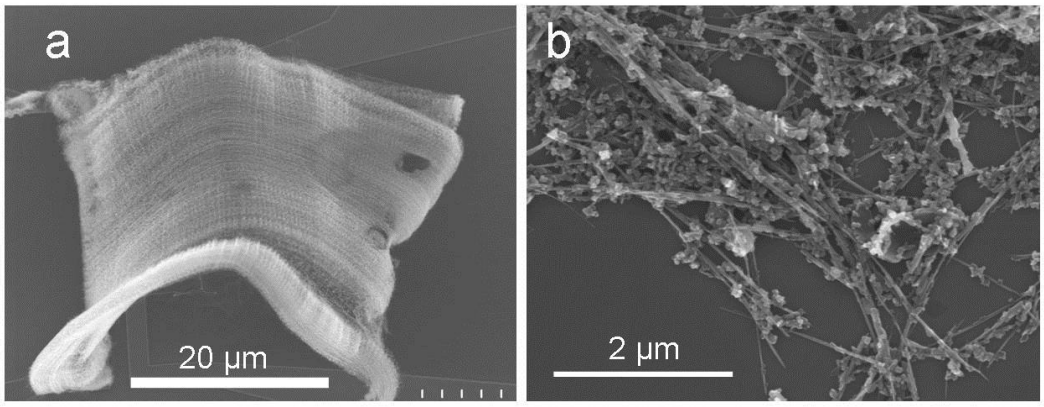

Figure 7.1. a, SEM image of MWCNTs grown using the local heating technique using 6 sccm acetylene, 300 sccm hydrogen and 500 sccm argon at 650 °C. b, SEM image of deposited MWCNTs grown using conventional CVD.

In the Renishaw inVia system that was used, the laser power of the 785 nm laser can be varied in certain steps by a combination of different filters. However, this step size was too large for this investigation of different laser powers. A polariser and an analyser were therefore added in the beam path. The analyser was kept at a constant angle in order to ensure that the laser polarisation on the sample was kept constant and thereby eliminate any dependence of laser polarisation. The laser power could then be continuously varied by rotating the polariser.

The power of the laser was measured indirectly by measurements of the signal obtained from an internal silicon reference sample. This could easily be measured just before every measurement of the nanotubes. The silicon signal was converted to laser power by calibration measurements where a power meter had been placed where the nanotubes otherwise would be. This resulted in a linear calibration curve from silicon signal to laser power, see Figure 7.2.

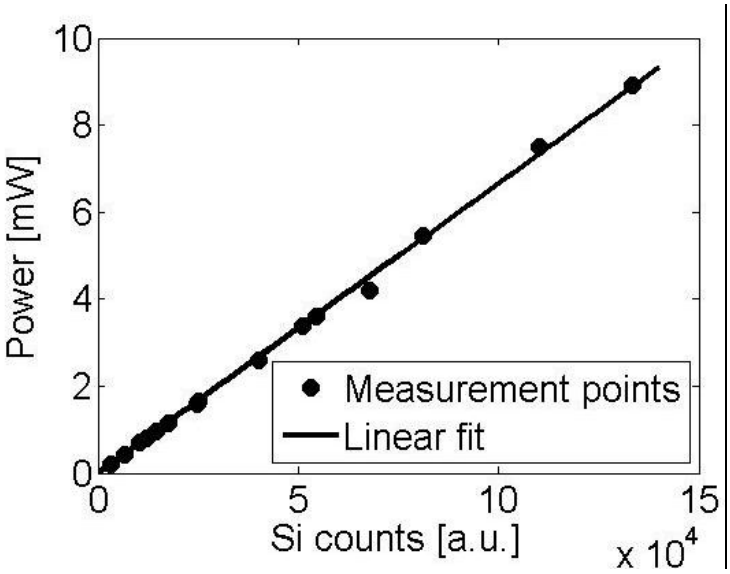

Figure 7.2. Calibration curve between laser power and measured intensity of an internal silicon reference sample.

The temperature of the nanotubes was determined from the measured blackbody spectrum as described in Chapter 3.3. Consequently, the temperature can only be estimated at relatively high temperatures since there has to be a reasonable blackbody signal for the temperature estimations. Raman spectra were also measured at low temperatures in order to see the shift of the peaks in the spectra, but no reliable temperature could be estimated from these measurements. For some samples, spectra with longer acquisition times were recorded in the D-G region in order to be able to determine the peak positions more accurately. These measurements are labelled GD in the legends of the figures.

The measurements were not done in order of increasing or decreasing laser power, but in a random order such that any hysteresis or effects of any drift could be eliminated.

7.2 Results

Figure 7.3 shows an example of spectra measured with different laser powers. There is no significant background at low powers and the Raman peaks from the nanotubes can clearly be identified, but as the power is increased the background grows larger and eventually drowns the Raman signal from the nanotubes.

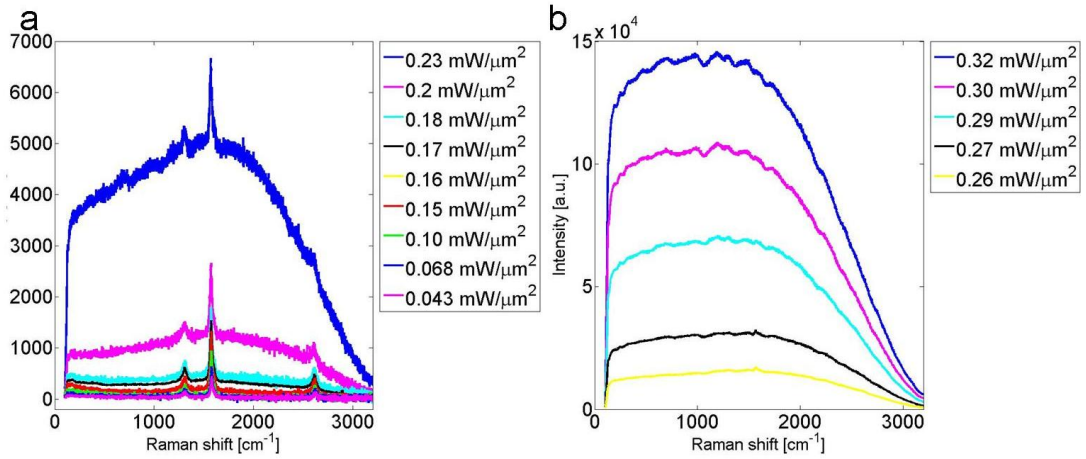

Figure 7.3. Raman spectra of MWCNTs for a range of different laser power densities using a wavelength of 785 nm. It can be seen that the background significantly increases for higher powers. a, shows the Raman spectra at lower laser powers and b at higher laser powers. The spectra are as measured by the Raman system before any corrections have been made.

As expected, the absolute area of the G band increases as the laser power is increased, see Figure 7.4a. Plotting this in a log-log graph yields that the intensity of the G band as a function of laser power follows a power law with a sublinear exponent (0.82), see Figure C.1 in Appendix C. This sublinear dependence could be due to broadening of the electronic bands as the temperature is increased which reduces the Raman cross section [119]. In ref. [119] a sublinear relation (0.85) was found for a short laser excitation wavelength (338 nm) whereas a superlinear relation (1.8) was found for a longer wavelength (647 nm). This sublinear relation could be explained by heating effects by the UV laser whereas the authors attributed the superlinear behaviour to excitons increasing the Raman resonance. Figure 7.4b shows the intensity of the G band divided by the laser power for different laser powers. It can be seen that this ratio slowly decreases as the laser power is increased. This is because the nanotubes at higher laser powers are hotter and therefore yield a lower Stokes Raman signal. The error in the areas at high laser power is larger than at low laser powers due to the significantly larger background.

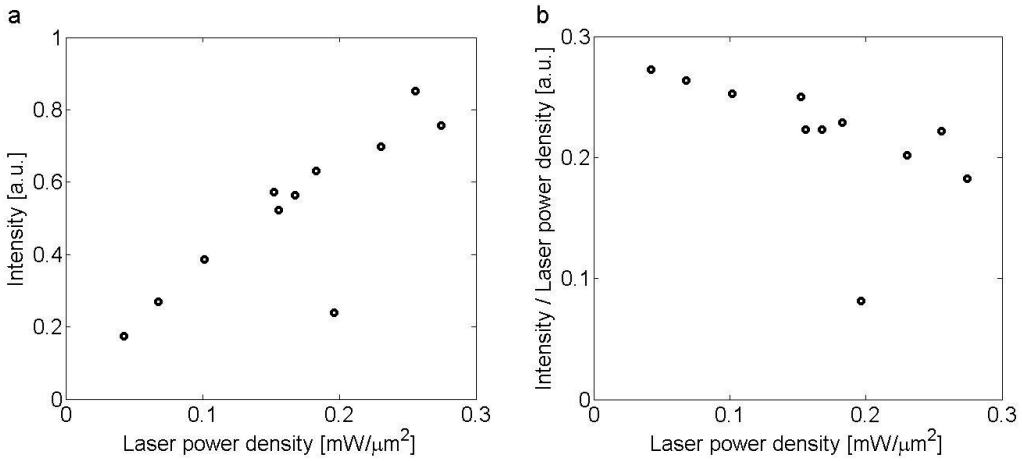

Figure 7.4. a, absolute area of the G band as a function of laser power density. b, area of the G band per power unit of the incoming laser light versus the laser power. Both graphs are for the same sample as is shown in Figure 7.3.

The different shape of the curves in Figure 7.3 is due to the nanotubes being heated to different temperatures at different laser powers and therefore emitting blackbody radiation with different shapes. This can be used to estimate the temperature as described in Chapter 3.3. Figure 7.5 shows that there is a linear dependence between the laser power and the temperature of the nanotubes. It can also be seen that higher laser powers are required to heat the nanotubes grown by standard CVD compared to the nanotubes grown by the local heating technique. This could be because these nanotubes are lying on the substrate which acts as a heat sink whereas the nanotubes grown by the local heating technique are arched in the argon with limited contact with the substrate, as shown in figure Figure 7.1. Especially for the nanotubes grown by conventional CVD, the intensity of the blackbody radiation was too low for any temperature estimations at low laser powers.

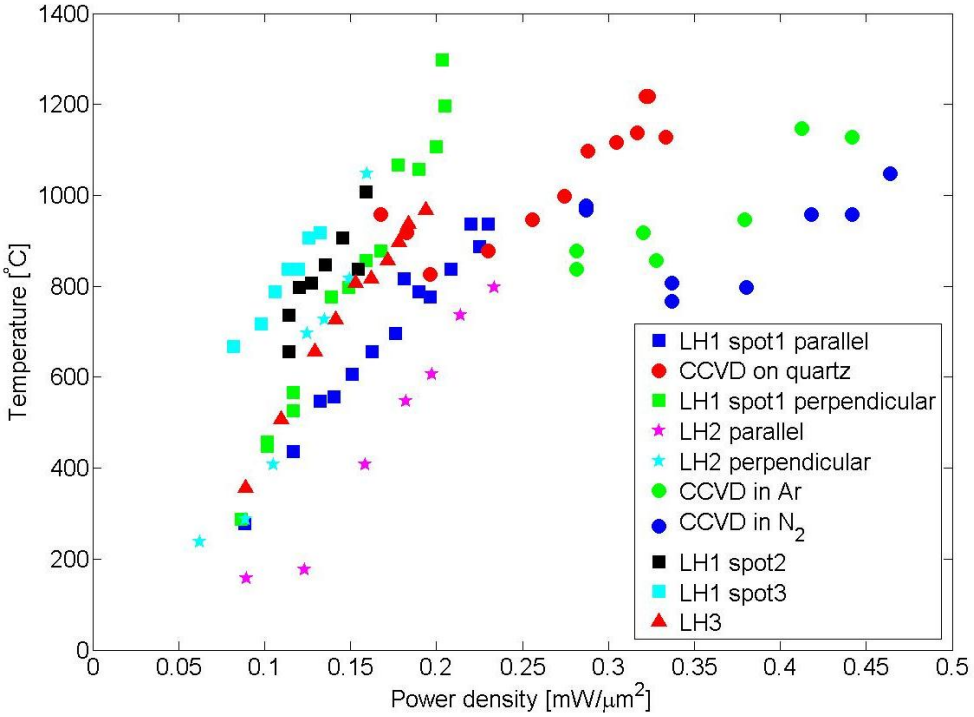

Figure 7.5. Temperature calculated from the blackbody spectra for several samples as a function of incident laser power density. LH stands for samples grown by the local heating technique whereas CCVD stands for samples grown by conventional catalytic CVD. Parallel and perpendicular refer to the laser polarisation compared to the direction of the nanotubes.

In order to get an estimate of the intensity of the emitted light, the area under the spectra between the G and G' peaks, after correction for the detection efficiency, is calculated for each laser power and temperature. This is plotted in a log-log graph for several samples in Figure 7.6 as a function of temperature and as a function of laser power in Figure C.2 in Appendix C. It can be seen that for each sample there is a linear dependence of the logarithm of the intensity as a function of the logarithm of the temperature. Consequently, the intensity of the emitted light follows a power law. This dependence is summarized in Table 1.

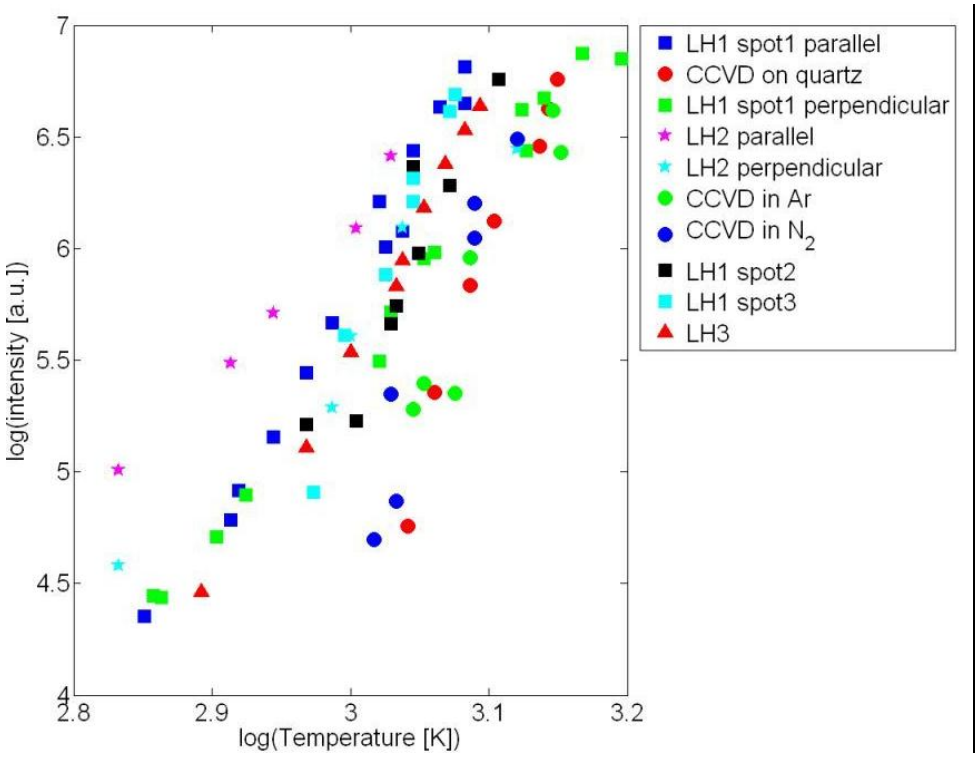

Figure 7.6. Logarithm of the area under the spectra between the G and G' peaks as a function of the logarithm of the temperature. It can be seen that there is a linear relationship which indicates a power law dependence between this intensity and the temperature. LH stands for samples grown by the local heating technique whereas CCVD stands for samples grown by conventional catalytic CVD. Parallel and perpendicular refer to the laser polarisation compared to the direction of the nanotubes.

The spread in exponents between different samples is quite large, see Table 1. The spread is larger for the intensity of the light as a function of temperature than as a function of laser power, which is due to the uncertainty in the temperature measurements. There are also fewer data points for the temperature dependence since the temperature can not be estimated for low laser powers.

Table 1. Summary of the power law dependences between the intensity of the area under the Raman spectrum between the G and G' peaks as a function of laser power and temperature respectively. LH stands for samples grown by the local heating technique whereas CCVD stands for samples grown by conventional catalytic CVD.

Sample	P^	T^
LH1 spot1 parallel	8.4	10.9
CCVD on quartz	9.8	17.0
LH1 spot1 perpendicular	8.1	7.8
LH2 parallel	7.3	6.9
LH2 perpendicular	10.2	6.7
CCVD in Ar	8.8	12.2
CCVD in N_2	11.7	17.0
LH1 spot2	9.2	12.3
LH1 spot3	8.8	16.2
LH3	8.6	11.2
Average	9.1±1.2	11.8±4.0

According to the Stefan-Boltzmann law, the energy radiated by a blackbody is proportional to the fourth power of its temperature. The value found here is significantly higher (11.8 ± 4.0). This is because only a very small part of the spectrum is investigated here, whereas the Stefan-Boltzmann law is for the full spectrum. This becomes important since not only the intensity but also the shape of the blackbody curve changes with temperature, see Figure 7.7. In our case, the intensity is measured between the G and G' peaks, which approximately corresponds to 900-950 nm. These measurements are taken in the temperature interval 600-1200 °C. In this temperature and wavelength intervals, the blackbody intensity scales with temperature with an exponent of 13.8 ± 0.5, which is in fairly good agreement with the results found here.

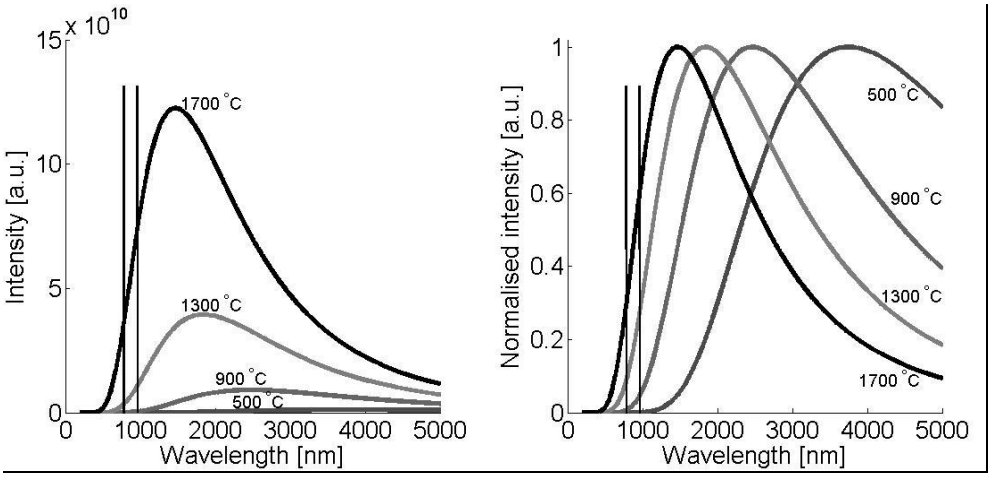

Figure 7.7. a, Blackbody curve for different temperatures. b, as in a, but the different curves have been normalised to their maximum values in order to highlight the wavelength shift of the maxima. It can be seen that both the intensity and the shape of the curves change as the temperature changes. The two vertical lines show the region which approximately corresponds to the region between the G and G' peaks.

As discussed above, the position of the G peak in the Raman spectrum shifts when the temperature is increased. Figure 7.8 shows that the position of the G peak linearly shifts downwards as the power is increased. For an increase in laser power the spectral position of the G peak changes less for the CCVD nanotubes than for the nanotubes grown by the local heating technique. This is expected since a higher laser power is required to heat the CCVD nanotubes.

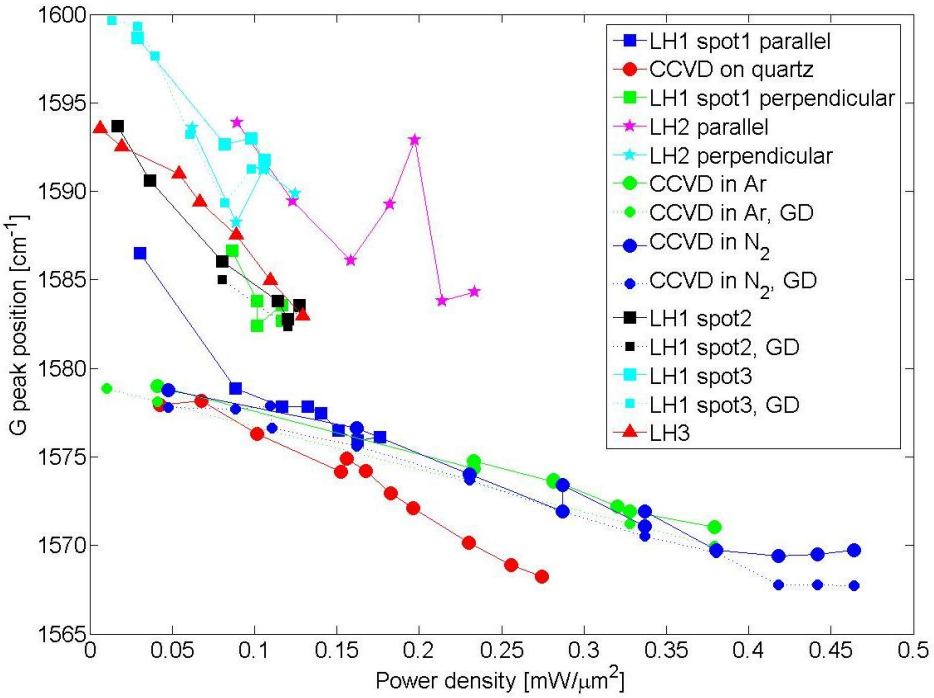

Figure 7.8. Spectral position of the G peak as a function of the incident laser power density. LH stands for samples grown by the local heating technique whereas CCVD stands for samples grown by conventional catalytic CVD.

Figure 7.9 shows the Raman shift of the G peak as a function of temperature. The G peak is more pronounced at lower temperatures and laser powers whereas the blackbody signal is stronger at higher temperatures and laser powers. Consequently, the position of the G peak can be determined more accurately at low laser powers where the blackbody signal is too low for any temperature estimates. Since the overlap between these two regimes is rather small, there are only a few data points in Figure 7.9. In order to get an overall trend, a linear relationship was calculated between the spectral position of the G peak and the laser power and another between the temperature and the laser power:

$$\begin{aligned} G &= \mathrm{a}P + \mathrm{b} \\ T &= \mathrm{c}P + \mathrm{d} \end{aligned}, \qquad 7.1$$

where G is the spectral position of the G peak, P the laser power, T the temperature and a, b, c and d are constants. These two equations can be combined to give a temperature dependence of the G peak position:

$$G = \frac{a}{c}T + b - \frac{ad}{c} \qquad 7.2$$

This is represented by the straight lines in Figure 7.9 and the values of the gradients are listed in Table 3.

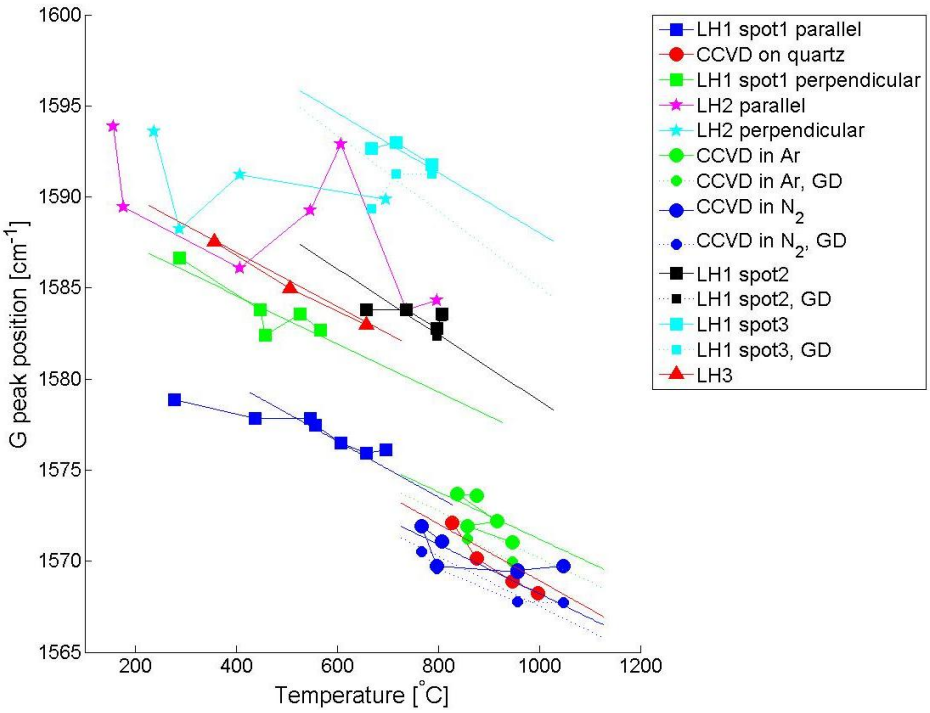

Figure 7.9. Position of the G peak in the Raman spectrum for several samples as a function of temperature. The straight lines are calculated using linear fits as described in the text.

The nanotubes grown with the local heating technique are well aligned, see Figure 7.1. The laser could therefore be aligned parallel and perpendicular to the nanotubes in order to investigate any polarization dependence. The spectral position of the G peak is found at higher wavenumbers for perpendicular laser polarisation. All other trends, such as the temperature shift, are very similar for the different polarizations. The temperature behaviour of the CCVD nanotubes is independent of whether they were deposited on silicon oxide or quartz and whether the measurements were done in argon or nitrogen.

The linear relationship between laser power and peak position can be used to estimate the spectral position of the peaks in a situation without any influence from the laser power, that is where the laser power is 0 mW. These positions are summarised in Table 2 and shown for all samples in Table C.1 in Appendix C. It was found that there is a large difference in spectral position of the G peak between the nanotubes grown by conventional CVD and the nanotubes grown using the local heating method. This could be due to graphitic material other than nanotubes yielding a significant Raman signal. In Figure 7.1b it can also be seen

that the deposited nanotubes are dirty. The G peak is centred around 1580 cm^{-1} for graphene [66].

Table 2. Summary of the estimated spectral positions of the G and D peaks if unaffected by the laser power, that is for a laser power of 0 mW.

Sample	Estimated G position at 0 mW laser power [cm^{-1}]	Estimated D position at 0 mW laser power [cm^{-1}]
Conventional CVD	1580 ± 1	1315 ± 3
Local heating	1595 ± 5	1307 ± 3

Similar effects as for the G peak can be seen for the D peak as a function of laser power and temperature, see Figure 7.10 and Figure 7.11. The D peak shifts to lower wavenumbers as the temperature is increased, similarly to the behaviour of the G peak.

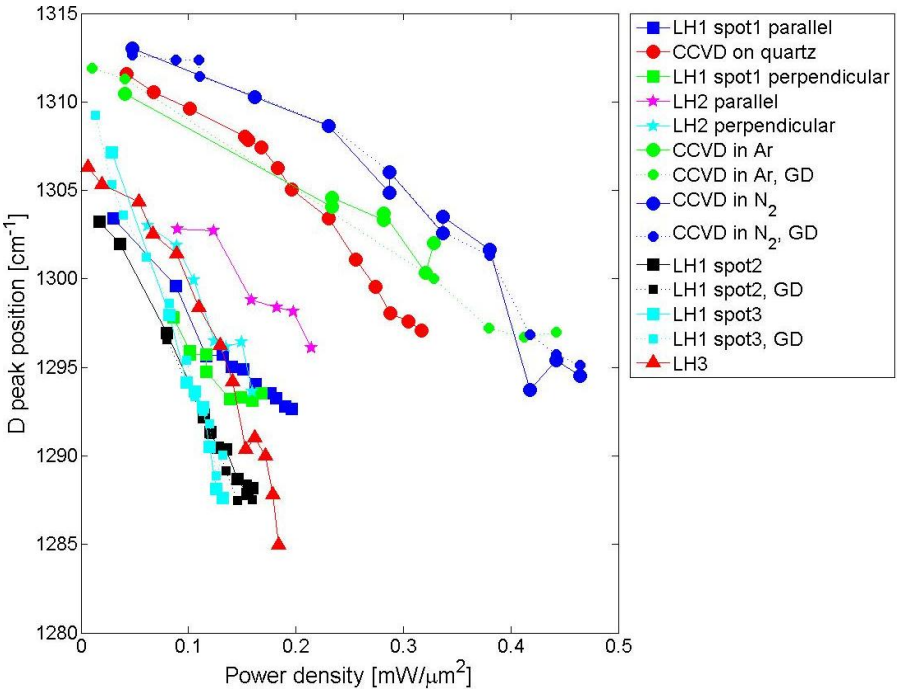

Figure 7.10. Position of the D peak in the Raman spectrum as a function of laser power density for several different samples.

The D peak is positioned at higher wavenumbers for the nanotubes grown by conventional CVD compared to the nanotubes grown by the local heating technique, see Figure 7.10 and Figure 7.11. The average spectral shift of the D peak is similar for the nanotubes grown by the different methods but the spread is significantly broader for the nanotubes grown by the local heating technique. The temperature dependence on the spectral position of both the D and G peaks are summarised in Table 3.

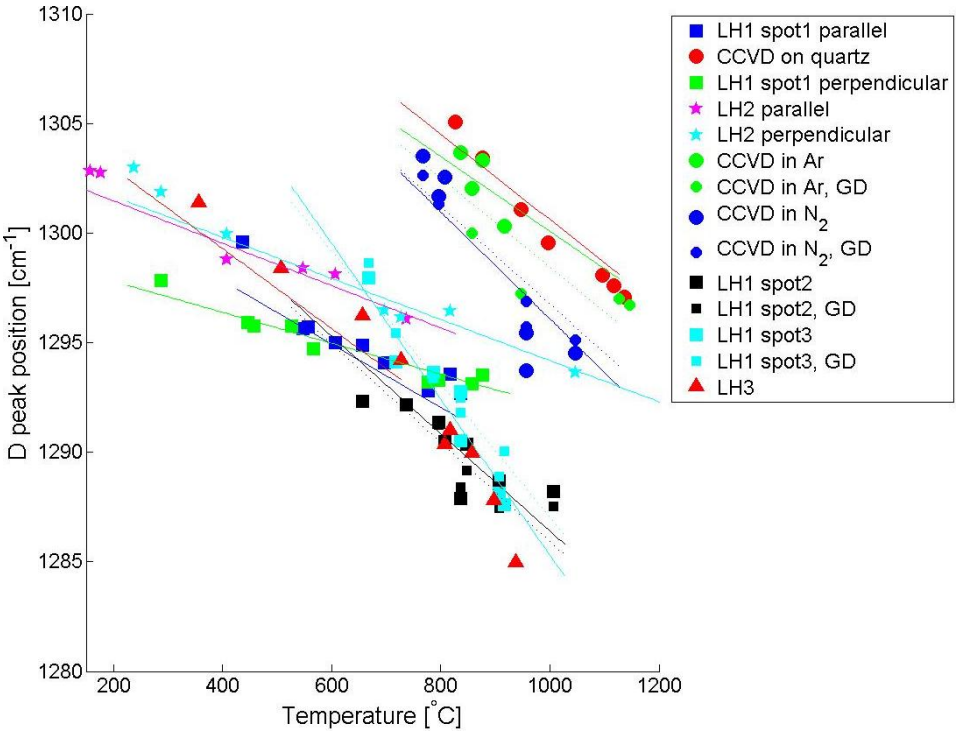

Figure 7.11. Spectral position of the D peak as a function of temperature for several different samples. LH stands for nanotubes grown by the local heating technique whereas CCVD stands for nanotubes grown by standard CVD.

In Table 3 it can be seen that the values of the shift of the spectral position of the G peak as a function of temperature found here are lower than what is generally reported in literature [117-120]. The shifts of the D peak here are similar to what has been found elsewhere [118-120].

Table 3. Summary of the temperature dependent spectral shifts of the G and D peaks in the Raman spectrum. LH stands for nanotubes grown by the local heating technique whereas CCVD stands for nanotubes grown by standard CVD.

Sample	G shift [cm^{-1} / K]	D shift [cm^{-1} / K]
LH1 spot1 parallel	-0.015	-0.014
CCVD on quartz	-0.016	-0.019
LH1 spot1 perpendicular	-0.013	-0.0070
	-0.014	-0.011
LH2 parallel	-	-0.0097
LH2 perpendicular	-	-0.0094
CCVD in Ar	-0.013	-0.017
	-0.013	-0.020
CCVD in N_2	-0.013	-0.024
	-0.014	-0.022
LH1 spot2	-0.018	-0.022
		-0.023
LH1 spot3	-0.017	-0.036
	-0.021	-0.030
LH3	-0.015	-0.018
Average:		
CCVD	-0.014±0.001	-0.021±0.002
Local heating	-0.016±0.003	-0.018±0.01
Literature	-0.02 to -0.03 [117-120]	-0.01 to -0.025 [118-120]

It is possible to heat the nanotubes using different laser excitation wavelengths. Figure 7.12 shows the spectral shift of nanotubes when irradiated by a wavelength of 514 nm. These measurements are so far down on the blackbody tail that any temperature estimates using the blackbody radiation become too uncertain. This chapter was therefore focused on experiments using a laser excitation wavelength of 785 nm.

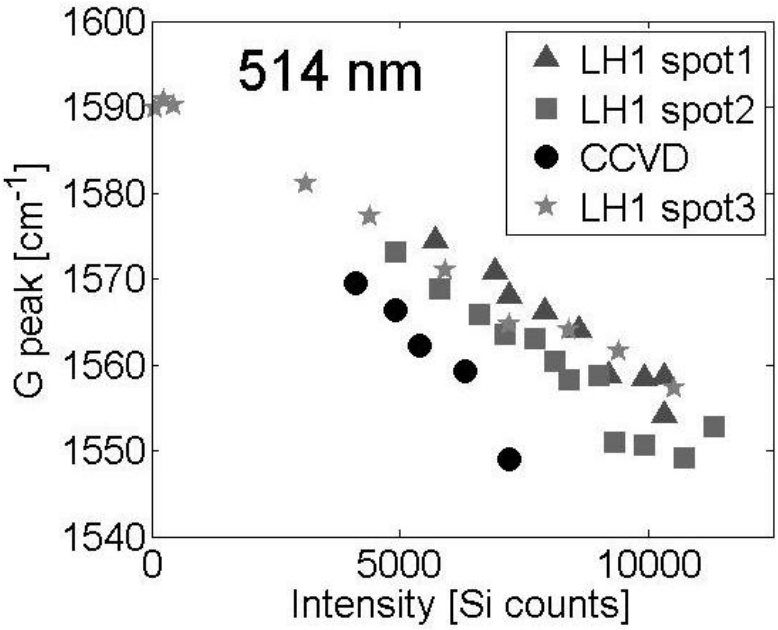

Figure 7.12. Spectral position of the G peak when using an excitation wavelength of 514 nm as a function of counts on an internal silicon reference sample, which is linear in laser power. There is a clear downshift of the G peak position. The temperature can not be estimated at these short wavelengths.

7.3 Conclusions

Carbon nanotubes can be heated significantly by a laser commonly used in Raman spectroscopy. An excitation wavelength of 785 nm was used to allow temperature estimations from the blackbody radiation of the hot nanotubes. The laser power density was varied in the range 5-500 $\mu W/\mu m^2$, which resulted in nanotube temperatures up to approximately 1100 °C. This shows that even low power densities can heat the carbon nanotubes to high temperatures and that care has to be taken during Raman measurements. Strong backgrounds in the nanotube Raman spectrum are often attributed to photoluminescence, but blackbody radiation can also be an important factor.

The temperature can, for example, be estimated by the difference between the Stokes and anti-Stokes signals or the temperature shift of the silicon peak. Here we show that the temperature can also be estimated by the blackbody radiation from the nanotubes.

The different behaviour of the nanotubes grown by local heating CVD and conventional CVD can be explained by considering that the former are suspended whereas

the latter are lying on the substrate. The samples grown by conventional CVD contain carbon material in other forms than nanotubes which shifts the behaviour from that observed with the nanotubes grown by local heating.

Chapter 8 Electromechanical properties of vertically aligned carbon nanotubes

Carbon nanotubes have been extensively studied and suggested for applications in electronics [121]. They are promising both as conductors of current and of heat [122-124]. Nanotubes are, for example, considered as replacements for copper wires in via holes [125]. This is interesting since they can withstand up to 1000 times higher current densities and they are very good thermal conductors [4]. The possibility of using carbon nanotubes as transistors is also being investigated [126], as well as field emission electron sources [127]. CNTs can also be used as electrodes in sensors, due to their low power consumption and large surface area [128]. Carbon nanotubes can be grown as vertically aligned structures in many different geometries determined by the catalyst pattern and the height of these arrays can be tuned by the growth time of the nanotubes and what conditions are used, as has been seen throughout this thesis and is discussed in ref. [76]. These arrays can be used to form large films that are being investigated as promising actuator materials [129]. There have however not been as many studies on mechanical actuation properties of directly grown vertically aligned nanotubes. In ref. [130] it was found that nanotube arrays can be compressed under a mechanical load. The nanotubes then buckle forming patterns similar to the patterns shown here in Figure 5.8 and Figure 5.9 in Chapter 5. The nanotubes straighten and retain their original shape when the load is removed.

Another possible application of CNTs, the varactor, is investigated here. A varactor is a device that can change its capacitance on application of a bias voltage.

A capacitor can be thought of as two metal plates separated by a short distance. The capacitance, *C*, can be calculated by:

$$C = \varepsilon_r \varepsilon_0 A/d, \qquad 8.1$$

where ε_r is the relative permittivity, ε_0 the permittivity in vacuum, *A* the area of the two plates and *d* the distance between them. The capacitance can therefore be varied by changing the separation between these plates, and thus forming a varactor.

Carbon nanotubes have a very high surface area and are therefore interesting as material for capacitors since the capacitance depends on the surface area. They have therefore been investigated as one electrode in a capacitor [131]. A dielectric layer was deposited on the MWCNTs, followed by deposition of a metal layer forming the second electrode, see Figure 8.1. The carbon nanostructures were synthesised by a dc-PECVD process that typically results in nanofibres and not nanotubes, but the authors described them

as MWCNTs. 40 000 structures were fabricated since the capacitance from a single structure was expected to be too small to measure. The capacitance was estimated to be 1.027 fF for each individual nanotube.

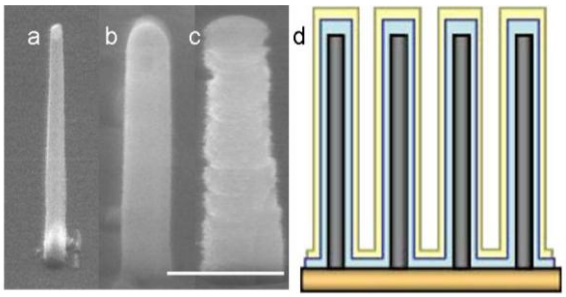

Figure 8.1. a, shows a SEM image of a single nanofibre, b, after deposition of a Si_3N_4 layer on the nanofibre and, c, after deposition of an Al layer. The scale bar is 500 nm. d, shows a sketch of the final capacitor structure, the nanofibres are grey, the Si_3N_4 layer light blue and the Al is yellow. Adapted from [131].

These nanofibres were later used to make a nanoscale switched capacitor [132]. Two nanofibres were grown on different electrodes. One of the nanofibres was covered with a dielectric layer and a thin metal layer, see Figure 8.2. A constant voltage was applied between these such that, when an even higher voltage was applied to the gate electrode, the uncovered nanofibre was actuated and came into contact with the covered nanofibre. The metal layer was thus charged and a capacitor was formed.

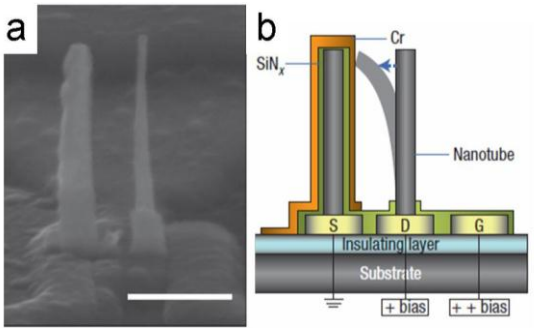

Figure 8.2. a, shows a SEM image of a fabricated device structure and b, shows a schematic diagram of the structure. A positive bias applied to the drain (D) and the gate (G) can deflect the nanofibre on the right hand side into contact with the structure on the left hand side, which charges the capacitor device. Removal of the bias can cause the nanofibre to go back to the vertical position, leaving the capacitor in a charged state. Adapted from [132].

Dragoman and Dragoman have studied actuation of single pairs of nanotubes [133]. The capacitance between two single nanotubes is very low. It is therefore necessary to use many pairs in parallel. Dragoman and Dragoman suggested to make a network of 1000 x 1000 single nanotubes. Ghavanini *et al.* are investigating a similar structure but using arrays of individual carbon nanofibers instead of carbon nanotubes [134]. These nanofibers are very small and consequently have to be placed very close together to yield higher capacitances. An individual pair of these fibres is shown in Figure 8.3. Isacsson and Kinaret have also modelled resonances in arrays of individual nanotubes when electrostatically actuated [135].

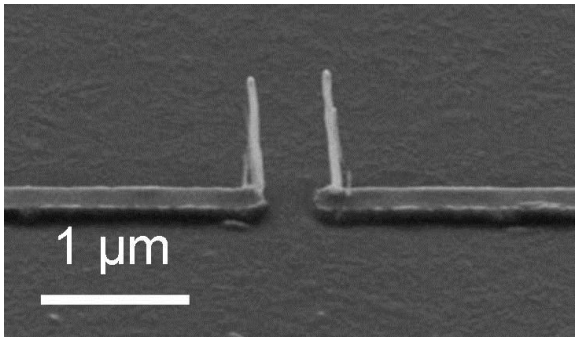

Figure 8.3. SEM image of a single nanofibre structure studied in ref. [134]. Adapted from [134].

In this chapter the possibility of making a varactor of nanotubes, and what more we can learn from such a structure, is investigated. The focus here is on growing vertically aligned arrays of MWCNTs and changing the separation between these arrays by applying a DC voltage between them. This creates an electrostatic force between the arrays, pulling them closer as the voltage is increased. The actuation was studied using an optical microscope and SEM. It was found that the arrays of nanotubes move as a single cohesive unit. A relatively low voltage was sufficient to actuate the arrays. The effective Young's modulus of the structure was found to be very low, less than 5 MPa, which is less than that of rubber. This is attributed to the low density and quasi-alignment of the nanotubes, which allow them to slip and slide against each other.

The devices were not intended to be competitive with commercial varactors, but the experiments were intended as proof of principle experiments. It was found that the devices can accurately be modelled by an equivalent electrical circuit. By fitting simulated scattering parameters with measured parameters the capacitance is found at selected actuation voltages. The model is found to accurately describe the system. The relatively low actuation voltage and the inherent properties of carbon nanotubes make this interesting for development of

micro- and nano-electromechanical devices. This therefore forms the basis for developing practical devices based on carbon nanotube arrays.

8.1 Experimental

A few different geometries were investigated by designing different catalyst patterns. However, the alignment of the nanotubes was a problem for both square and line shaped catalyst patterns, see Figure 8.4. This can be compared with the results by Jeong *et al.*, who found that the alignment depends on the size of the nanotube arrays and is worse for thinner arrays [136].

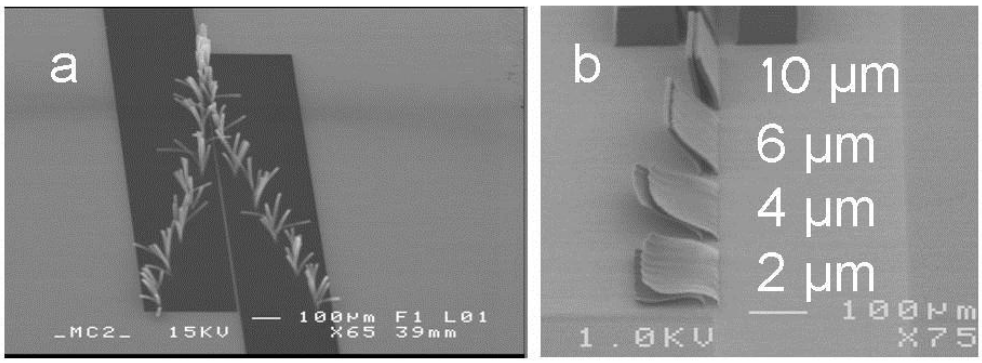

Figure 8.4. a, SEM image of nanotubes grown from square shaped patterns. b, SEM image of nanotubes grown from a rectangular catalyst shape with different widths, as listed in the image. It can be seen that the alignment is poor for the square shaped arrays and becomes better for thicker rectangular shaped arrays.

In order to improve the stability of the arrays, "support legs" were added, see Figure 8.5. A few different configurations were tested, 2, 3 or 5 supports. The added nanotubes do not contribute substantially to the capacitance but improve the mechanical stability significantly and thereby also the alignment. The structures in Figure 8.5 are examples of structures with 3 supports. The alignment was significantly increased, but this also makes it more difficult to actuate the arrays. The separation as a function of applied actuation voltage is shown in Figure 8.6 for several different test configurations. As expected, it can be seen that it is significantly more difficult to actuate the arrays with more support legs. The arrays with two support legs were therefore chosen for further experiments. Short arrays are also difficult to actuate, whereas the alignment becomes more difficult for longer nanotubes. The thickness of the arrays is also important, as can be seen above in Figure 8.4. The initial

separation of the nanotubes influences the initial capacitance. It is also an important factor for the alignment, since the shorter the separation is the better the alignment has to be. In order to get a maximal separation change for a minimal voltage a width of 4 µm and a separation of 10 µm were chosen.

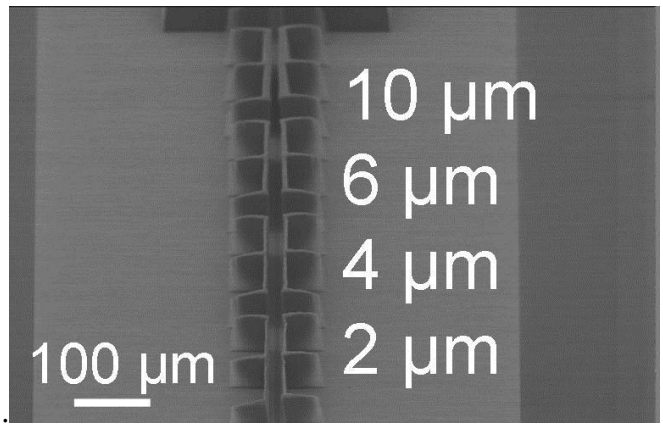

Figure 8.5. SEM image of arrays grown with three support legs and with different widths of the catalyst resulting in nanotube arrays with different thicknesses.

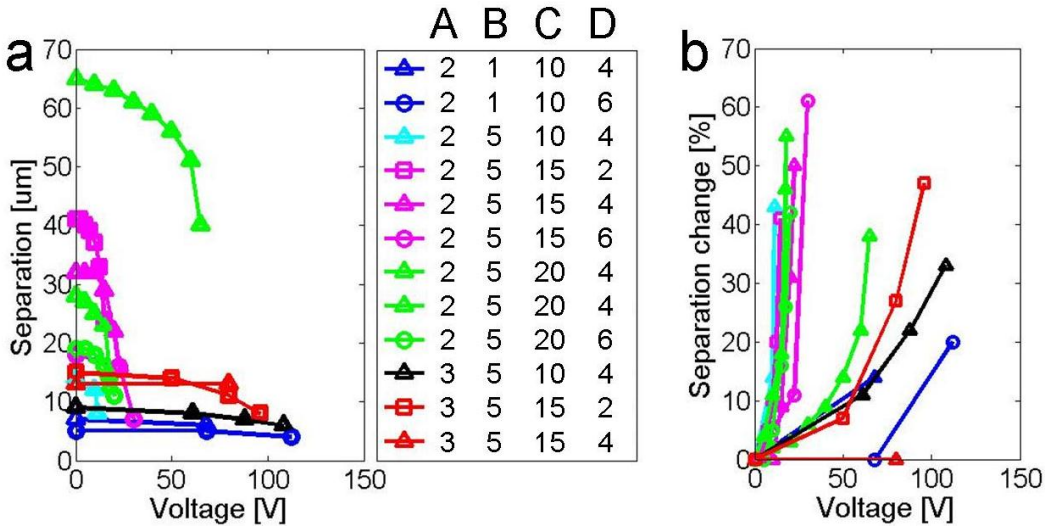

Figure 8.6 a, shows the separation of the nanotube arrays and b, shows the change of the separation, both as a function of applied actuation voltage for different geometries. Column A in the legend refers to the number of support legs, column B refers to the nanotube growth time in minutes, column C refers to the separation of the bottom of the arrays in µm and column D refers to the width of the catalyst pattern in µm.

Each device was designed as two opposing T-shaped electrodes consisting of 10 nm Ti as adhesion layer and 200 nm Mo. These were connected to contact pads in order to enable electrical connection. In contrast to the other chapters, the electrodes were here deposited by sputtering instead of by electron beam evaporation. It was found that this resulted in a resistance one order of magnitude lower than that for the evaporated Mo, which is beneficial for electrical measurements. The electrode area was minimised and shielding electrodes were added in order to reduce the parasitic capacitance and optimise the capacitance measurements [50], see Figure 8.7a and Chapter 3.4 for more information. The catalyst and supporting layer was kept the same, 1 nm Fe and 5 nm Al_2O_3 respectively. The catalyst was deposited at the top of the T-shaped electrodes in an area that was 200 µm long, 4 µm wide and the two areas were separated by 10 µm, unless otherwise stated.

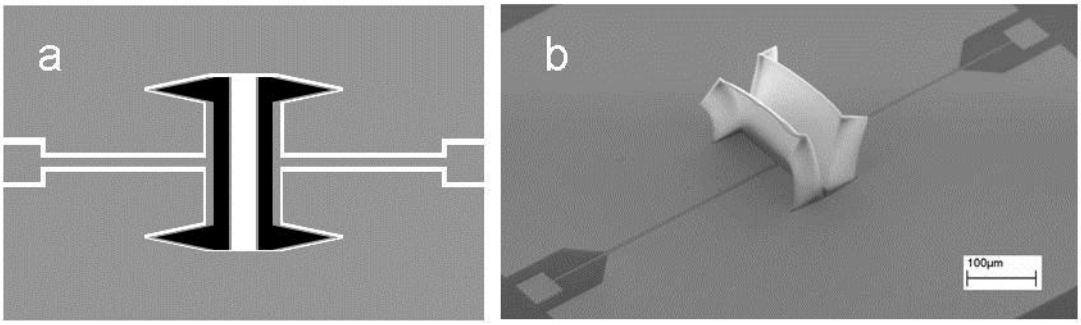

Figure 8.7. a, Schematic of the deposited metal layers. The grey area is where the molybdenum is deposited and the black is where the catalyst is deposited. b, SEM image of a grown structure.

Thermal CVD was used to grow the nanotubes in a quartz furnace at 700 °C, using a gas flow of 5 sccm C_2H_2, 500 sccm H_2 and 500 sccm Ar for 150 s. This resulted in multiwalled nanotubes with a diameter of 5-10 nm and typically 5 walls with a length of 130±5 µm, see Figure 8.7b. The density of the arrays was estimated by measuring the geometry of the device in SEM and by determining the weight of the nanotubes by weighing the sample before and after burning the nanotubes by pyrolysis. The arrays were found to have a density of approximately 10^{10} nanotubes cm^{-2}.

The capacitance between the arrays was measured using a probe station connected to an Agilent 5071B network analyser. The procedure is explained in Chapter 3.4.

8.2 Results

The samples were placed in the same chamber as was used for the local heating growth of carbon nanotubes and videos were recorded of the actuation using the optical microscope. This enabled real time measurements of the actuation. The microscope was focused on the top of the array. Snapshots from one of these videos are shown in Figure 8.8. The resolution is limited in an optical microscope and the depth of field is short, therefore the devices were also actuated inside an SEM in order to increase the resolution and the depth of field, see Figure 8.9. The separation is clearly decreased when a voltage is applied in both cases. The change in separation per change in voltage increases as the applied voltage is raised. Consequently, the actuation response is the highest just below the pull-in voltage, which is the voltage at which the nanotube arrays come into contact with each other. It is interesting to note that even though the nanotube arrays are extremely porous, with only 10^{10} nanotubes cm^{-2} corresponding to a porosity of >95%, they move as a single unit. The brightness of the walls changes as the voltage is increased in the SEM pictures. The lower wall appears darker since it has a positive voltage applied to it, which makes it more difficult for secondary electrons to escape. Since the image in a SEM is generated by these secondary electrons the image will look darker where there only are a few electrons and brighter where there are many electrons. Krupke *et al.* have shown a similar effect [137].

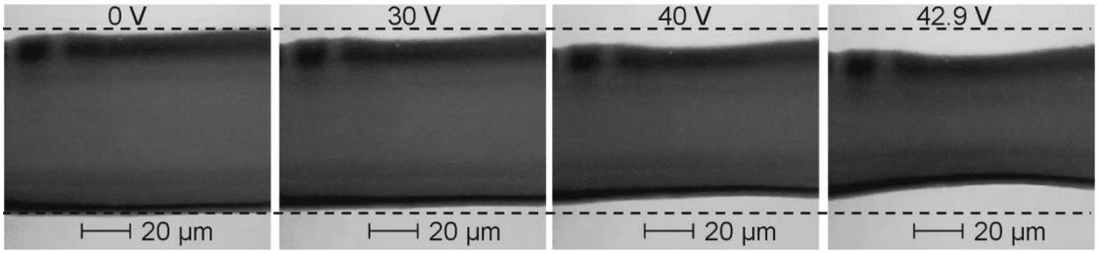

Figure 8.8. Snapshots from a video recorded by an optical microscope focused on the top of the arrays showing how the nanotube arrays are pulled together when the actuation voltage is increased. The applied voltage is listed above each snapshot and the horizontal dashed lines are there to help the eye follow the initial separation of the arrays. The actuation per volt is seen to increase as the voltage increases.

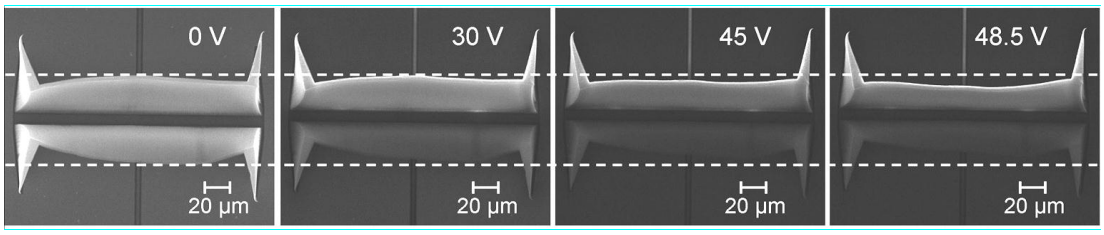

Figure 8.9. SEM images of arrays actuated at the voltages shown in the top of each image. The horizontal dashed lines help to guide the eye to where the arrays were located without any applied actuation voltage. The actuation per volt is seen to increase as the voltage increases. The lower array looks darker as the applied actuation voltage is increased due to the applied positive voltage draining the array of electrons.

Small fluctuations in the growth conditions can yield different final geometries of the arrays, even for otherwise identical cases. Consequently, the voltages required for actuation are different for different devices. This can be seen in Figure 8.10, where the actuation in SEM seems different compared to under the optical microscope. This is a consequence of different initial separations of the nanotube arrays and not a feature of the different techniques. The nanotubes also tend to lean away from each other, resulting in a larger effective separation between the arrays than that of the patterned catalyst. It should, however, be possible to solve this by optimising the growth conditions.

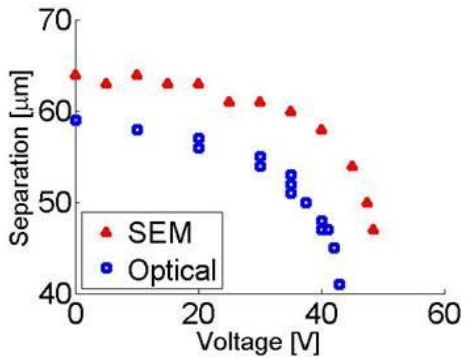

Figure 8.10. Separation as a function of applied actuation voltage for a device actuated in SEM and another device actuated under an optical microscope. The difference between these is not due to the different monitoring techniques but due to different initial separations of the nanotube arrays.

The actuation is reproducible for many cycles as long as the voltage stays below the pull-in voltage. Figure 8.11 shows an example of a device that was cycled 15 times without any sign of degradation. The actuation voltage could instantaneously be changed between 0

V and a voltage just below the pull-in voltage resulting in the same actuation as for a slow actuation, see right part of Figure 8.11. When the pull-in voltage is reached, a current starts flowing between the arrays, which leads to destruction of the nanotubes, see Figure 8.12. This happens when the gap is reduced to approximately 2/3 of the initial separation, which also Desquesnes *et al*. found for MEMS switches [138]. Mainly the middle part of the array is damaged, since this is where the actuation is greatest.

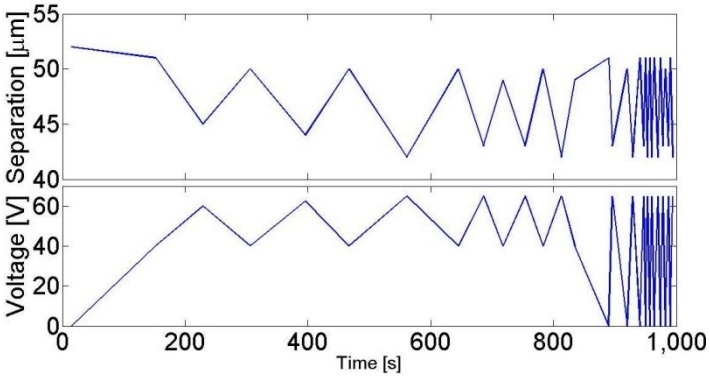

Figure 8.11. The top of the image shows the separation between the nanotube arrays as a function of time and the bottom shows the applied actuation voltage. The graph show that the actuation is reproducible over the 15 cycles.

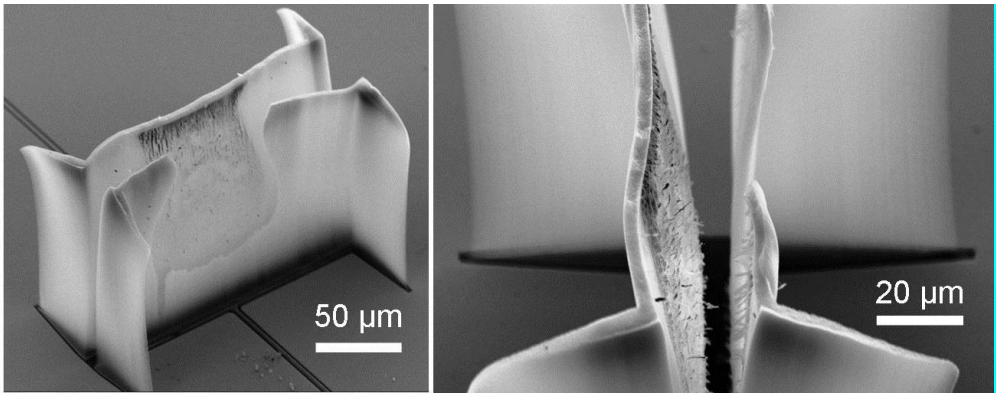

Figure 8.12. SEM images of a device after the pull-in voltage has been reached. A large part of the array on the right side has been destroyed. Some parts of the nanotubes from the destroyed part can be seen deposited on the array on the left side.

Simulations were made on a structure with the same layout as the experimental devices, with the same density, height (135 µm) and width (4 µm) of the arrays and with a separation of 10 µm at the bottom and 60 µm at the top. The arrays were not modelled as an array of nanotubes, but as a block of a metal with similar density. The simulated separation

as a function of applied voltage is plotted in Figure 8.13 for four different values of the Young's modulus. The simulations also predicted the pull-in to be reached when the initial separation had decreased to 67%.

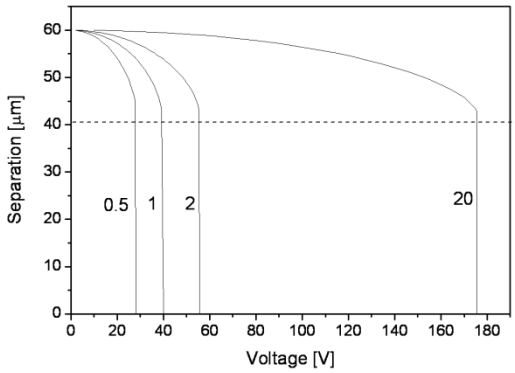

Figure 8.13. Simulations of the actuation of a device showing the separation at the top of the nanotube arrays assuming an initial separation of 60 µm at the top and 10 µm at the bottom. This is shown for four different values of the Young's modulus, 0.5, 1, 2 and 20 MPa. As expected the pull-in voltage scales with the square root of the Young's modulus. The dashed line show a separation of 67% where pull-in is expected to occur.

The Young's moduli of MWCNTs are in the range from 10-50 GPa for catalytically grown nanotubes with a lot of defects to about 800 GPa for high quality arc-discharge grown nanotubes [3]. Young's moduli higher than 1 TPa have been reported by measuring the nanotube vibrations in TEM [139]. It is therefore expected that the nanotubes here have a Young's modulus in between these extremes. At a given voltage, the displacement at the top of the nanotubes scales with $1/\sqrt{(E)}$, where E is the Young's modulus [140]. If the arrays of nanotubes used here had a Young's modulus equivalent to that of individual multiwalled nanotubes, the pull-in voltage would be in the range 3.9-35 kV, which is orders of magnitude higher than the tens of volts found here. The arrays consequently have a significantly lower effective Young's modulus. The reason for this is that the arrays have a low density and the nanotubes are far from being straight but are rather intertwined in each other, see Figure 8.14, making it easy for the nanotubes to slide against each other and thereby forming a material with a low effective Young's modulus.

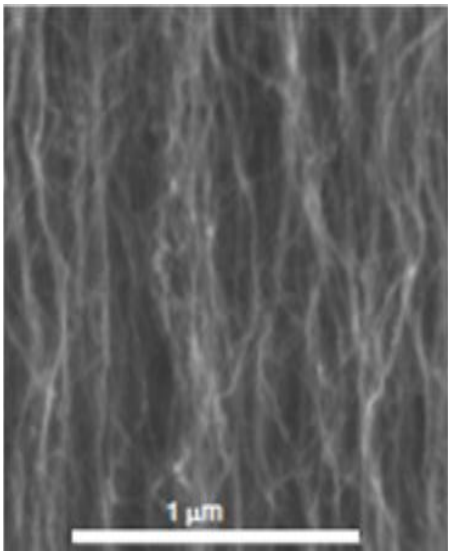

Figure 8.14. SEM image showing the low density and curly nature of the nanotube array.

The separation at the top of the arrays as a function of the applied voltage is plotted in Figure 8.15. This can be used to estimate the Young's modulus. The line in Figure 8.15 is a fit using the Young's modulus as a fitting parameter. This gives a Young's modulus of 3.8 MPa. Hayamizu *et al.* fabricated devices from densified nanotube films and found a Young's modulus of about 10 GPa. The densification increased the density to about 42% [141] which is significantly higher than what is studied here. Nanotube yarns also have a much higher Young's modulus than these devices. Zhang *et al.* have reported values of about 150-460 MPa [142]. Cao *et al.* have reported elastic moduli of about 6 MPa for compressive films, which are more similar to our structures [130].

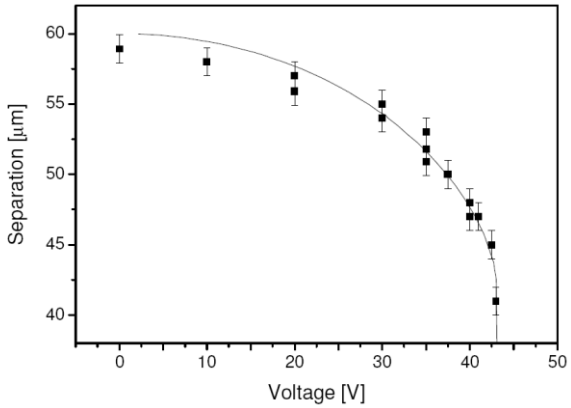

Figure 8.15. Measured separation at the top of the arrays plotted against the applied voltage. The line shows the results from a simulation using a Young's modulus of 3.8 MPa.

8.2.1 Capacitance measurements

The capacitance was measured using the method discussed in chapter 3.4. The S-parameters were first measured at selected actuation voltages by application of high frequency signals and measurements of the transmission and reflection signals. The system was modelled by the equivalent circuit shown in Figure 8.16, where the capacitances and resistances were used as fitting parameters when comparing the response of the model with the high frequency measurements.

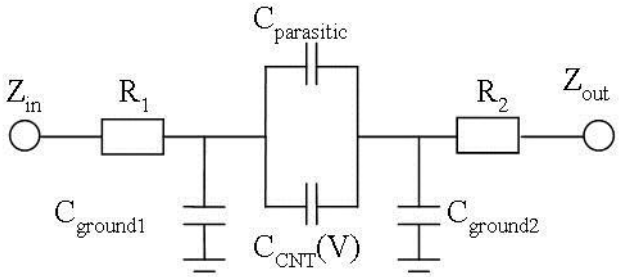

Figure 8.16. The equivalent electrical circuit used to model the devices. $C_{CNT}(V)$ is the active varactor device, the capacitance between the nanotube arrays. R_1 and R_2 are the resistances of the transmission lines, $C_{ground1}$ and $C_{ground2}$ are capacitances to the grounded side electrodes and $C_{parasitic}$ is the capacitance between the electrodes which the nanotubes are grown on.

The capacitances $C_{ground1}$ and $C_{ground2}$ were found by measurements on an OPEN sample. The sample had been exposed to growth conditions but had no catalyst in order to not grow any nanotubes so that the capacitances inherent to the geometry of the device could be extracted. These were found by looking at the Smith chart, see Figure 8.17, where the impedance, *Z*, can be extracted for every frequency, *f*. It can be seen that the reflected signal, S22, behaves as for a pure capacitance, which is expected for our devices. The S21 response is found in the centre of the chart, showing a good matching to the 50 Ω system. More information about basic S-parameter theory and how to use a Smith chart can for example be found from the Agilent Technologies homepage and their handbook [49].

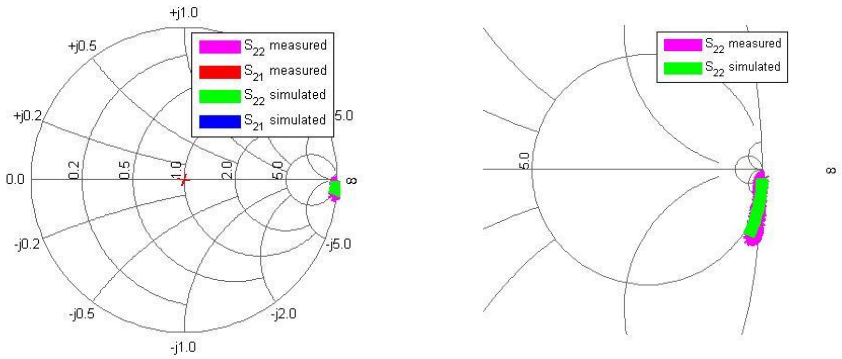

Figure 8.17. Smith chart of the S21 and S22 responses for a device without any nanotubes (OPEN), which is used to determine the capacitance inherent to the geometry of the device.

The capacitances to the shields can be calculated from the impedances found for different frequencies in the Smith chart since the impedance for a purely capacitive circuit is equal to;

$$Z_C = 1/j\omega C = 1/j2\pi fC, \qquad 8.2$$

where ω is the angular frequency. Rearranging this gives that the capacitance is equal to C = 1/(2πf Im(Z)) which gives a value of 110 fF. The transmission coefficient S21 of the S-parameters was measured on a THRU sample, which is a sample with a wire connecting the two T-shapes. These samples had also been exposed to growth conditions but without catalysts. This system was modelled using the equivalent circuit shown in Figure 3.11 and Figure 8.16, but without the capacitance from the nanotubes and including a line bypassing the parasitic capacitance. This resulted in insertion losses of 14 dB, which were modelled by the two resistances R1=R2=190 Ω. The capacitance between the electrodes, $C_{parasitic}$, was then used as a fitting parameter for the S21 response for an OPEN structure and was found to be 5.8 fF. The capacitance between the arrays of nanotubes at selected applied voltages was then used as a fitting parameter in the same way on a real device.

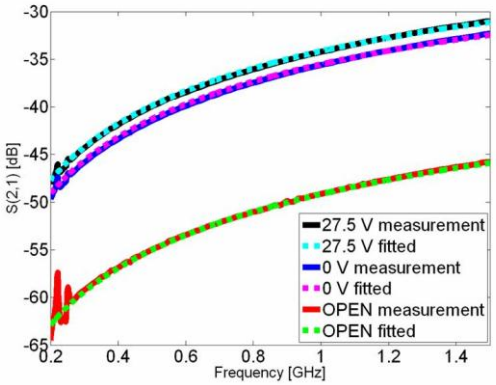

Figure 8.18. Measured and fitted S21 responses for the device at 0 V and 27.5 V, which is just below the pull-in voltage, together with the response for an OPEN device without any nanotubes.

Figure 8.18 shows the S21 response for an OPEN device together with a real device with 0 V and 27.5 V DC bias applied. The model fits the measurements very well for all cases, indicating that the model describes the system accurately. Fitting the capacitance at 0 V yielded a value of 22 fF, which gradually was increased to 27 fF at 27.5 V. This was just below the pull-in voltage and resulted in a capacitance change of more than 20 %. The capacitance could reproducibly be varied below this voltage, see Figure 8.19. The voltage was increased over this voltage after a few cycles to see the change in capacitance. As expected the capacitance dropped since the nanotubes were permanently damaged, see Figure 8.12. It can also be seen that when the voltage was increased further, the capacitance dropped since more and more nanotubes were destroyed. Even if the structure has been damaged, the capacitance can still be varied by changing the actuation voltage. The absolute value of the capacitance is then reduced and a higher actuation voltage is required to reach the same capacitance value as before. The final capacitance is lower than the initial capacitance at 0 V, which also shows that the structure was damaged.

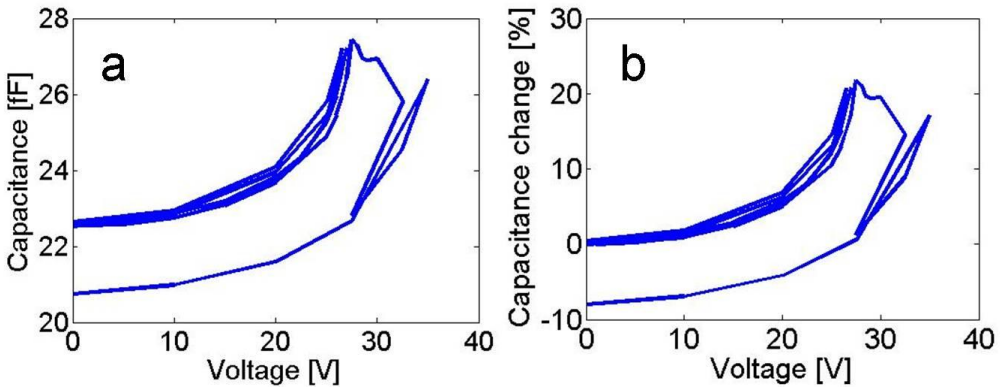

Figure 8.19. a, shows the capacitance versus actuation voltage and b, the change of capacitance compared to the starting value versus the applied voltage. The capacitance can reproducibly be varied below the pull-in voltage. The capacitance can still be reproducibly varied after the pull-in voltage has been reached but at higher actuation voltages and lower capacitances.

The absolute capacitance of the device can be increased in a few different ways. The separation between the arrays can be decreased, but this makes the alignment more crucial. The effective area of the arrays can also be increased in order to increase the absolute capacitance. This can be done by either increasing the length of the nanotubes or the length of the array. Increasing the length of the nanotubes make the alignment more difficult, therefore the length of the arrays was here increased. In Figure 8.20 it can be seen that by doubling the length of the array the capacitance is also doubled, which is expected from Equation 8.1.

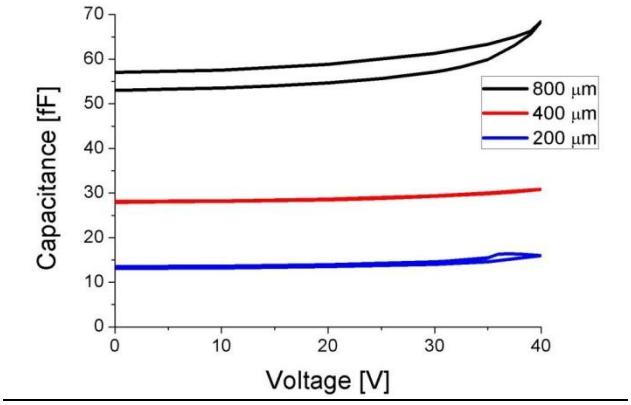

Figure 8.20. The capacitance as a function of applied voltage for devices with different lengths but otherwise identical parameters. The capacitance can be seen to change linearly with the length of the nanotube arrays.

The Q factor or the quality factor can be calculated by the ratio of the reactance (the imaginary part of the impedance), *X*, to the resistance (the real part of the impedance), *R*;

$$Q = \left| \frac{X}{R} \right| = 1/(2\pi f R C), \qquad 8.3$$

where *R* is the resistance and *C* is the capacitance for a frequency *f*. This is plotted both without actuation (0 V) and actuated (27.5 V) in Figure 8.21 in the frequency range 0.2-1.5 GHz. It can be seen that the Q factor decreases from 100 to 10 as the frequency increases. The losses are dominated by the relatively poor conductivity of the Mo electrodes.

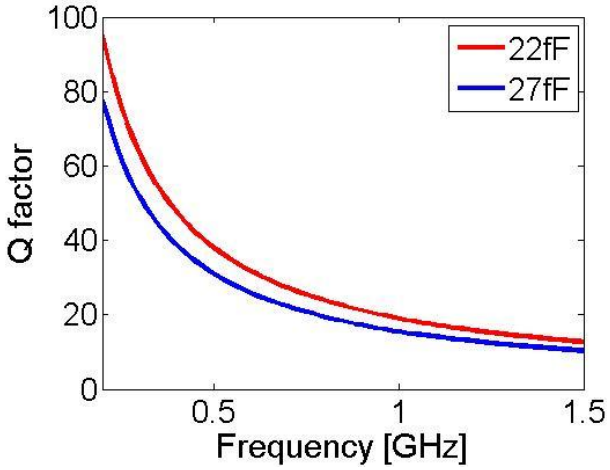

Figure 8.21. The Q factor as a function of the RF frequency. The upper red line is for a device before actuation with a capacitance of 22 fF, whereas the lower blue line is for an actuated device with a capacitance of 27 fF.

8.3 Outlook

Similar devices have been reported after these experiments were done [143]. These structures are very similar but the nanotubes are much shorter, 64 µm and 74 µm compared to 130 µm here, and with a significantly higher density, 8±2 x 10^{11} CNTs/cm^2, which is almost two orders of magnitude higher than here. The Young's modulus was estimated to be in the range of 30-100 MPa. This is much higher than the ~4 MPa found here, which can be expected from the higher density. In order to increase the capacitance, the arrays of nanotubes were interleaved to create several devices in parallel, see Figure 8.22.

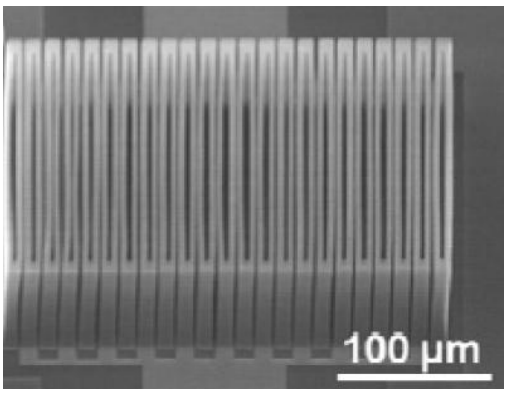

Figure 8.22. A varactor device used in ref. [143] designed as several interleaved fingers in order to increase the capacitance. Adapted from [143].

The high density of nanotubes and the shorter length increased the alignment, but the alignment was a significant problem already for the 74 µm long nanotubes, resulting in unreliable device fabrication. Burning of the nanotubes when the pull-in voltage was reached was avoided by limiting the actuation current to 100 nA. It was mostly not possible to separate the walls again after pull-in was achieved. This is due to strong van der Waals interaction between the membranes. The capacitance was measured using a similar technique to what is reported here. The maximum measured capacitance was 400 fF and the maximum actuation was 5.8 % (for different geometries). The Q factor was found to vary depending on the actual setup but was similar to what was found here.

The varactors can also be made using the local heating growth technique. The varactors are then compatible with standard microelectronics fabrication. However, the alignment was poor in the growth conditions that were studied, see Figure 8.23, but it should be possible to improve this. These structures are significantly smaller than the structures grown using conventional CVD. The capacitance for these structures is therefore significantly lower than for the structures studied above. This could also be optimised by placing the walls closer to each other and by increasing the size of the heater or alternatively placing many in parallel.

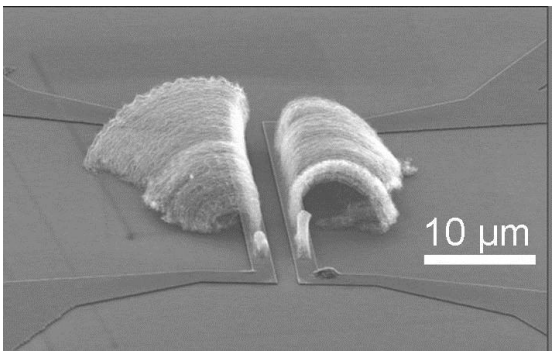

Figure 8.23. SEM image of nanotube arrays grown using the local heating technique. These arrays are too long for any actuation, but it should be possible to make a small varactor device with arrays about half as long.

The actuation of each array was very reproducible. The reproducibility between different devices was however significantly lower, due to differences in the initial separation between the top of the arrays. This results in higher actuation voltages for devices with a greater separation since the electrostatic force depends on the distance between the arrays. Consequently, the reproducibility of the growth of the devices would have to be increased if a real device was to be made.

The fabrication must be improved in order to improve the performance of the varactors, that is to improve the tunability and quality factor, reduce the actuation voltage and increase the capacitance. The capacitance can be increased by placing many walls in parallel, as seen in [143], by increasing the size of the walls, as shown above, or by reducing the separation between them. It is also possible to increase the capacitance by depositing a dielectric layer on the nanotubes [132]. The quality factor can be improved by reducing all resistances in the device. The actuation voltage can be reduced by decreasing the gap between the membranes and the width of them while keeping a good alignment. The alignment can be improved by increasing the density of nanotubes, but this will also increase the Young's modulus and actuation voltage of the devices.

8.4 Conclusions

A varactor was fabricated using two parallel arrays of MWCNTs. The arrays could be actuated by a relatively low bias voltage. By comparing the actuation with model calculations an effective Young's modulus of the nanotube arrays could be estimated. A very low value (about 4 MPa) was found, which allows the relatively large structure to be actuated by relatively low actuation voltages. The capacitances of the device were found by

comparisons between radio frequency measurements and simulations of an equivalent circuit where the capacitance between the nanotubes was used as a fitting parameter. A very good agreement was found between the model and the measurements. A change in capacitance of more than 20 % was achieved. The separation between the arrays, and thereby also the capacitance, could reproducibly be varied below the pull-in voltage, at which point the nanotubes came into contact. The excellent agreement between the model and the measurements makes it possible to design devices for specific operating conditions. The absolute value of the capacitance can, for example, be scaled by changing the dimensions of the nanotube arrays.

It was found that arrays of vertically aligned carbon nanotubes behave as a single unit with a very low Young's modulus and can be used as building blocks for MEMS and NEMS devices. It was also demonstrated that carbon nanotubes can be grown *in situ* on substrates with a layout that permits ultra-sensitive radio-frequency measurements after exposure to standard nanotube growth conditions.

Chapter 9 Conclusions

A local heating method to grow carbon nanotubes has been developed and investigated in this thesis. A small metal (molybdenum) wire is resistively heated, which locally creates temperatures high enough to grow carbon nanotubes. The current through the molybdenum wire is controlled by a LabVIEW program, which also monitors the voltage drop. The growth chamber can be made quite small since no furnace is required. It can therefore also be placed under an optical microscope, which allows *in situ* studies both by optical microscopy and by Raman spectroscopy. Since the high temperatures are very localised on the substrate, nanotubes can be grown directly on the chip without heating the entire chip to high temperatures. The process is therefore compatible with microelectronics processing. In this thesis a relatively small amount of nanotubes was grown during each experiment, but the process can be scaled up by connecting many heaters in parallel, as shown in refs. [34, 40].

In situ studies of the growth process are interesting in order to increase the understanding of how nanotubes are grown and eventually allow selective synthesis of nanotubes with specific and predetermined chirality. This is important in order to take full advantage of the extraordinary properties of carbon nanotubes.

Here, predominantly multi-walled carbon nanotubes grow when acetylene is used as carbon feedstock, whereas mainly single-walled carbon nanotubes grow in an ethylene atmosphere. The multi-walled nanotubes grow vertically in bundles. These bundles are large enough to allow *in situ* studies using optical microscopy. A high growth rate was measured by combining these measurements with *ex situ* SEM. The activation energy was found to be similar to that of standard CVD in otherwise similar conditions. Heaters with a temperature gradient were fabricated in order to study the effect of different temperatures while keeping all other parameters identical. The length of the multi-walled nanotubes gradually increased as the temperature increased. At high temperatures the growth abruptly switched from multi-walled to single-walled nanotube growth. The G/D ratio increased with temperature, indicating that more defective nanotubes are grown at lower temperatures.

The nanotube growth with ethylene as carbon feedstock was investigated by *in situ* Raman spectroscopy using two different modes. In one the nanotube growth was stopped after selected growth times, allowing careful investigation by Raman spectroscopy. Four different laser excitation wavelengths were used to study both the RBM and D-G regions of the Raman spectrum at each time. The G/D ratio was found initially to decrease, indicating

growth of more defective nanotubes and/or deposition of amorphous carbon. The signal from the D peak then decreased, suggesting that the growing nanotubes undergo a self-annealing process. More peaks were found to appear in the RBM region during the growth showing that the nanotube diameter distribution broadens and also appears to shift towards thicker nanotubes. The growth evolution was also studied in real time by *in situ* Raman spectroscopy. The growth could be well described by a growth model using the initial growth rate and the catalyst lifetime as parameters. The growth was found to be limited by mass transfer of carbon. The IV characteristics of the heater were monitored during the growth process. Comparisons of these measurements with the Raman measurements showed that the heater is carbonised before the nanotubes start growing.

Since the gases used here are at room temperature the nanotube growth rate is expected to be low [37]. Despite this, fast growth rates have been measured. This could be due to the carbon first reacting with the molybdenum and forming carbon chains on the heater. Signals indicative of polyyne or cumulene chains have been measured by Raman spectroscopy. The carbon can then be transferred to the catalyst where nanotubes are grown. The heater thus creates an additional pathway for the carbon atoms.

Raman spectra of heated nanotubes were investigated. The nanotubes were heated by the same laser that was used for the Raman measurements. It was found that this could heat the nanotubes to high temperatures. The Raman spectra included a significant background from blackbody radiation. This could be used to estimate the temperature of the nanotubes. The positions of the main peaks in the Raman spectra of carbon nanotubes shift with temperature. This shift was here found to be similar to what has been estimated using other techniques. This shows that it is important to use a low laser power during Raman measurements, as otherwise the peaks shift and a strong blackbody signal can appear. This is especially important for temperature dependent studies where the influence of the Raman laser can be important.

The electromechanical properties of arrays of vertically aligned carbon nanotubes were investigated. The arrays were actuated by a DC bias voltage and were found to behave as a single unit with a very low Young's modulus (similar to that of rubber). This is thought to be because the nanotubes do not grow exactly straight but can easily be stretched and due to that the individual nanotubes in the arrays can slide against each other. The actuation was reproducible over many cycles as long as the actuation voltage was kept below the pull-in voltage. At this voltage the arrays come into contact and irreversibly damage the device. The capacitance between the arrays was extracted by comparing radio frequency measurements

and simulations, where the capacitance between the arrays was kept as a fitting parameter. The model could describe the measurements very well. The capacitance between the arrays could reproducibly be varied by more than 20 % by varying the bias voltage. The absolute value can be scaled by scaling the dimensions and relative position of the arrays.

Bibliography

1. Iijima, S., *Helical microtubules of graphitic carbon.* Nature, 1991. **354**(6348): p. 56-58.
2. Mann, D., et al., *Ballistic Transport in Metallic Nanotubes with Reliable Pd Ohmic Contacts.* Nano Letters, 2003. **3**(11): p. 1541-1544.
3. Salvetat, J.-P., et al., *Elastic Modulus of Ordered and Disordered Multiwalled Carbon Nanotubes.* Advanced Materials, 1999. **11**(2): p. 161-165.
4. Wei, B.Q., R. Vajtai, and P.M. Ajayan, *Reliability and current carrying capacity of carbon nanotubes.* Applied Physics Letters, 2001. **79**(8): p. 1172-1174.
5. Chen, G.Y., et al., *Growth of carbon nanotubes at temperatures compatible with integrated circuit technologies.* Carbon, 2011. **49**(1): p. 280-285.
6. Hofmann, S. and et al., *Controlled low-temperature growth of carbon nanofibres by plasma deposition.* New Journal of Physics, 2003. **5**(1): p. 153.
7. Radushkevich, L.V. and V.M. Lukyanovich, *Structure of the carbon produced in the thermal decomposition of carbon monoxide on an iron catalyst.* Zhurnal Fizicheskoi Khimii, 1952. **26**: p. 88-95.
8. Monthioux, M. and V.L. Kuznetsov, *Who should be given the credit for the discovery of carbon nanotubes?* Carbon, 2006. **44**(9): p. 1621-1623.
9. Iijima, S. and T. Ichihashi, *Single-shell carbon nanotubes of 1-nm diameter.* Nature, 1993. **363**(6430): p. 603-605.
10. Zheng, L.X., et al., *Ultralong single-wall carbon nanotubes.* Nat Mater, 2004. **3**(10): p. 673-676.
11. Hertel, T. [cited; Available from: http://www.phys-chemie.uni-wuerzburg.de/fileadmin/08050200/user_upload/index_explained.jpg.]
12. Reich, S., C. Thomsen, and M. J., *Carbon nanotubes - basic concepts and physical properties*. 2004: Wiley.
13. Saito, R., et al., *Electronic structure of graphene tubules based on C_{60}.* Physical Review B, 1992. **46**(3): p. 1804.
14. Dresselhaus, M.S., et al., *Raman spectroscopy of carbon nanotubes.* Physics Reports, 2005. **409**(2): p. 47-99.
15. Saito, R., et al., *Electronic structure of chiral graphene tubules.* Applied Physics Letters, 1992. **60**(18): p. 2204-2206.
16. Dai, H., *Carbon nanotubes: opportunities and challenges.* Surface Science, 2002. **500**(1-3): p. 218-241.
17. Dresselhaus, M.S., et al., *Electronic, thermal and mechanical properties of carbon nanotubes.* Philosophical Transactions of the Royal Society of London. Series A: Mathematical, Physical and Engineering Sciences, 2004. **362**(1823): p. 2065-2098.
18. Michael, K., *Factors affecting synthesis of single wall carbon nanotubes in arc discharge.* Journal of Physics D: Applied Physics, 2007. **40**(8): p. 2388.
19. Guo, T., et al., *Catalytic growth of single-walled manotubes by laser vaporization.* Chemical Physics Letters, 1995. **243**(1-2): p. 49-54.
20. Vijayaraghavan, A., et al., *Ultra-Large-Scale Directed Assembly of Single-Walled Carbon Nanotube Devices.* Nano Letters, 2007. **7**(6): p. 1556-1560.

21. Baba, A., et al., *Micro/nanopatterning of single-walled carbon nanotube-organic semiconductor composites.* Nanotechnology, 2009. **20**(8): p. 085301.
22. Choi, G.S., et al., *Mass production of carbon nanotubes using spin-coating of nanoparticles.* Microelectronic Engineering, 2003. **66**(1-4): p. 77-82.
23. Lee, S., et al., *Hot-filament CVD synthesis and application of carbon nanostructures.* Thin Solid Films, 2008. **516**(5): p. 700-705.
24. Taki, Y., et al., *Selective Growth of Vertically Aligned Single-, Double-, and Triple-Walled Carbon Nanotubes by Radiation-Heated Chemical Vapor Deposition Radiation-heated CVD (RHCVD).* Japanese Journal of Applied Physics, 2008. **47**(1): p. 721–724.
25. Taki, Y., et al., *Selective Growth of Single-, Double-, and Triple-Walled Carbon Nanotubes through Precise Control of Catalyst Diameter by Radiation-Heated Chemical Vapor Deposition.* Japanese Journal of Applied Physics, 2008. **47**(1): p. 725–729.
26. Haluscaronka, M., Y. Bellouard, and A. Dietzel, *Time dependent growth of vertically aligned carbon nanotube forest using a laser activated catalytical CVD method.* physica status solidi (b), 2008. **245**(10): p. 1927-1930.
27. Cantoro, M., et al., *Effects of pre-treatment and plasma enhancement on chemical vapor deposition of carbon nanotubes from ultra-thin catalyst films.* Diamond and Related Materials, 2006. **15**(4-8): p. 1029-1035.
28. Hofmann, S., et al., *Surface Diffusion: The Low Activation Energy Path for Nanotube Growth.* Physical Review Letters, 2005. **95**(3): p. 036101-4.
29. Wang, Y., et al., *Comparison study of catalyst nanoparticle formation and carbon nanotube growth: Support effect.* Journal of Applied Physics, 2007. **101**(12): p. 124310-8.
30. Lim, S., et al., *Plasma-Assisted Synthesis of Carbon Nanotubes.* Nanoscale Research Letters, 2010. **5**: p. 1377-1386.
31. *ITRS 2008 update*. [cited; Available from: http://www.itrs.net/Links/2008ITRS/Home2008.htm.]
32. Englander, O., D. Christensen, and L. Lin, *Local synthesis of silicon nanowires and carbon nanotubes on microbridges.* Applied Physics Letters, 2003. **82**(26): p. 4797-4799.
33. Kawano, T., et al., *Formation and characterization of silicon/carbon nanotube/silicon heterojunctions by local synthesis and assembly.* Applied Physics Letters, 2006. **89**(16): p. 163510-3.
34. Jungen, A., et al., *Localized and CMOS compatible growth of carbon nanotubes on a 3 x3 pm2 microheater spot*, in *Trancducers05, The 13th International Conference on Solid-Statc Sensors, Actuators and Microsystems*. 2005: Seoul, Korea.
35. Nagato, K., et al., *Local Synthesis of Tungsten Oxide Nanowires by Current Heating of Designed Micropatterned Wires.* Appl. Phys. Express, 2008. **1**(1).
36. Kim, S.M. and et al., *SWCNT growth on Al/Fe/Mo investigated by in situ mass spectroscopy.* Nanotechnology, 2007. **18**(18): p. 185709.
37. Eres, G., et al., *Molecular Beam-Controlled Nucleation and Growth of Vertically Aligned Single-Wall Carbon Nanotube Arrays.* The Journal of Physical Chemistry B, 2005. **109**(35): p. 16684-16694.

38. Hart, A.J., L. van Laake, and A.H. Slocum, *Desktop Growth of Carbon-Nanotube Monoliths with In Situ Optical Imaging.* Small, 2007. **3**(5): p. 772-777.
39. Mølhave, K., et al., *Epitaxial Integration of Nanowires in Microsystems by Local Micrometer-Scale Vapor-Phase Epitaxy.* Small, 2008. **4**(10): p. 1741-1746.
40. Sunden, E.O., et al., *Room-temperature chemical vapor deposition and mass detection on a heated atomic force microscope cantilever.* Applied Physics Letters, 2006. **88**(3): p. 033107-3.
41. Santra, S., et al., *Post-CMOS wafer level growth of carbon nanotubes for low-cost microsensors - a proof of concept.* Nanotechnology, 2010. **21**(48): p. 485301.
42. Udrea, F., et al. *Three technologies for a smart miniaturized gas-sensor: SOI CMOS, micromachining, and CNTs - challenges and performance*. in *Electron Devices Meeting, 2007. IEDM 2007. IEEE International*. 2007.
43. Engström, D.S., et al., *Vertically aligned CNT growth on a microfabricated silicon heater with integrated temperature control-determination of the activation energy from a continuous thermal gradient.* Journal of Micromechanics and Microengineering, 2011. **21**(1): p. 015004.
44. Ren, Z.F., et al., *Synthesis of Large Arrays of Well-Aligned Carbon Nanotubes on Glass.* Science, 1998. **282**(5391): p. 1105-1107.
45. Sosnowchik, B.D., L. Lin, and O. Englander, *Localized heating induced chemical vapor deposition for one-dimensional nanostructure synthesis.* Journal of Applied Physics, 2010. **107**(5): p. 051101-14.
46. Gamble, H.S., et al., *Low-loss CPW lines on surface stabilized high-resistivity silicon.* Microwave and Guided Wave Letters, IEEE, 1999. **9**(10): p. 395-397.
47. Nordling, C. and J. Österman, *Physics Handbook for Science and Engineering*. 6th ed. 1999, Lund: Studentlitteratur.
48. Christofferson, J., et al. *Microscale and Nanoscale Thermal Characterization Techniques*. in *Thermal Issues in Emerging Technologies: Theory and Application, 2007. THETA 2007. International Conference on*. 2007.
49. Agilent. [cited; Available from: http://eesof.tm.agilent.com/docs/iccap2002/MDLGBOOK/1MEASUREMENTS/3VNA/3SPAR/1SparBasics_1.pdf http://eesof.tm.agilent.com/docs/iccap2002/iccap_mdl_handbook.html.]
50. Eriksson, A., et al., *Direct Transmission Detection of Tunable Mechanical Resonance in an Individual Carbon Nanofiber Relay.* Nano Letters, 2008. **8**(4): p. 1224-1228.
51. Ohring, M., *Materials Science of Thin Films. Deposition and Structure*. 2nd ed. 2002, San Diego: Academic Press.
52. Raman, C.V., *A new radiation.* Indian J. Phys, 1928. **2**.
53. Landsberg, G. and L. Mandelstam, *Eine neue Erscheinung bei der Lichtzerstreuung in Krystallen.* Die Naturwissenschaften, 1928. **16**: p. 557-558.
54. Singh, R. and F. Riess, *The 1930 Nobel Prize for Physics: A close decision?* Notes and Records of the Royal Society of London, 2001. **55**(2): p. 267-283.

55. Maruyama, S. [cited; Available from: http://www.photon.t.u-tokyo.ac.jp/~maruyama/kataura/katauran.pdf.]
56. Saito, R., C. Fantini, and J. Jiang, *Excitonic States and Resonance Raman Spectroscopy of Single-Wall Carbon Nanotubes*, in *Carbon Nanotubes*. 2008, Springer Berlin / Heidelberg. p. 251-286.
57. Fantini, C., et al., *Optical Transition Energies for Carbon Nanotubes from Resonant Raman Spectroscopy: Environment and Temperature Effects.* Physical Review Letters, 2004. **93**(14): p. 147406.
58. Hsieh, Y.-P., et al., *Chiral angle dependence of resonance window widths in (2n + m) families of single-walled carbon nanotubes.* Applied Physics Letters, 2010. **96**(10): p. 103118-3.
59. Jorio, A., et al., *Structural (n, m) Determination of Isolated Single-Wall Carbon Nanotubes by Resonant Raman Scattering.* Physical Review Letters, 2001. **86**(6): p. 1118.
60. Meyer, J.C., et al., *Raman Modes of Index-Identified Freestanding Single-Walled Carbon Nanotubes.* Physical Review Letters, 2005. **95**(21): p. 217401.
61. Milnera, M., et al., *Periodic Resonance Excitation and Intertube Interaction from Quasicontinuous Distributed Helicities in Single-Wall Carbon Nanotubes.* Physical Review Letters, 2000. **84**(6): p. 1324.
62. Park, J.S., et al., *Raman resonance window of single-wall carbon nanotubes.* Physical Review B, 2006. **74**(16): p. 165414.
63. Jorio, A., et al., *G-band resonant Raman study of 62 isolated single-wall carbon nanotubes.* Physical Review B, 2002. **65**(15): p. 155412.
64. Brown, S.D.M., et al., *Origin of the Breit-Wigner-Fano lineshape of the tangential G-band feature of metallic carbon nanotubes.* Physical Review B, 2001. **63**(15): p. 155414.
65. Pimenta, M.A., et al., *Raman modes of metallic carbon nanotubes.* Physical Review B, 1998. **58**(24): p. R16016.
66. Dresselhaus, M.S., A. Jorio, and R. Saito, *Characterizing Graphene, Graphite, and Carbon Nanotubes by Raman Spectroscopy.* Annual Review of Condensed Matter Physics, 2010. **1**(1): p. 89-108.
67. Brown, S.D.M., et al., *Observations of the D-band feature in the Raman spectra of carbon nanotubes.* Physical Review B, 2001. **64**(7): p. 073403.
68. Saito, R. and et al., *Double resonance Raman spectroscopy of single-wall carbon nanotubes.* New Journal of Physics, 2003. **5**(1): p. 157.
69. Maciel, I.O., et al., *Electron and phonon renormalization near charged defects in carbon nanotubes.* Nat Mater, 2008. **7**(11): p. 878-883.
70. Gupta, A., et al., *Raman Scattering from High-Frequency Phonons in Supported n-Graphene Layer Films.* Nano Letters, 2006. **6**(12): p. 2667-2673.
71. de los Arcos, T., et al., *The Influence of Catalyst Chemical State and Morphology on Carbon Nanotube Growth.* The Journal of Physical Chemistry B, 2004. **108**(23): p. 7728-7734.
72. de los Arcos, T., et al., *Strong influence of buffer layer type on carbon nanotube characteristics.* Carbon, 2004. **42**(1): p. 187-190.
73. Börjesson, A., et al., *Computational study of the thermal behavior of iron clusters on a porous substrate.* Physical Review B, 2008. **77**(11): p. 115450.

74. Nerushev, O.A., et al., *Particle size dependence and model for iron-catalyzed growth of carbon nanotubes by thermal chemical vapor deposition.* Journal of Applied Physics, 2003. **93**(7): p. 4185-4190.
75. Dittmer, S., *Development of a Method for Highly Localized Growth of Carbon Nanotubes*, in *Applied Physics*. 2008, Chalmers University of Technology: Gothenburgh.
76. Puretzky, A.A., et al., *In situ measurements and modeling of carbon nanotube array growth kinetics during chemical vapor deposition.* Applied Physics A: Materials Science & Processing, 2005. **81**(2): p. 223-240.
77. Wang, X., et al., *Fabrication of Ultralong and Electrically Uniform Single-Walled Carbon Nanotubes on Clean Substrates.* Nano Letters, 2009. **9**(9): p. 3137-3141.
78. Kim, K.-E., et al., *Investigation on the temperature-dependent growth rate of carbon nanotubes using chemical vapor deposition of ferrocene and acetylene.* Chemical Physics Letters, 2005. **401**(4-6): p. 459-464.
79. Liu, K., et al., *A growth mark method for studying growth mechanism of carbon nanotube arrays.* Carbon, 2005. **43**(14): p. 2850-2856.
80. Vinten, P., et al., *Origin of periodic rippling during chemical vapor deposition growth of carbon nanotube forests.* Carbon, 2011. **In Press, Corrected Proof**.
81. Zhang, Q., et al., *Synchronous Growth of Vertically Aligned Carbon Nanotubes with Pristine Stress in the Heterogeneous Catalysis Process.* The Journal of Physical Chemistry C, 2007. **111**(40): p. 14638-14643.
82. Zhang, Y., et al., *Ethanol-Promoted High-Yield Growth of Few-Walled Carbon Nanotubes.* The Journal of Physical Chemistry C, 2010. **114**(14): p. 6389-6395.
83. Zhang, Y., et al., *Tailoring the Morphology of Carbon Nanotube Arrays: From Spinnable Forests to Undulating Foams.* ACS Nano, 2009. **3**(8): p. 2157-2162.
84. Nerushev, O.A., et al., *The temperature dependence of Fe-catalysed growth of carbon nanotubes on silicon substrates.* Physica B: Condensed Matter, 2002. **323**(1-4): p. 51-59.
85. Geohegan, D.B., et al., *In situ time-resolved measurements of carbon nanotube and nanohorn growth.* physica status solidi (b), 2007. **244**(11): p. 3944-3949.
86. Wood, R.F., et al., *Simple model of the interrelation between single- and multiwall carbon nanotube growth rates for the CVD process.* Physical Review B, 2007. **75**(23): p. 235446.
87. Ding, F., K. Bolton, and A. Rosen, *Iron-carbide cluster thermal dynamics for catalyzed carbon nanotube growth.* Journal of Vacuum Science & Technology A: Vacuum, Surfaces, and Films, 2004. **22**(4): p. 1471-1476.
88. Harutyunyan, A.R., et al., *Hidden features of the catalyst nanoparticles favorable for single-walled carbon nanotube growth.* Applied Physics Letters, 2007. **90**(16): p. 163120-3.
89. Cheung, C.L., et al., *Diameter-Controlled Synthesis of Carbon Nanotubes.* The Journal of Physical Chemistry B, 2002. **106**(10): p. 2429-2433.

90. In, J.B., et al., *Hidden role of trace gas impurities in chemical vapor deposition growth of vertically-aligned carbon nanotube arrays.* Applied Physics Letters, 2011. **98**(15): p. 153102-3.
91. Abed, H., et al., *Directed growth of horizontal silicon nanowires by laser induced decomposition of silane.* Journal of Vacuum Science & Technology B: Microelectronics and Nanometer Structures, 2006. **24**(3): p. 1248-1253.
92. Haluška, M., Y. Bellouard, and A. Dietzel, *Time dependent growth of vertically aligned carbon nanotube forest using a laser activated catalytical CVD method.* physica status solidi (b), 2008. **245**(10): p. 1927-1930.
93. Park, J.B. and et al., *The rapid growth of vertically aligned carbon nanotubes using laser heating.* Nanotechnology, 2009. **20**(18): p. 185604.
94. Shi, J., et al., *Direct synthesis of single-walled carbon nanotubes bridging metal electrodes by laser-assisted chemical vapor deposition.* Applied Physics Letters, 2006. **89**(8): p. 083105.
95. Arnold, M.S., et al., *Sorting carbon nanotubes by electronic structure using density differentiation.* Nat Nano, 2006. **1**(1): p. 60-65.
96. Dittmer, S., et al., *Growth of Aligned MWNT Arrays Using a Micrometer Scale Local-Heater at Low Ambient Temperature.* Journal of Nanoscience and Nanotechnology, 2010. **10**(6): p. 4015-4022.
97. Puretzky, A.A. and et al., *Real-time imaging of vertically aligned carbon nanotube array growth kinetics.* Nanotechnology, 2008. **19**(5): p. 055605.
98. Einarsson, E., et al., *Growth dynamics of vertically aligned single-walled carbon nanotubes from in situ measurements.* Carbon, 2008. **46**(6): p. 923-930.
99. Jönsson, M. and et al., *In situ growth rate measurements during plasma-enhanced chemical vapour deposition of vertically aligned multiwall carbon nanotube films.* Nanotechnology, 2007. **18**(30): p. 305702.
100. Meshot, E.R., et al., *Engineering Vertically Aligned Carbon Nanotube Growth by Decoupled Thermal Treatment of Precursor and Catalyst.* ACS Nano, 2009. **3**(9): p. 2477-2486.
101. Yoshida, H., et al., *Atomic-Scale In-situ Observation of Carbon Nanotube Growth from Solid State Iron Carbide Nanoparticles.* Nano Letters, 2008. **8**(7): p. 2082-2086.
102. Sharma, R. and Z. Iqbal, *In situ observations of carbon nanotube formation using environmental transmission electron microscopy.* Applied Physics Letters, 2004. **84**(6): p. 990-992.
103. Helveg, S., et al., *Atomic-scale imaging of carbon nanofibre growth.* Nature, 2004. **427**(6973): p. 426-429.
104. Dittmer, S., et al., *In situ Raman studies of single-walled carbon nanotubes grown by local catalyst heating.* Chemical Physics Letters, 2008. **457**(1-3): p. 206-210.
105. Finnie, P., A. Li-Pook-Than, and J. Lefebvre, *The Dynamics of the Nucleation, Growth and Termination of Single-Walled Carbon Nanotubes from in situ Raman Spectroscopy During Chemical Vapor Deposition.* Nano Research, 2009. **2**(10): p. 783-792.
106. Kaminska, K., et al., *Real-time in situ Raman imaging of carbon nanotube growth.* Nanotechnology, 2007. **18**(16).

107. Li-Pook-Than, A., J. Lefebvre, and P. Finnie, *Phases of Carbon Nanotube Growth and Population Evolution from in Situ Raman Spectroscopy during Chemical Vapor Deposition.* The Journal of Physical Chemistry C, 2010. **114**(25): p. 11018-11025.
108. Picher, M., et al., *Self-Deactivation of Single-Walled Carbon Nanotube Growth Studied by in Situ Raman Measurements.* Nano Letters, 2009. **9**(2): p. 542-547.
109. Picher, M., E. Anglaret, and V. Jourdain, *High temperature activation and deactivation of single-walled carbon nanotube growth investigated by in situ Raman measurements.* Diamond and Related Materials, 2010. **19**(5-6): p. 581-585.
110. Futaba, D.N., et al., *Kinetics of Water-Assisted Single-Walled Carbon Nanotube Synthesis Revealed by a Time-Evolution Analysis.* Physical Review Letters, 2005. **95**(5): p. 056104.
111. Kobayashi, Y., et al., *Extremely intense Raman signals from single-walled carbon nanotubes suspended between Si nanopillars.* Chemical Physics Letters, 2004. **386**(1-3): p. 153-157.
112. Wang, L. and W.T. Tysoe, *The structural properties and thermal decomposition pathways for ethylene adsorbed on clean Mo(100).* Surface Science, 1990. **236**(3): p. 325-340.
113. Bartlett, B.F. and W.T. Tysoe, *Molybdenum metal catalyzed reaction of ethylene.* Catalysis Letters, 1997. **44**(1): p. 37-42.
114. Kastner, J., et al., *Reductive Preparation of Carbyne with High Yield. An in Situ Raman Scattering Study.* Macromolecules, 1995. **28**(1): p. 344-353.
115. Lim, S.H., et al., *A molecular quantum wire of linear carbon chains encapsulated within single-walled carbon nanotube (C[sub n]@SWNT).* Journal of Applied Physics, 2011. **109**(1): p. 016108-3.
116. Eres, G., et al., *Model for Self-Assembly of Carbon Nanotubes from Acetylene Based on Real-Time Studies of Vertically Aligned Growth Kinetics.* The Journal of Physical Chemistry C, 2009. **113**(35): p. 15484-15491.
117. Chiashi, S., et al., *Temperature dependence of Raman scattering from single-walled carbon nanotubes: Undefined radial breathing mode peaks at high temperatures.* Japanese Journal of Applied Physics, 2008. **47**(4): p. 2010-2015.
118. Huang, F.M., et al., *Temperature dependence of the Raman spectra of carbon nanotubes.* Journal of Applied Physics, 1998. **84**(7): p. 4022-4024.
119. Puech, P., et al., *Raman G and D band in strongly photoexcited carbon nanotubes.* Physical Review B, 2009. **79**(8): p. 085418.
120. Raravikar, N.R., et al., *Temperature dependence of radial breathing mode Raman frequency of single-walled carbon nanotubes.* Physical Review B, 2002. **66**(23): p. 235424.
121. Graham, A.P., et al., *How do carbon nanotubes fit into the semiconductor roadmap?* Applied Physics A: Materials Science & Processing, 2005. **80**(6): p. 1141-1151.
122. Graham, A.P., et al., *Towards the integration of carbon nanotubes in microelectronics.* Diamond and Related Materials, 2004. **13**(4-8): p. 1296-1300.

123. Robertson, J., *Growth of nanotubes for electronics.* Materials Today, 2007. **10**(1-2): p. 36-43.
124. Avouris, P. and J. Chen, *Nanotube electronics and optoelectronics.* Materials Today, 2006. **9**(10): p. 46-54.
125. Sato, M., et al., *High-Current Reliability of Carbon Nanotube Via Interconnects.* Japanese Journal of Applied Physics, 2010. **49**(10).
126. Haselman, M. and S. Hauck, *The Future of Integrated Circuits: A Survey of Nanoelectronics.* Proceedings of the IEEE, 2010. **98**(1): p. 11-38.
127. Fan, S., et al., *Self-Oriented Regular Arrays of Carbon Nanotubes and Their Field Emission Properties.* Science, 1999. **283**(5401): p. 512-514.
128. Goldoni, A. and et al., *Sensing gases with carbon nanotubes: a review of the actual situation.* Journal of Physics: Condensed Matter, 2010. **22**(1): p. 013001.
129. Aliev, A.E., et al., *Giant-Stroke, Superelastic Carbon Nanotube Aerogel Muscles.* Science, 2009. **323**(5921): p. 1575-1578.
130. Cao, A., et al., *Super-Compressible Foamlike Carbon Nanotube Films.* Science, 2005. **310**(5752): p. 1307-1310.
131. Jang, J.E., et al., *Nanoscale capacitors based on metal-insulator-carbon nanotube-metal structures.* Applied Physics Letters, 2005. **87**(26): p. 263103.
132. Jang, J.E., et al., *Nanoscale memory cell based on a nanoelectromechanical switched capacitor.* Nat Nano, 2008. **3**(1): p. 26-30.
133. Dragoman, D. and M. Dragoman, *Variable capacitance mechanisms in carbon nanotubes.* Journal of Applied Physics, 2007. **101**(3): p. 036111-3.
134. Ghavanini, F.A., et al., *Compatibility Assessment of CVD Growth of Carbon Nanofibers on Bulk CMOS Devices.* Nano Letters, 2008. **8**(8): p. 2437-2441.
135. Isacsson, A. and J.M. Kinaret, *Parametric resonances in electrostatically interacting carbon nanotube arrays.* Physical Review B, 2009. **79**(16): p. 165418.
136. Jeong, G.-H., et al., *Effect of catalyst pattern geometry on the growth of vertically aligned carbon nanotube arrays.* Carbon, 2009. **47**(3): p. 696-704.
137. Vijayaraghavan, A., et al., *Imaging electronic structure of carbon nanotubes by voltage-contrast scanning electron microscopy.* Nano Research, 2008. **1**(4): p. 321-332.
138. Dequesnes, M., S.V. Rotkin, and N.R. Aluru, *Calculation of pull-in voltages for carbon-nanotube-based nanoelectromechanical switches.* Nanotechnology, 2002. **13**(1): p. 120.
139. Krishnan, A., et al., *Young's modulus of single-walled nanotubes.* Physical Review B, 1998. **58**(20): p. 14013.
140. Landau, L.D. and E.M. Lifschitz, *Theory of Elasticity*. 2nd ed. 1981: Oxford: Pergamon.
141. Hayamizu, Y., et al., *Integrated three-dimensional microelectromechanical devices from processable carbon nanotube wafers.* Nat Nano, 2008. **3**(5): p. 289-294.
142. Zhang, M., K.R. Atkinson, and R.H. Baughman, *Multifunctional Carbon Nanotube Yarns by Downsizing an Ancient Technology.* Science, 2004. **306**(5700): p. 1358-1361.
143. Arun, A., et al., *Tunable MEMS capacitors using vertical carbon nanotube arrays grown on metal lines.* Nanotechnology, 2011. **22**(2): p. 025203.

Appendix A Sample fabrication steps

Processing steps for local heater sample fabrication:

Spin coat LOR 3A – 3000 rpm for 60 s (3000 ms ramp up and down)

(Use 2000 rpm for thicker layers)

Bake 180 °C for 5 min.

Spin UV 5 – 3000 rpm for 60 s (3000 ms ramp up and down)

Bake 130 °C for 90 s.

Electron beam exposure

Postbake 130 °C for 90 s.

Develop 45 s in MF24A (increase time if necessary)

Rinse in water

Ash 30 s at 50 W just before deposition

Deposit materials (electron beam evaporation or sputtering)

1165 remover, heat two baths to <85 °C, ultrasonicate if necessary

Rinse in acetone

and IPA

Appendix B *In situ* studies

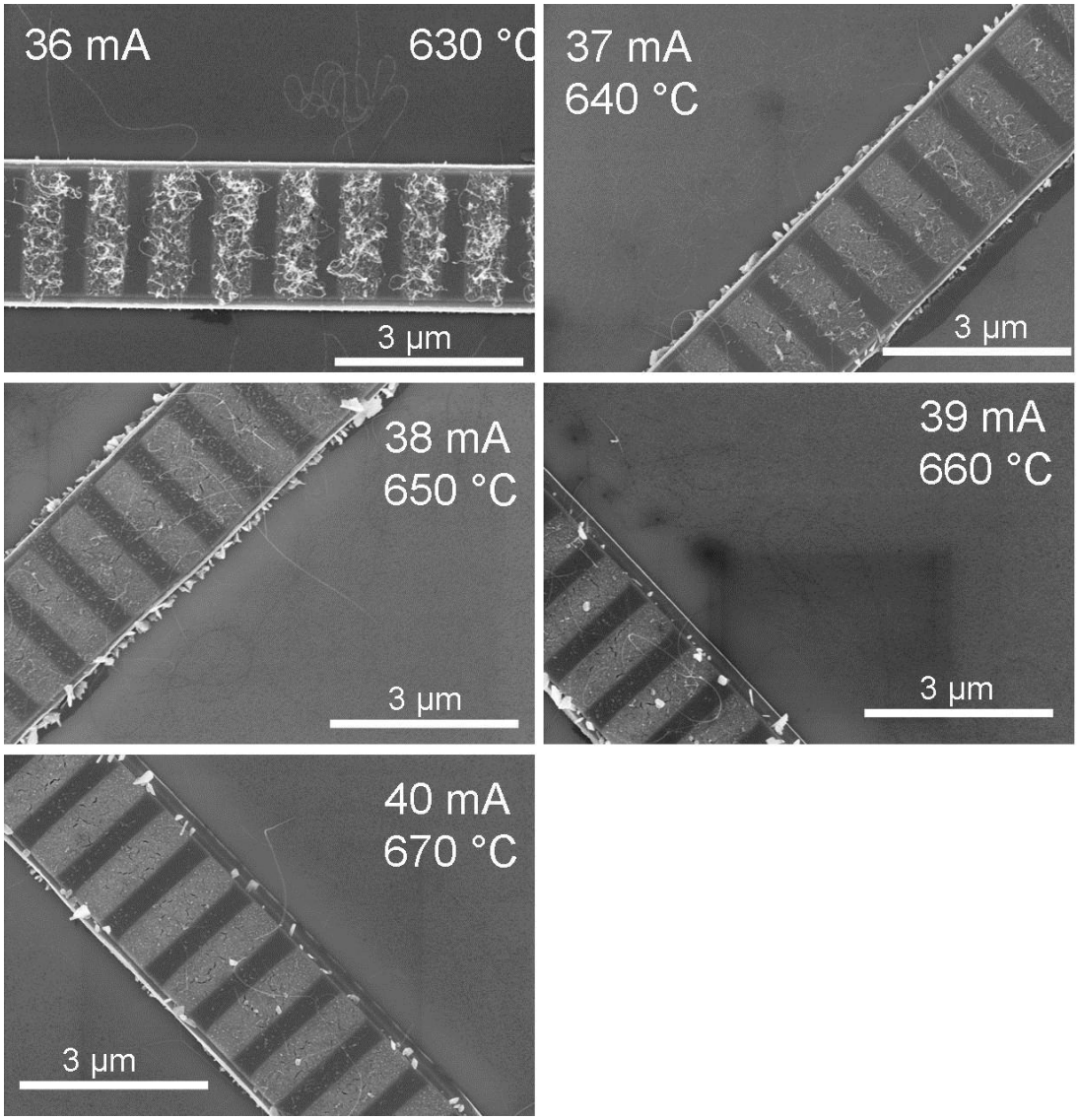

Figure B.1. SEM images of nanotubes grown using 6 sccm of ethylene at different temperatures, as shown on the images.

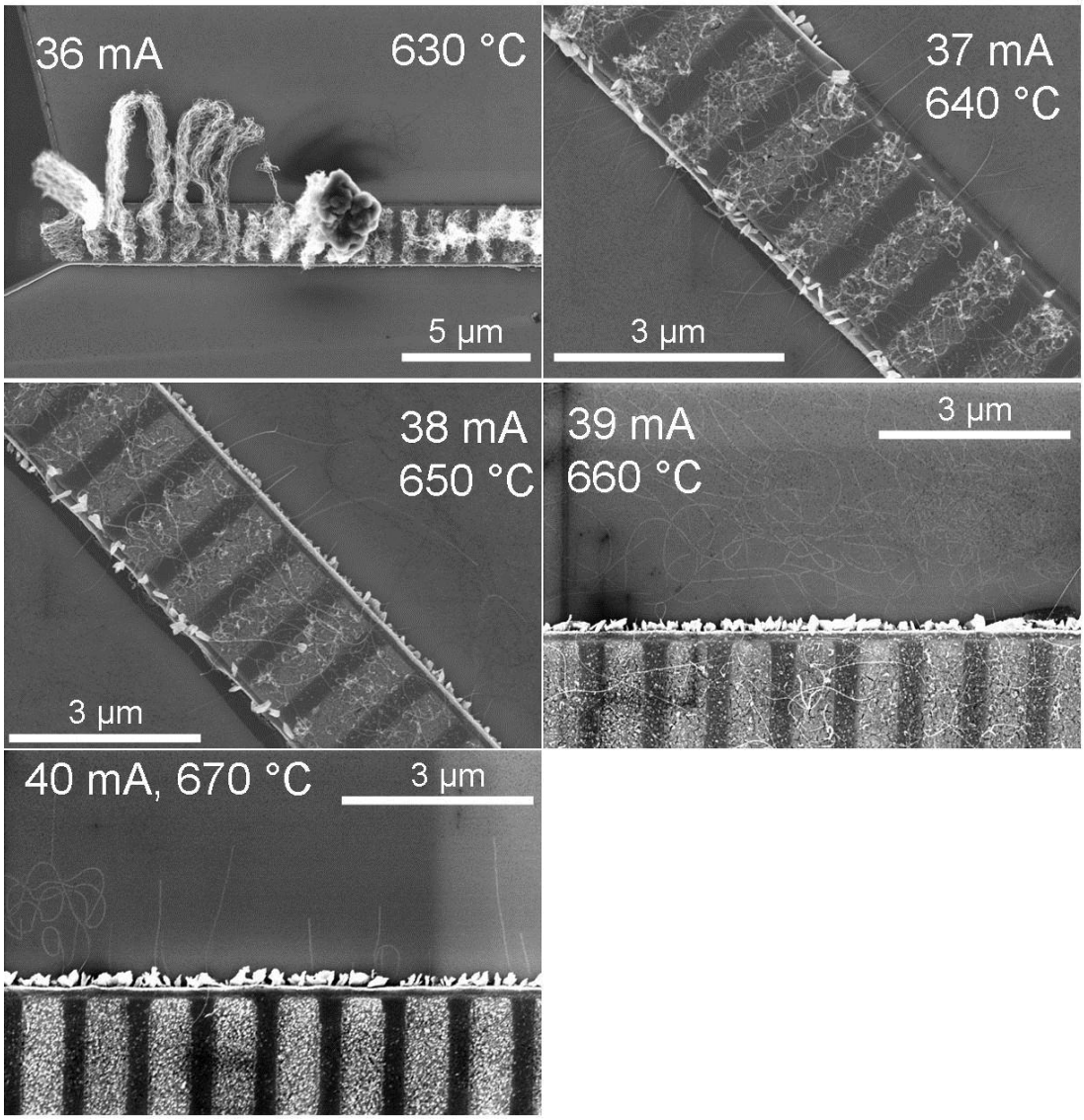

Figure B.2. SEM images of nanotubes grown using 30 sccm of ethylene at different temperatures, as shown on the images.

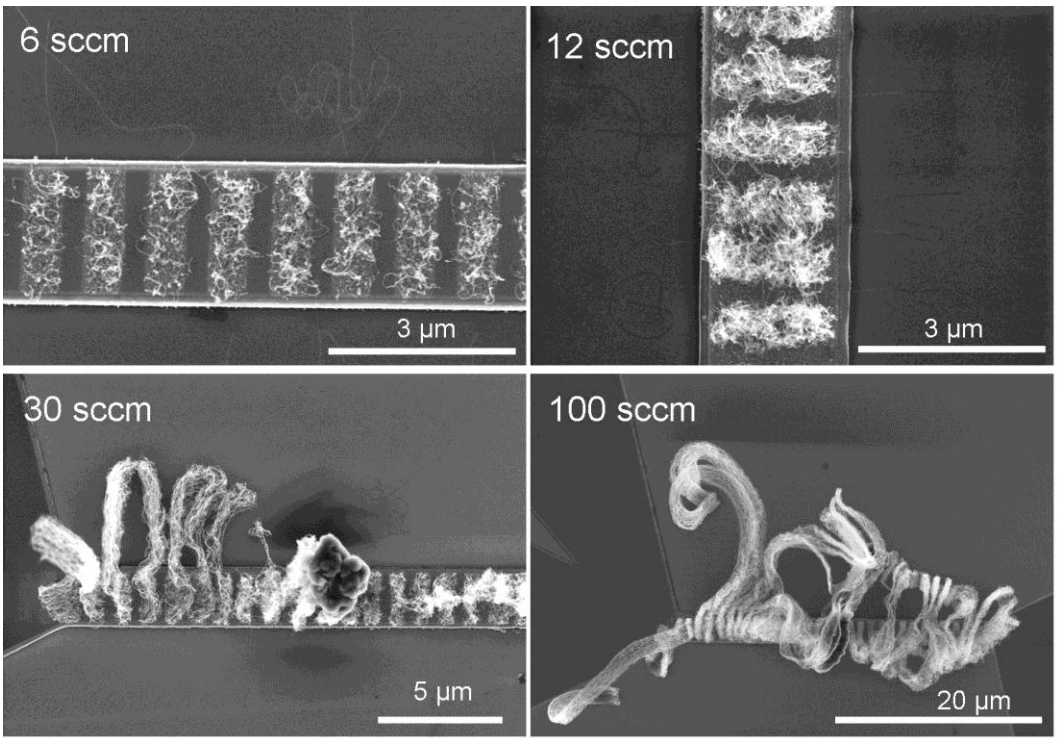

Figure B.3. SEM images of nanotubes grown at 630 °C for different ethylene flow rates, as shown on the different images.

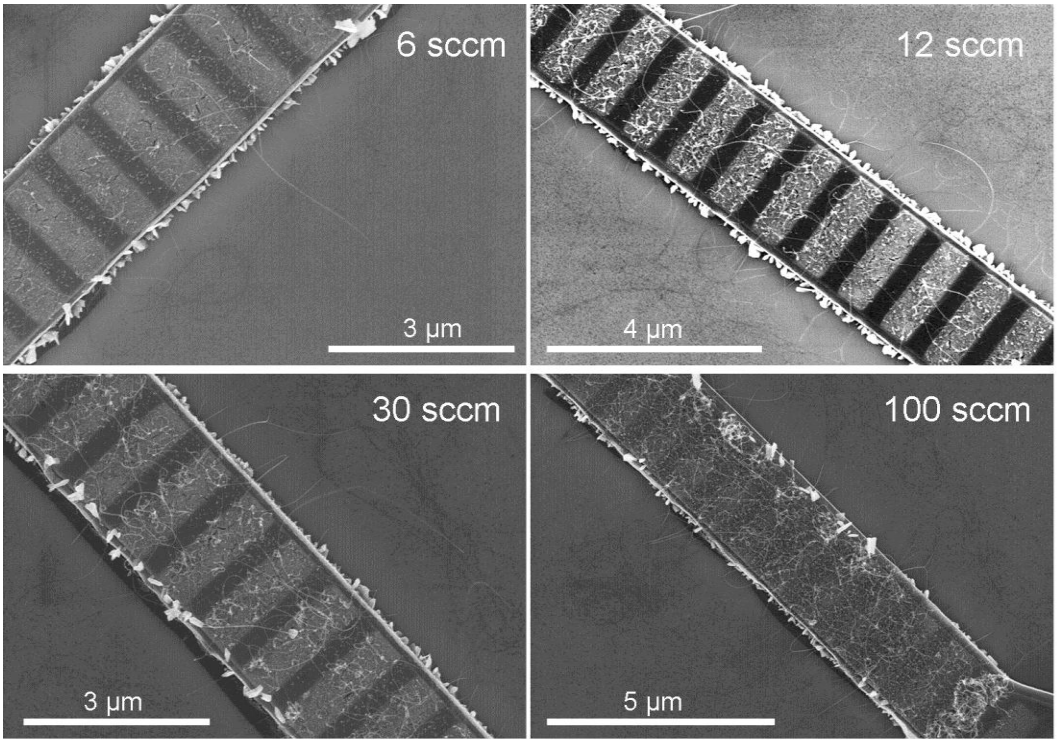

Figure B.4. SEM images of nanotubes grown at 650 °C for different ethylene flow rates, as shown on the different images.

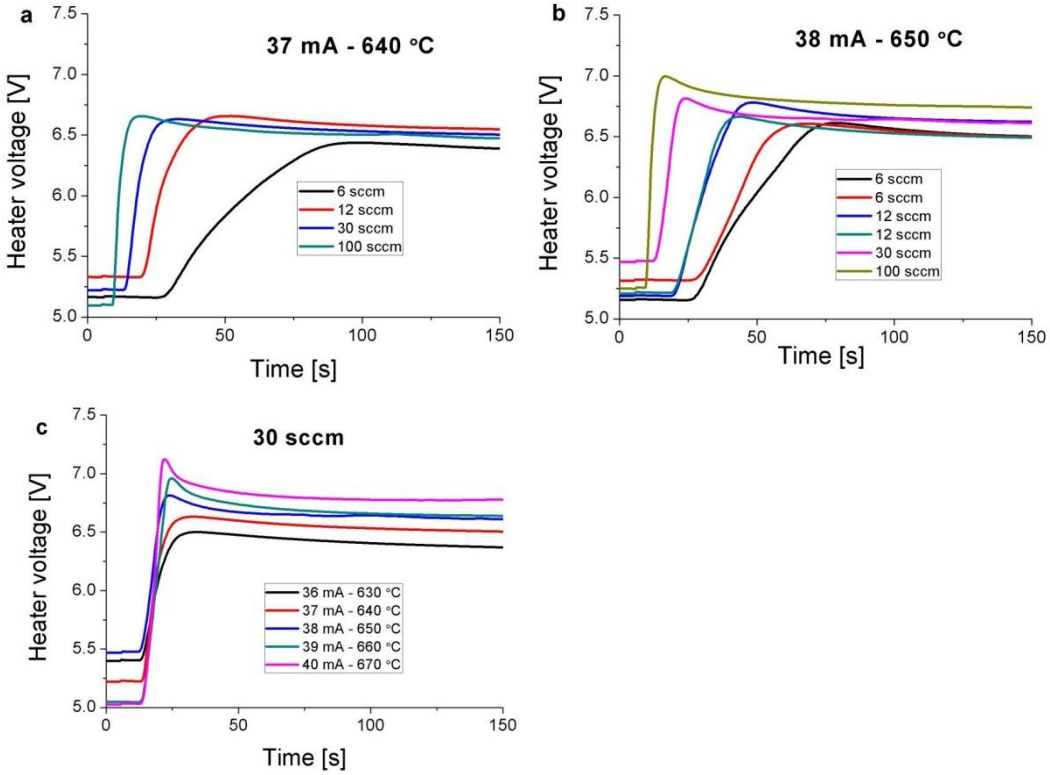

Figure B.5. Zoomed in images of the voltage drop across the heater just after the ethylene has been started. a, and b, show the effect of different carbon flow rates at a constant temperature (640 °C and 650 °C respectively), whereas c, shows the voltage drop for the same ethylene flow rate (30 sccm) but at different temperatures.

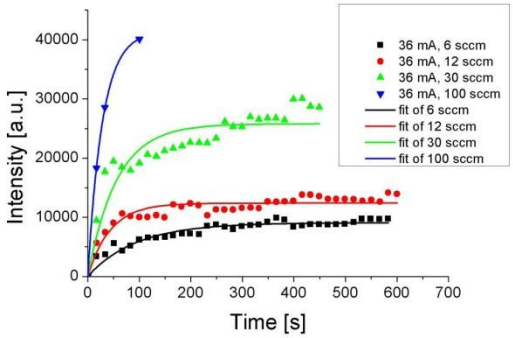

Figure B.6. Time evolution of the area of the D peak. The temperature was 630 °C and the ethylene flow rates were 6, 12, 30 and 100 sccm. The lines are fits using equation 6.3.

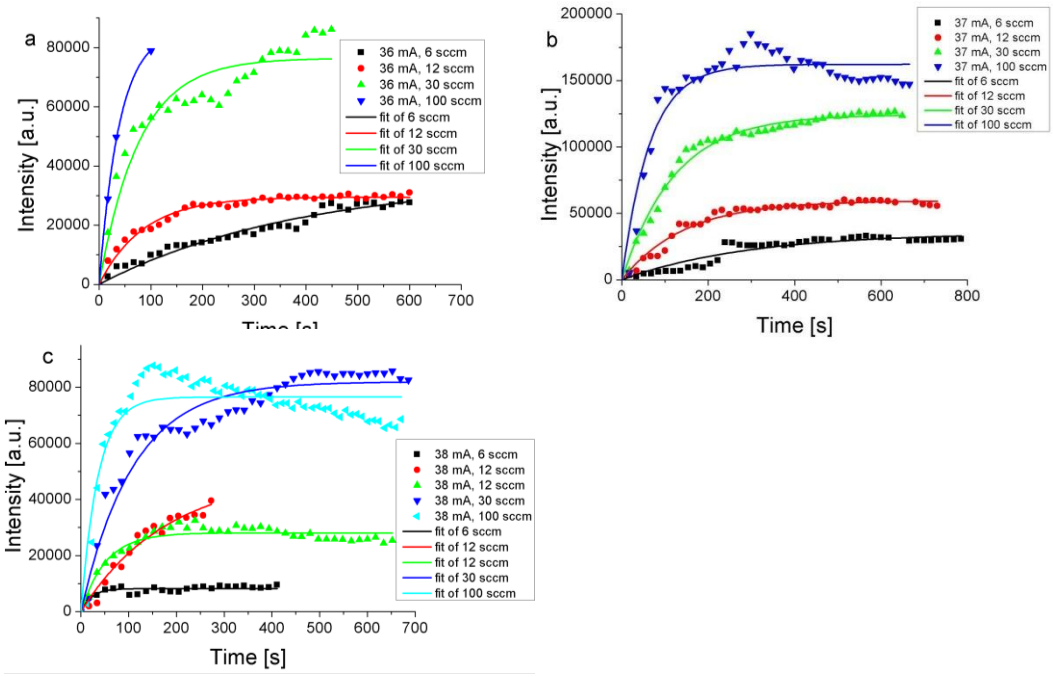

Figure B.7. Time evolution of the area of the G peak. Each image shows the evolution at a constant heater current and temperature for different ethylene flow rates. The temperature is 630 °C in a, 640 °C in b, and 650 °C in c. The lines are fits using equation 6.3.

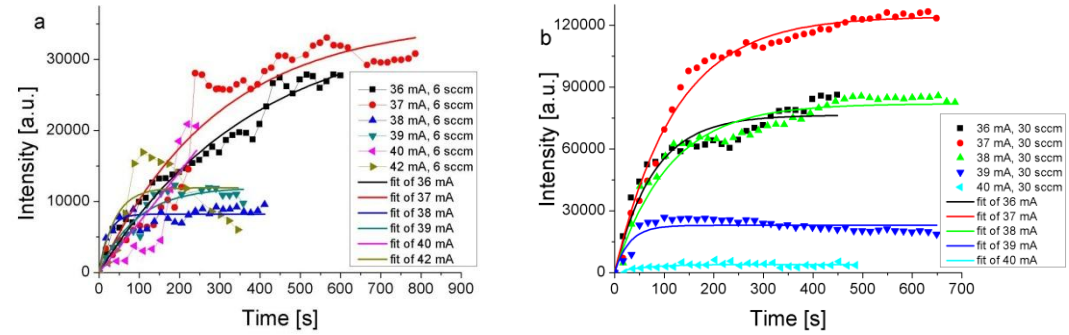

Figure B.8. Time evolution of the area of the G peak. Each image shows the evolution at a constant ethylene flow rate at different heater currents and temperatures. The flow rate is 6 sccm in a, and 30 sccm in b. The lines are fits using equation 6.3.

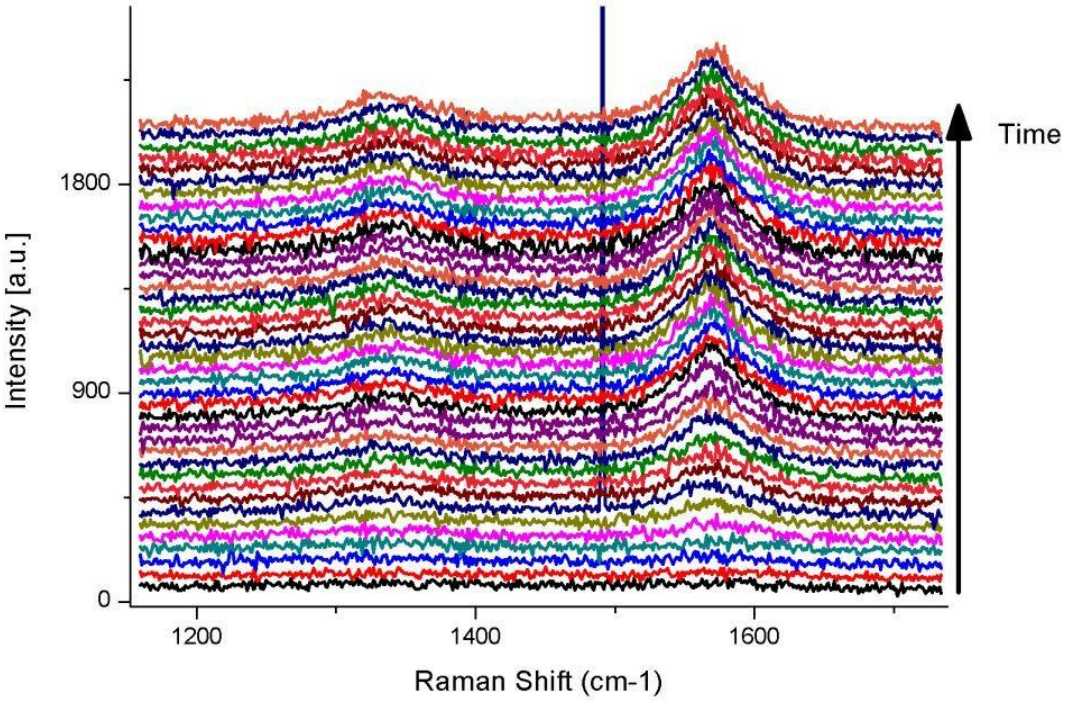

Figure B.9. Time evolution of the Raman spectrum in the D-G region for nanotubes grown at 630 °C using an ethylene flow rate of 12 sccm. Growth proceeds from the bottom to the top and each spectrum is recorded using an acquisition time of 15 s. A larger D peak is visible here than in the time series shown in 6.2.2. The sharp peak is from a cosmic ray.

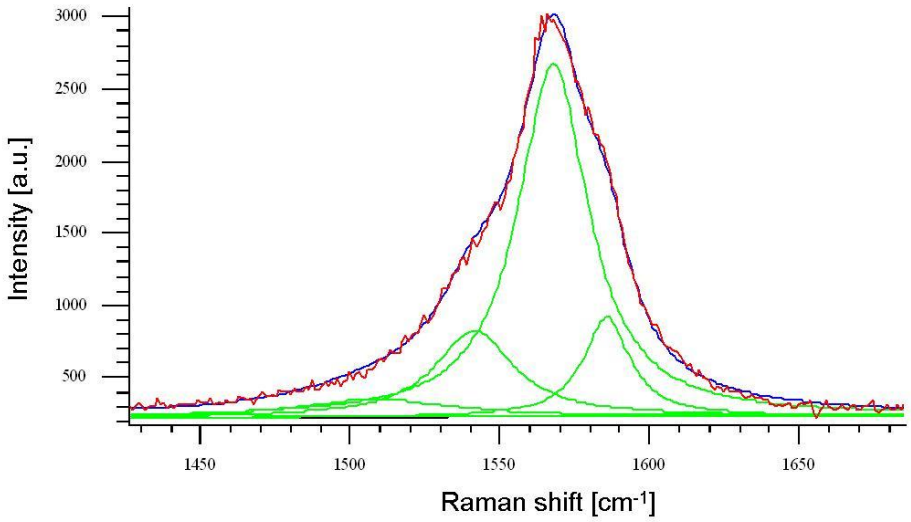

Figure B.10. Fit of the G band for growth of nanotubes using an ethylene flow of 100 sccm at 640 °C. The spectrum was acquired after 5 min with an acquisition time of 15 s.

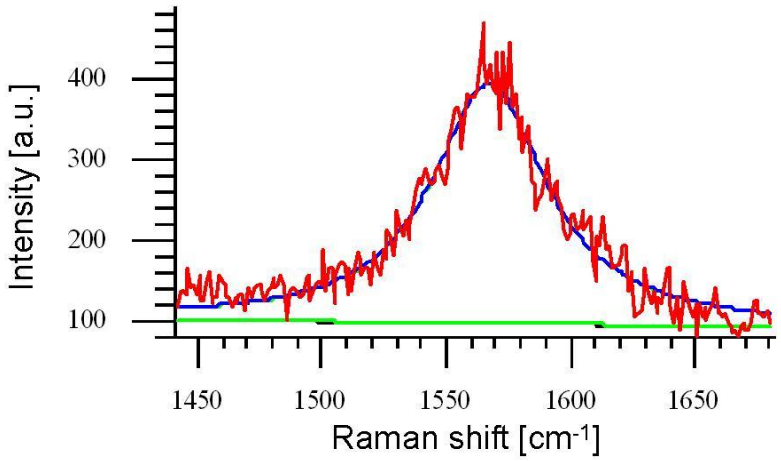

Figure B.11. Fit of the G band for growth of nanotubes using an ethylene flow of 12 sccm at 630 °C. The spectrum was acquired after 5 min with an acquisition time of 15 s.

Appendix C Laser heating

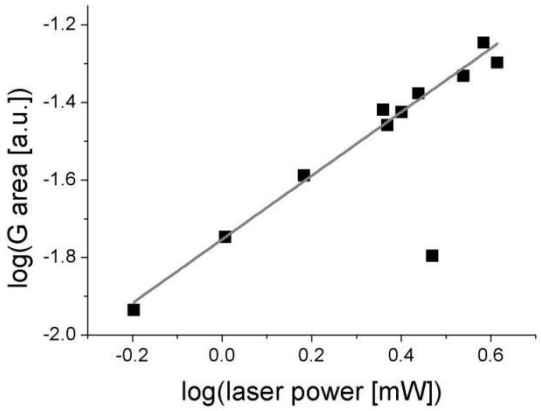

Figure C.1. Logarithm of the area of the G peak plotted against the logarithm of the laser power. The slope is a linear fit which gives a gradient of 0.82.

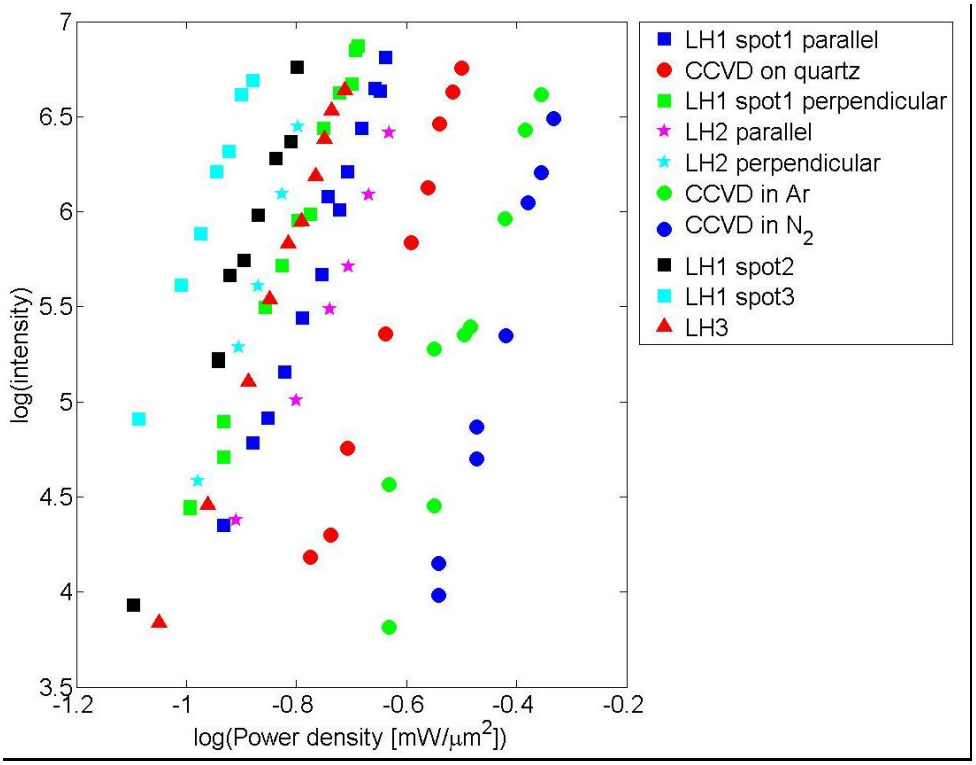

Figure C.2. Logarithm of the irradiated intensity plotted versus the logarithm of the laser power density.

Table C.1. Table showing the estimated positions of the G and D peaks without any heating.

Sample	Estimated G position at 0 mW laser power	Estimated D position at 0 mW laser power
LH1 spot1 parallel	1587.0	1304.7
CCVD on quartz	1580.9	1315.6
LH1 spot1 perpendicular	1594.2	1301.5
	1595.1	1304.4
LH2 parallel	-	1308.3
LH2 perpendicular	-	1309.5
CCVD in Ar	1580.1	1311.8
	1579.1	1312.4
CCVD in N_2	1580.4	1318.1
	1579.9	1316.9
LH1 spot2	1594.5	1305.6
		1305.4
LH1 spot3	1600.9	1313.0
	1601.3	1310.7
LH3	1594.6	1308.7
Average ± standard deviation: Conventional CVD	1580.1 ± 0.7	1314.0 ± 2.8
Local heating	1595.4 ± 4.8	1307.2 ± 3.4

Appendix D LabVIEW program

Main.vi

LabVIEW program used to control the current through the heater and monitor the voltage across the heater and across the full device.

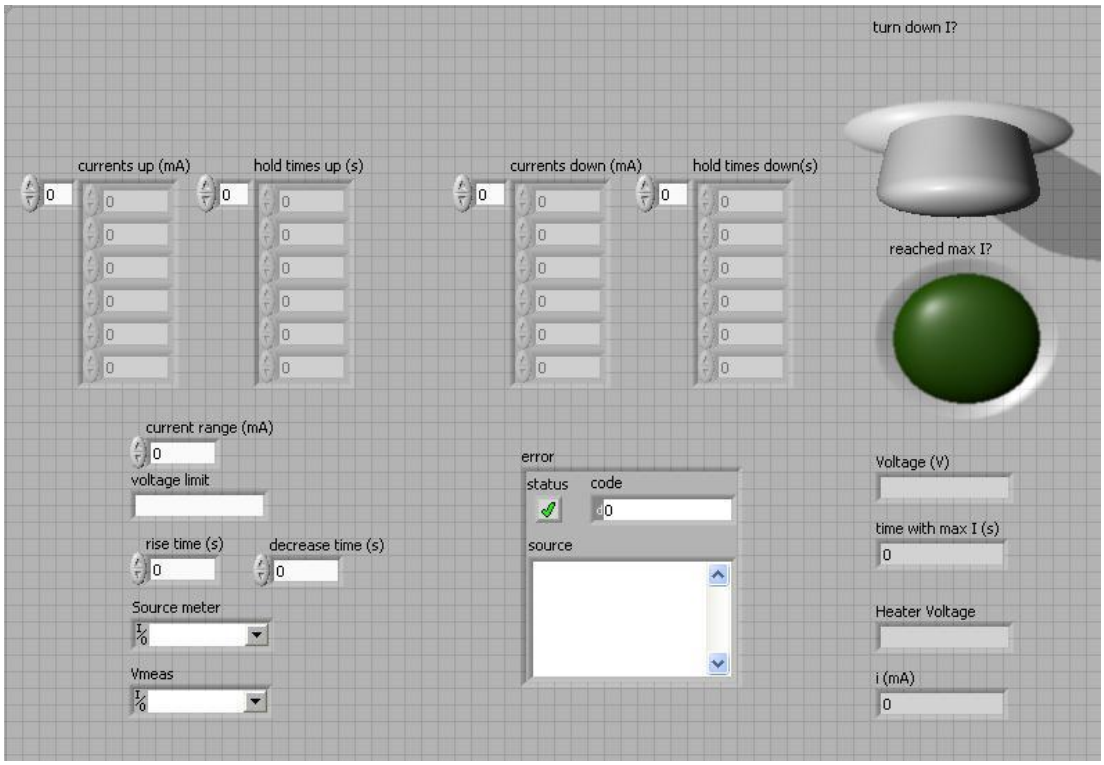

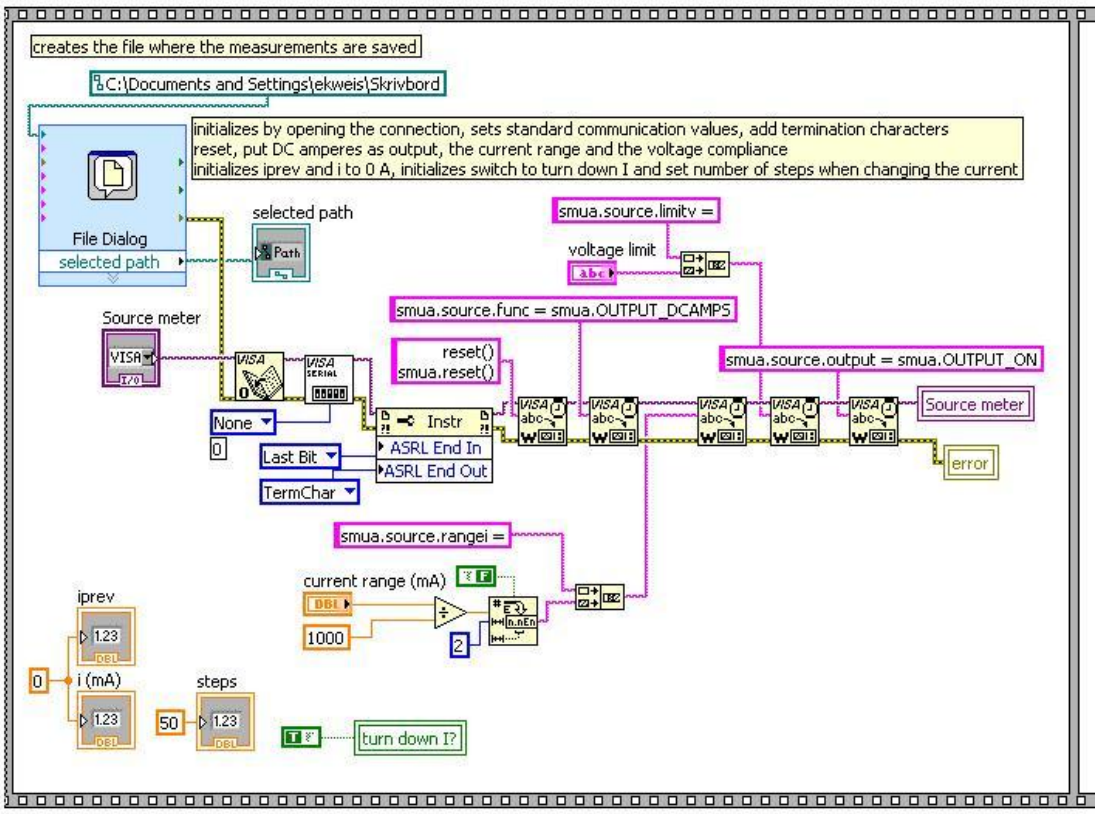
creates the file where the measurements are saved
C:\Documents and Settings\ekweis\Skrivbord
initializes by opening the connection, sets standard communication values, add termination characters
reset, put DC amperes as output, the current range and the voltage compliance
initializes iprev and i to 0 A, initializes switch to turn down I and set number of steps when changing the current
File Dialog
selected path
selected path
smua.source.limitv =
voltage limit
Source meter
smua.source.func = smua.OUTPUT_DCAMPS
reset()
smua.reset()
smua.source.output = smua.OUTPUT_ON
Source meter
error
None
0
Last Bit
TermChar
Instr
ASRL End In
ASRL End Out
smua.source.rangei =
current range (mA)
1000
2
iprev
0
i (mA)
steps
50
turn down I?

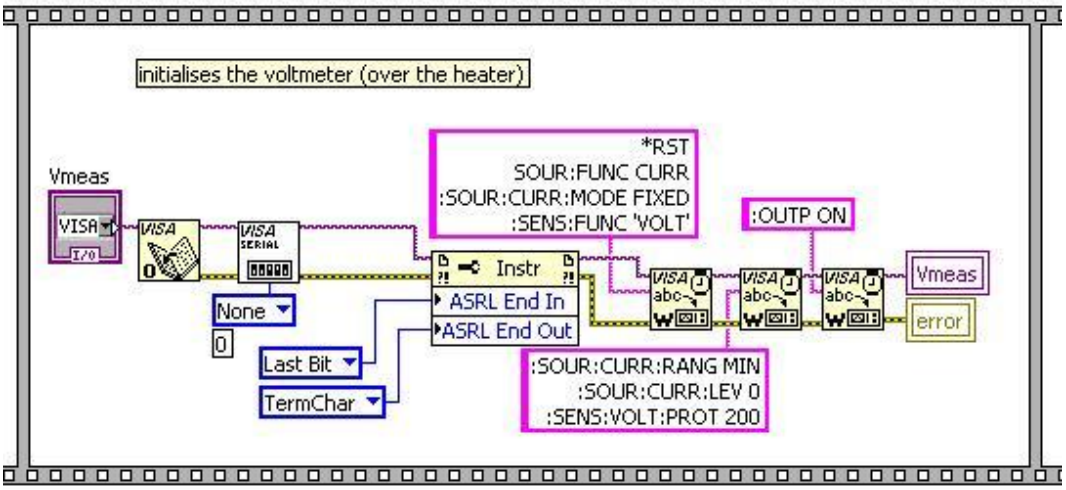
initialises the voltmeter (over the heater)
Vmeas
*RST
SOUR:FUNC CURR
:SOUR:CURR:MODE FIXED
:SENS:FUNC 'VOLT'
:OUTP ON
Instr
ASRL End In
ASRL End Out
None
0
Last Bit
TermChar
Vmeas
error
:SOUR:CURR:RANG MIN
:SOUR:CURR:LEV 0
:SENS:VOLT:PROT 200

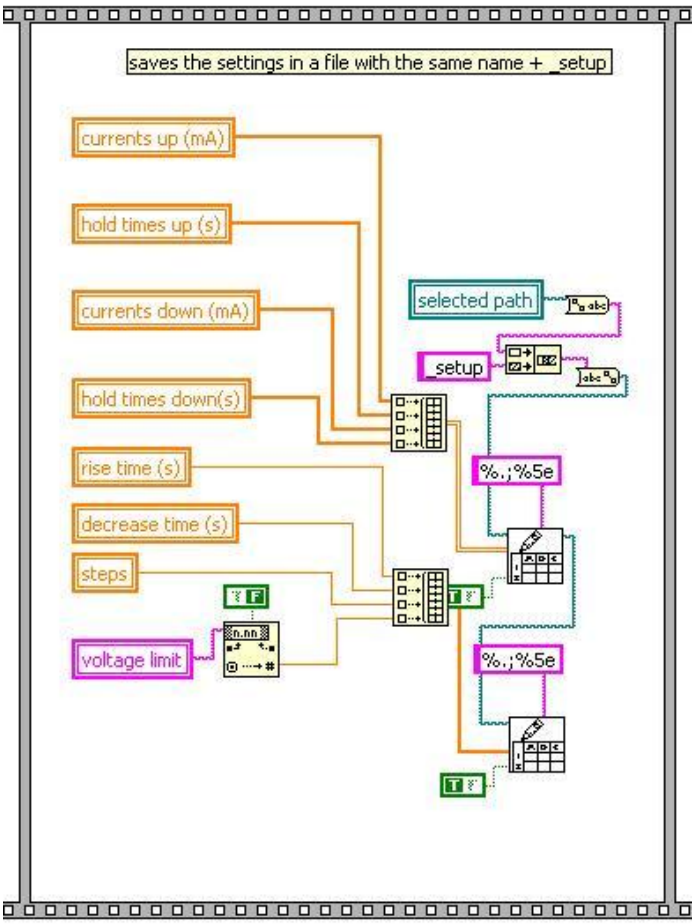
saves the settings in a file with the same name + _setup
currents up (mA)
hold times up (s)
currents down (mA)
hold times down(s)
rise time (s)
decrease time (s)
steps
voltage limit
selected path
_setup
%.;%5e
%.;%5e

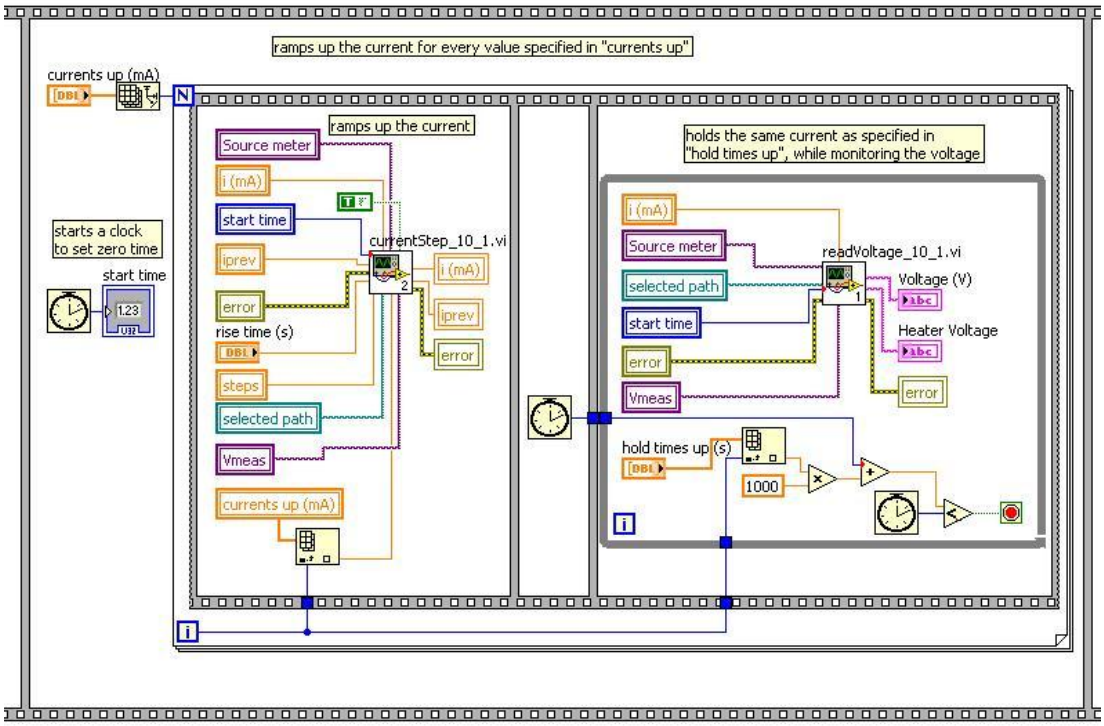
ramps up the current for every value specified in "currents up"
currents up (mA)
starts a clock to set zero time
start time
ramps up the current
Source meter
i (mA)
start time
iprev
error
rise time (s)
steps
selected path
Vmeas
currents up (mA)
currentStep_10_1.vi
holds the same current as specified in "hold times up", while monitoring the voltage
readVoltage_10_1.vi
Voltage (V)
Heater Voltage
hold times up (s)
1000

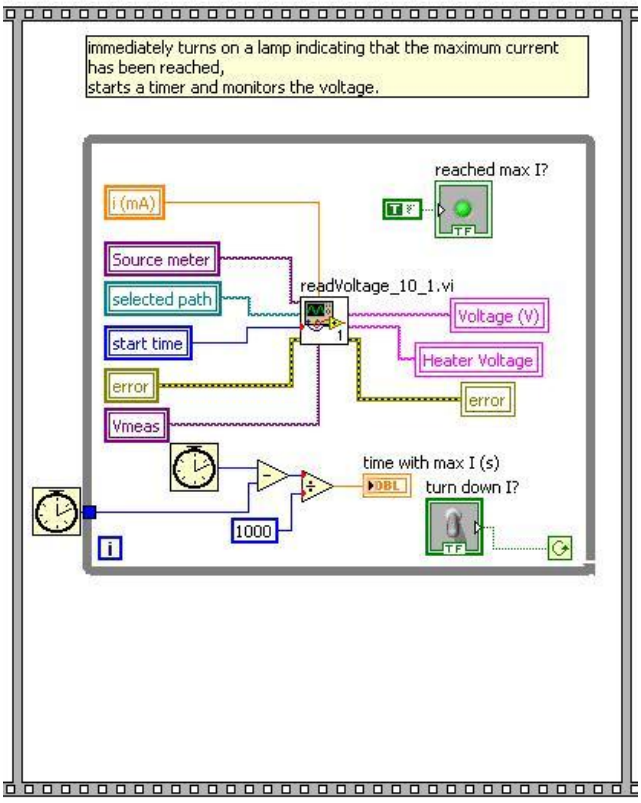
immediately turns on a lamp indicating that the maximum current has been reached,
starts a timer and monitors the voltage.
reached max I?
i (mA)
Source meter
selected path
start time
error
Vmeas
readVoltage_10_1.vi
Voltage (V)
Heater Voltage
error
time with max I (s)
turn down I?
1000

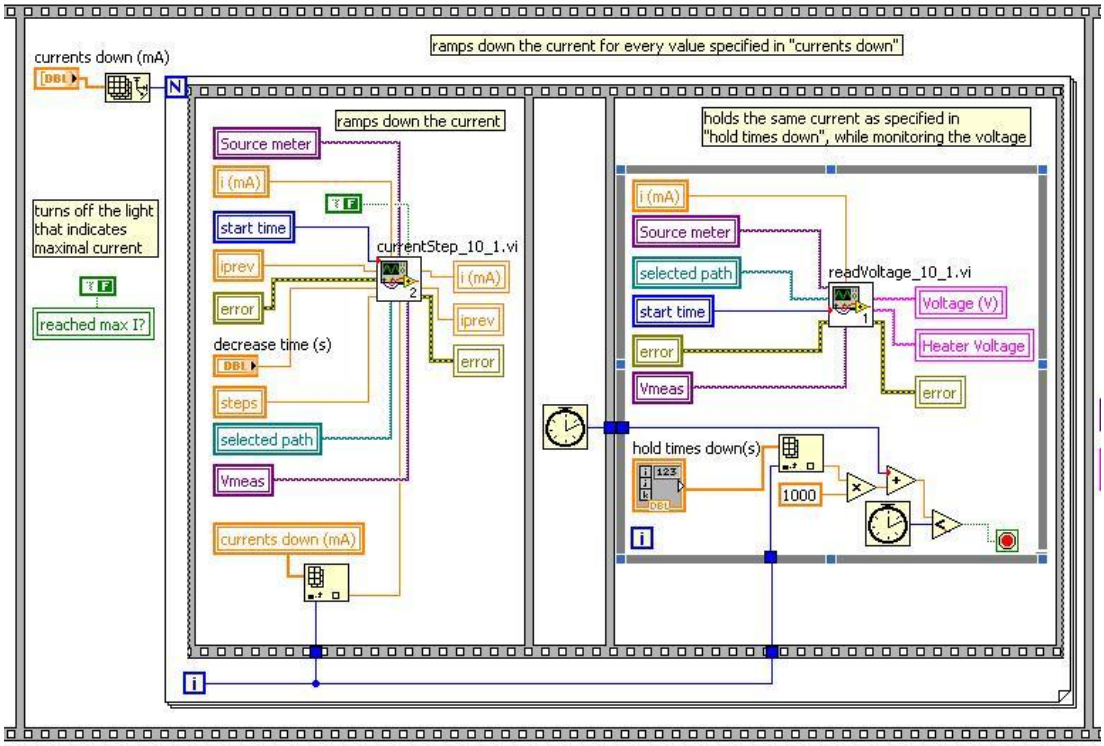
currents down (mA)
ramps down the current for every value specified in "currents down"
turns off the light that indicates maximal current
reached max I?
ramps down the current
Source meter
i (mA)
start time
iprev
error
currentStep_10_1.vi
decrease time (s)
steps
selected path
Vmeas
currents down (mA)
holds the same current as specified in "hold times down", while monitoring the voltage
readVoltage_10_1.vi
Voltage (V)
Heater Voltage
hold times down(s)
1000

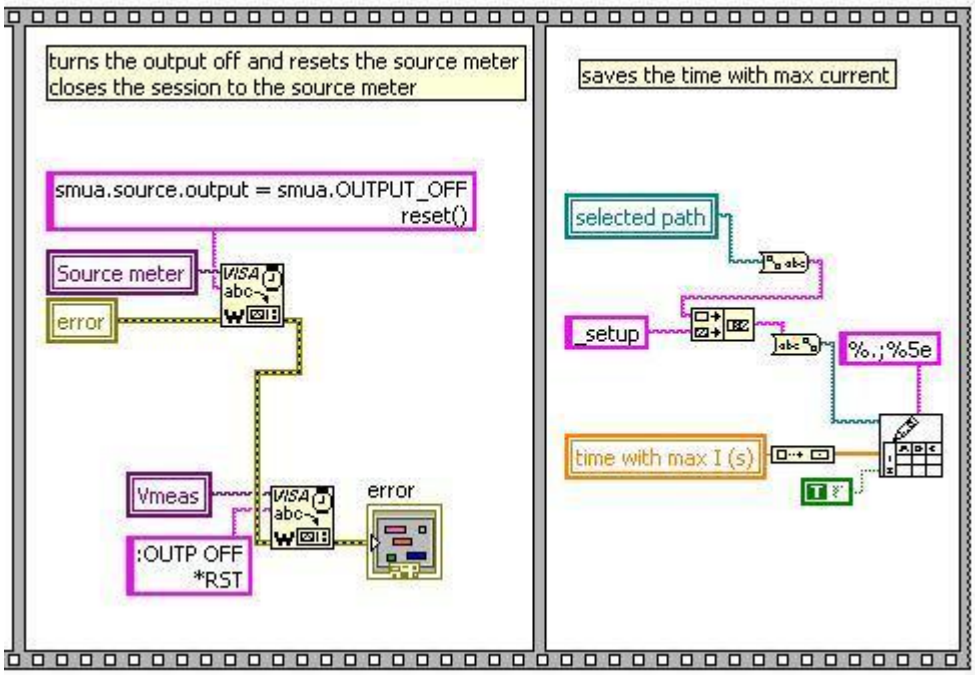
turns the output off and resets the source meter
closes the session to the source meter
smua.source.output = smua.OUTPUT_OFF
reset()
Source meter
error
VISA
abc
Vmeas
:OUTP OFF
*RST
error
saves the time with max current
selected path
_setup
%.;%5e
time with max I (s)

currentStep.vi

Subprogram of Main.vi, used to increase the current through the heater while monitoring the voltage drop.

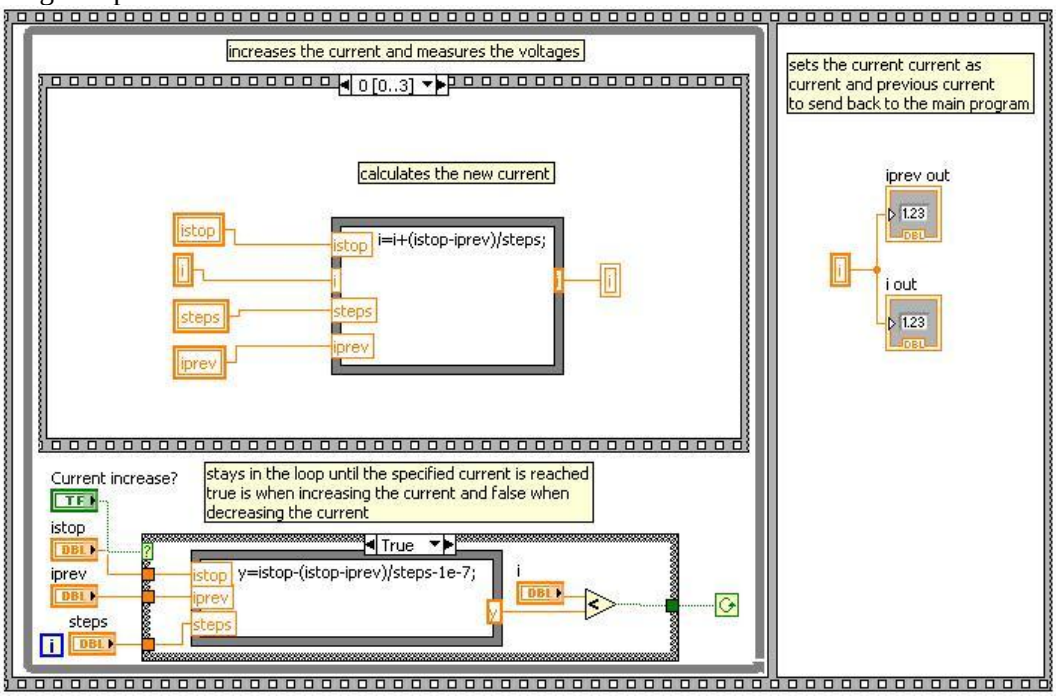

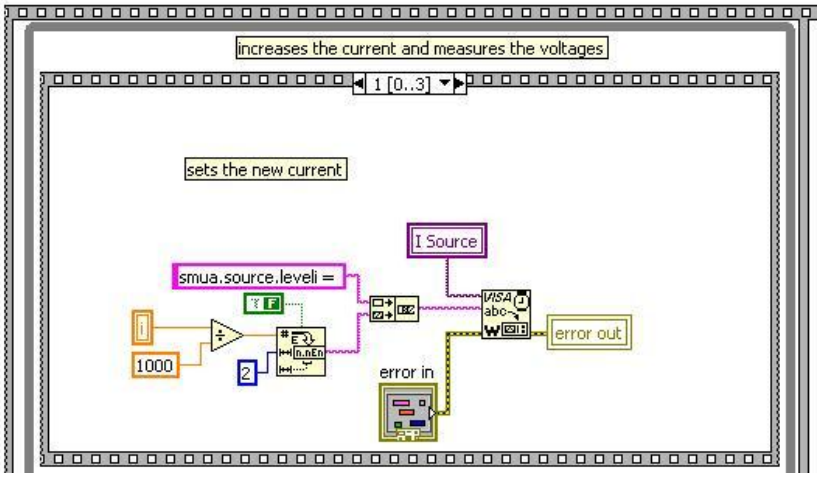

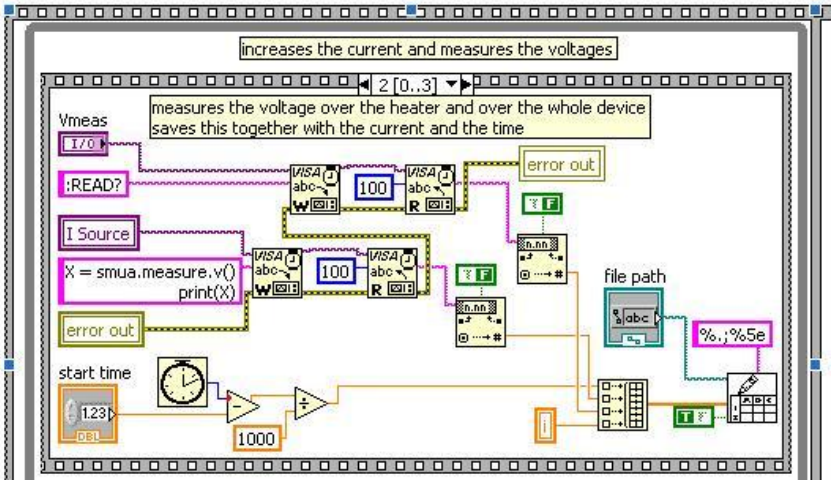
increases the current and measures the voltages
2 [0..3]
measures the voltage over the heater and over the whole device
saves this together with the current and the time
Vmeas
I/O
:READ?
I Source
X = smua.measure.v()
print(X)
error out
100
100
error out
file path
%.;%5e
start time
1.23
DBL
1000

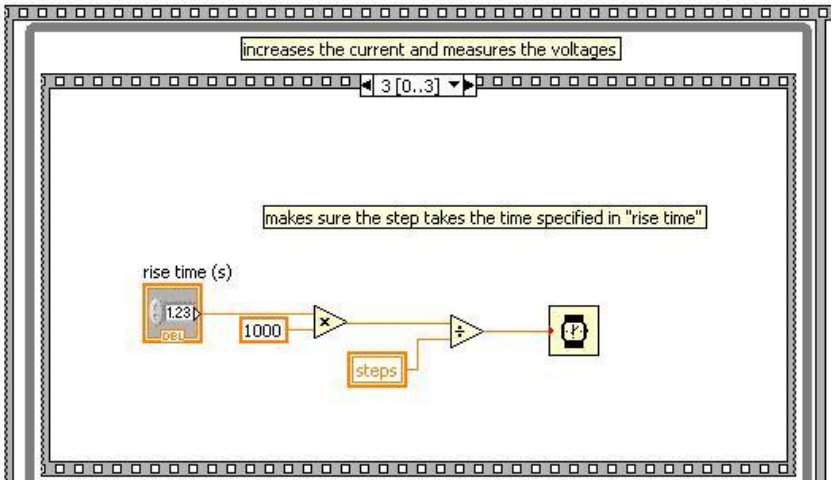
increases the current and measures the voltages
3 [0..3]
makes sure the step takes the time specified in "rise time"
rise time (s)
1.23
DBL
1000
steps

readVoltage.vi

Subprogram of Main.vi, used to measure the voltage across the heater and across the whole device.

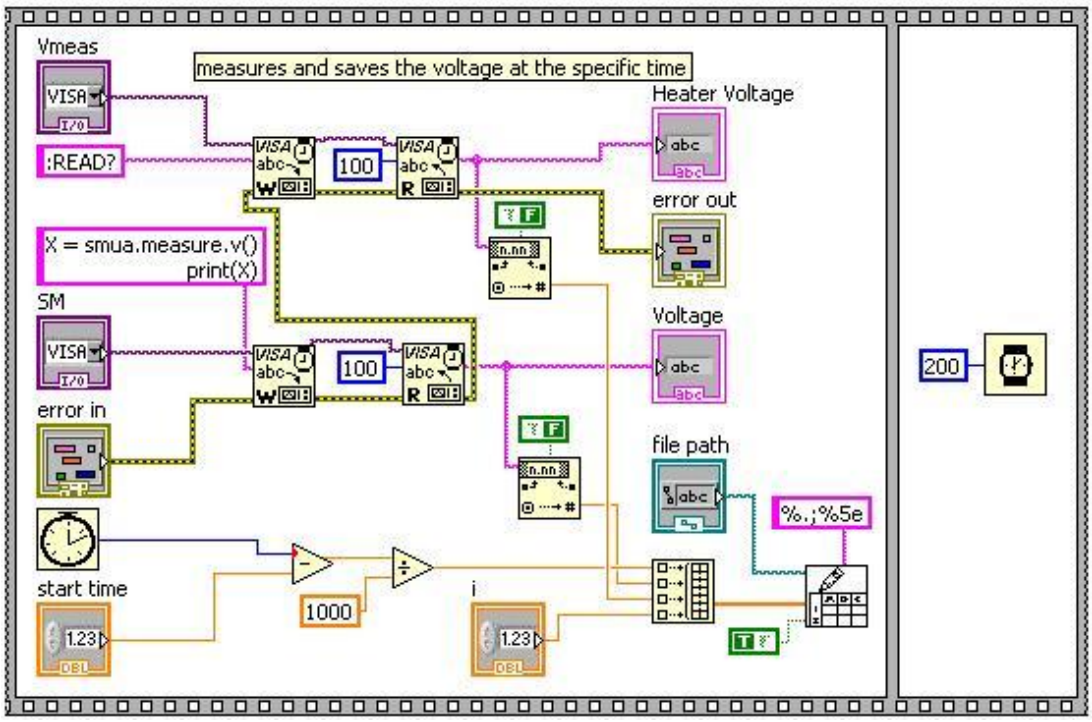

Appendix E Matlab code for temperature estimations

```
close all
clear all
clc

%%%%%%%%%%%%%%%%%%%%% specify the input file
folder = 'D:\Raman\20110221\';
file = 'E86_a_T_.txt';

%%%%%%%%%%%%%%%%%%%% create a vector with 1000 points in the
interval
x_start=600e-9; % start at this wavelength
x_stop=950e-9;  % stop at this wavelength
X1000=linspace(x_start,x_stop,1000); % creates a vector with 1000
points between these values

order = 10; % order of the fitted polynom

%%%%%%%%%%%%%%%%%%%% What the lamp really looks like (the original)
lampreal = load ('D:\Raman\Lampreal.txt'); % loads what the lamp
really looks like
lampreal(:,1)=lampreal(:,1).*1e-9;
lampreal_polykoeff = polyfit(lampreal(:,1),lampreal(:,2),order); %
calculates polynomial fit of the real lamp
fitlampreal_polynom_1000=polyval(lampreal_polykoeff,X1000); %
creates this curve in 1000 points

figure (1)
plot(lampreal(:,1),lampreal(:,2)); % plots the lamp
hold on
plot(X1000,fitlampreal_polynom_1000,'r'); % plots the fit
title('Lamp original')
legend('original','fitted')
xlabel('Wavelength (nm)')
ylabel('intensity (a.u.)')

%%%%%%%%%%%%%%%%%%%% what the lamp looks like in the spectrometer
%%% different files depending on setup
%lampmeas = load ('D:\Raman\20091014T\Cal_Lamp66A_step.txt'); %
loads the measured lamp
lampmeas = load ('D:\Raman\James\20091027\Lamp_Hole1.txt'); % loads
the measured lamp
% lampmeas = load
('D:\Raman\20100811\Wlamp_785nmlensesANDedge.txt'); % load the
measured lamp, 785nm lenses+edge
% lampmeas(:,1) = 1e7./((1e7./785)-lampmeas(:,1)); % changed for
raman shift (cm-1) and not lambda, for 785 nm
% lampmeas_long = load ('D:\Raman\James\20100119\Lamp-Diaphragm-6A6-
Notch1.txt'); % for notch filter
% lampmeas = load
('D:\Raman\Duncan\20100722\Wlamp_Tmeas_514nmlenses_step_10umslit_1.t
xt'); % load the measured lamp, 785 setup, 514nm lenses no filter
 lampmeas(:,1)=lampmeas(:,1).*1e-9;

%%% create polynomial
```

```
lampmeas_polykoeff = polyfit(lampmeas(:,1),lampmeas(:,2),order); %
calculates polynomial fit of the measured lamp
fitlampmeas_polynom_1000=polyval(lampmeas_polykoeff,X1000); %
creates this curve in 1000 points

figure (2)
plot(lampmeas(:,1),lampmeas(:,2)); %plots the measured lamp
hold on
plot(X1000,fitlampmeas_polynom_1000,'r'); % and the fit
title('Measured lamp')
legend('Measured','Fitted')
xlabel('Wavelength (nm)')
ylabel('Intensity (a.u.)')

figure(10)
plot(lampreal(:,1).*1e9,lampreal(:,2)./max(lampreal(:,2)),'k--
','LineWidth',3); % plots the lamp
s1 = xlabel('Wavelength [nm]'); set(s1,'FontSize',20);
s2 = ylabel('Normalised intensity [a.u.]'); set(s2,'FontSize',20);
set(gca,'FontSize',15);
hold on
plot(lampmeas(:,1).*1e9,lampmeas(:,2)./max(lampmeas(:,2)),'k','LineW
idth',3); %plots the measured lamp
axis([200 1100 0 1.05])
legend('Real W lamp spectrum','Measured W lamp
spectrum','Location','NorthWest')

%%%%%%%%%%%%%%%%%%%% calculates the transfer function,
%%% measured curve .* transfer function = real light
transferfct = fitlampreal_polynom_1000./fitlampmeas_polynom_1000; %
Calculates the transfer function

figure (3)
plot(X1000,transferfct./max(transferfct));
% plots the (normalised) transfer function
title('Transfer function (normalised)');
xlabel('Wavelength (nm)')
ylabel('intensity (a.u.)')

% test it on the measured lamp
figure (4)
plot(X1000,fitlampmeas_polynom_1000.*transferfct);
hold on
plot(X1000,fitlampreal_polynom_1000,'r--');
legend('measured','real')
xlabel('Wavelength (nm)')
ylabel('intensity (a.u.)')

%%%%%%%%%%%%%%%%%%%% heater spectrum
spectra = load(strcat(folder,file)); % loads the file specified
above
spectra_x = spectra(:,1).*1e-9; % x-values
%spectra_x(:,1) =1e7./((1e7./785)-spectra(:,1)); % changed for raman
shift (cm-1) and not lambda, for 785 nm
spectra_y = spectra(:,2); % y-values
interval_indices = find(spectra_x>=x_start & spectra_x<=x_stop); %
takes out the specified part of the spectra
```

```
spectra_interval_x = spectra_x(interval_indices); % Uses this on the
x-values
spectra_interval_y = spectra_y(interval_indices); % Uses this on the
y-values
figure (5)
plot(spectra_interval_x,spectra_interval_y)
xlabel('Wavelength (nm)')
ylabel('intensity (a.u.)')
figure(9)

plot(spectra_interval_x.*1e9,spectra_interval_y./max(spectra_interva
l_y),'k:')
hold on
s1 = xlabel('Wavelength [nm]'); set(s1,'FontSize',20);
s2 = ylabel('Normalised intensity [a.u.]'); set(s2,'FontSize',20);
set(gca,'FontSize',15);

%%%%%%%%%%%%%%%%%%%% transfer function for the specified interval
% create polynomial for the real lamp
fitlampreal_polynom_interval =
polyval(lampreal_polykoeff,spectra_interval_x);
% create polynomial for the measured lamp
fitlampmeas_polynom_interval =
polyval(lampmeas_polykoeff,spectra_interval_x);
% calculate transfer function in the interval
transferfct_interval =
fitlampreal_polynom_interval./fitlampmeas_polynom_interval;
figure(3)
hold on
plot(spectra_interval_x,transferfct_interval./max(transferfct_interv
al),'r--')

%%%%%%%%%%%%%%%%%%%% calculates the real curve
spectra_real = spectra_interval_y.*transferfct_interval;
spectra_real_normalised = spectra_real./max(spectra_real); %
normalise
figure (6)
plot(spectra_interval_x,spectra_real_normalised)
figure (9)
plot(spectra_interval_x.*1e9,spectra_real_normalised,'k')
legend('measured blackbody spectrum','corrected blackbody
spectrum','Location','NorthWest')

%%%%%%%%%%%%%%%%%%%% polynomial fit of the spectrum
spectra_real_normalised_polykoeff =
polyfit(spectra_interval_x,spectra_real_normalised,order); %
calculates the polynomial
spectra_real_normalised_polynom_interval =
polyval(spectra_real_normalised_polykoeff,spectra_interval_x);
figure (6)
xlabel('Wavelength [nm]')
ylabel('Intensity [a.u.]')
hold on
plot(spectra_interval_x,spectra_real_normalised_polynom_interval,'r'
)
%create output file
%dlmwrite(strcat(library,'polyfit',file),[spectra_interval_x,
spectra_real_normalised_polynom_interval],'\t');
```

```
%%%%%%%%%%%%%%%%%%%% more points
spectra_real_normalised_polynom_1000 =
polyval(spectra_real_normalised_polykoeff,X1000);
plot(X1000,spectra_real_normalised_polynom_1000,'g--')

%%%%%%%%%%%%%%%%%% constants
h=6.62606896*10^(-34);
c=299792458;
k=1.3806504*10^(-23);
lambda= linspace(x_start,x_stop,1000);

% Wien's approximation
figure(7)
plot(1./(spectra_interval_x), -
k/h/c*log(1*spectra_real.*(spectra_interval_x).^5))
hold on

%%% removes Raman peaks (if they are large)
%     x_start_wien = 620e-9; % start just after G
%     Gprim_low = 740e-9; % removing G'
%     Gprim_high = 810e-9;% removing G'
%     x_stop_wien = 860e-9; % stop when transfer func fitting is
worse
%     interval_indices_wien = find((spectra_x>=x_start_wien &
spectra_x<=Gprim_low) | (spectra_x>=Gprim_high &
spectra_x<=x_stop_wien)); % takes out the specified part of the
spectra
    x_start_wien = 690e-9; % start just after G
    x_stop_wien = 830e-9;  % stop when the sensitivity and fittings
are worse
    interval_indices_wien = find(spectra_x>=x_start_wien &
spectra_x<=x_stop_wien); % takes out the specified part of the
spectra

spectra_interval_x_wien = spectra_x(interval_indices_wien); % Uses
this on the x-values
spectra_interval_y_wien = spectra_y(interval_indices_wien); % Uses
this on the y-values

fitlampreal_polynom_interval_wien =
polyval(lampreal_polykoeff,spectra_interval_x_wien); % create
polynomial for the real lamp
fitlampmeas_polynom_interval_wien =
polyval(lampmeas_polykoeff,spectra_interval_x_wien); % create
polynomial for the measured lamp
transferfct_interval_wien =
fitlampreal_polynom_interval_wien./fitlampmeas_polynom_interval_wien
; % calculate transfer function in the interval

spectra_real_wien =
spectra_interval_y_wien.*transferfct_interval_wien;

plot(1./(spectra_interval_x_wien), -
k/h/c*log(1*spectra_real_wien.*(spectra_interval_x_wien).^5),'g')
        s1 = xlabel('1/Wavelength [nm^{-1}]');
set(s1,'FontSize',20);
```

```
        s2 = ylabel('-ln(I \lambda^{5}) [a.u.]');
set(s2,'FontSize',20);
        set(gca,'FontSize',15);

figure(8)
plot(1./(spectra_interval_x_wien), -
k/h/c*log(1*spectra_real_wien.*(spectra_interval_x_wien).^5),'g')

camorbit(180,0) % rotates the image
```